DEPARTMENT OF GEOLOGY AND GEOPHYSICS
ADDIS ABABA UNIVERSITY
SCHOOL OF GRADUATE STUDIES

Application of Remote Sensing in Lithological Mapping and Reconstruction of the Stratigraphy of North - western Mekele Area, Ethiopia.

By

BERHANU TEMESGEN

Addis Ababa
May 1995

Application of Remote Sensing in Lithological Mapping and Reconstruction of the Stratigraphy of North - western Mekele Area, Ethiopia.

A Thesis presented to
The School of Graduate Studies of
Addis Ababa University.

In Partial Fulfilment of
the Requirements for the Degree
Master of Science in Geology

by
Berhanu Temesgen
May 1995.

ADDIS ABABA UNIVERSITY

SCHOOL OF GRADUATE STUDIES

APPLICATION OF REMOTE SENSING IN LITHOLOGICAL MAPPING AND RECONSTRUCTION OF THE STRATIGRAPHY OF NORTH-WESTERN MAKELE AREA, ETHIOPIA.

by

BERHANU TEMESGEN

FACULTY OF SCIENCE

DEPARTMENT OF GEOLOGY AND GEOPHYSICS.

APPROVAL BY BOARD OF EXAMINERS

Dr. Tilahun Mammo
Chairman, Department
Graduate Committee

Prof. Antonio Russo
Advisor

Prof. Roberto Valera
Examiner (External)

Dr. Gezahegn Yirgu
Examiner

Dr. Endale Ketefo
Examiner

Abstract

The area under study is located within the Mekele out lier. It comprises Mesozoic sedimentary rocks unconformably overlain by trap volcanics.

Landsat-TM images have been processed and geologically analysed in combination with revision of the previous works and present field survey for lithological mapping and reconstruction of the stratigraphy of the study area.

In remote sensing the sensor and the object to be sensed are located remotely apart. The link is due to electromagnatic (EM) waves. Thus in image processing and interpretation the knowledge of how EM radiation is generated, propagated, and modified when it interacts with materials is the main key.

Materials produce a diagnostic spectral signature in response to the EM interaction. Generally, spectral signatures are related to the nature of the corresponding rock, which help to identify a material through image processing. Image processing includes statistical and graphical evaluation, ratioing, contrast enhancement, principal and canonical component analyses, combination of selected bands, texture and vegetation index analyses, classification, and visual interpretation of the images.

Structures and other lineaments, lithological boundaries, and drainage patterns are traced directly from the screen during image interpretation. Ten mappable units are recognized both by digital image processing and visual interpretation. These are from youngest to oldest: Dolorite, Basalt, Amba Aradam Formation, Agula Shale, five separately mappable Antalo Limestone units, and Adigrat Sandstone.

From sedimentary point of view, Adigrat Sandstone is fluviatile in origin, while the Antalo Limestone and Agula Shale are related with transgression and regression of the sea during Jurassic time. Amba Aradam Formation, on the contrary, lying unconformably on Agula Shale, is probably due to the withdral of the sea caused by an uplift of cratonic area related to the separation of America and Africa plates during the Cretaceous time.

The final thematic images are geometrically rectified using selected ground control points to refer them with other maps. Digitally processed images expose fairly well the main lithologic units with some limitation.

Contents

Page

List of Tables

Annexes

Acknowledgement

This is an opportunity to convey my gratitude to the many persons who contributed to my education and career, in particular to my advisors Prof. Antonio Russo and Prof. Alberto Marini.

An equally generous thanks should also be extended to the Germany Academic Exchange Service (DAAD), that awarded me an in-country scholarship for two years in my post graduate study and for the financial support for the research project. I wish also to express my wholehearted appreciation to the Italian Technical Unit (UTL) for the financial support during the field work.

Finally, I would like also to thank all my colleagues and friends, whose support is indispensable, specially Ato Lulseged Ayalew, Ato Worash Getaneh, Ato Asfawossen Asrat for their assistance in data collection during the field and in organizing the thesis. I am indebted to Ato Belachew and Ato Getenet Beshah (from EMA) for the help they rendered me during image processing.

1. INTRODUCTION

This Thesis presents the results of application of remote sensing methods to lithological mapping and reconstruction of the stratigraphy of an area located north - west of Mekele, in northern Ethiopia. The area under consideration covers about 800 sq. km, and is located 800 km north of Addis Ababa. It lies within the Northern Ethiopia Sedimentary basin between 13^0 00'' N and 14^0 30'' N latitudes, and 38^0 30'' E and 40^0 00'' E longitudes (see Fig 1.1.); specifically it is to the west of the main road from May Mekden to Wukro including the area up to Hagere Selam.

The area comprises gentle rolling relief, cut by steep gorges along rivers, and bounded on all sides by steep cliffs at the main rivers. Elevation, within the area, ranges from 1770 to 2809 m a.s.l.

There are two main roads in the study area that run from Mekele to Wukro and from Mekele to Hagere Selam. Both are all weathered roads.

The climate in the region is characterized by moderate and pleasant temperature with 500 to 600 mm mean annual rainfall, and in general has semi-arid environment. The annual precipitation is usually between July and September, with a dry period of seven to eight months.

The natural vegetation commonly found in the region consists of seasonal grasses and scattered trees. Crops, which are grown only in the rainy seasons, cover most of the field for two to four months.

The geology of the area has attracted many workers starting from the beginning of 1940's. Main studies in the Mekele basin include those of Merla and Minucci, (1938); Dainelli, (1943); Engels, (1966, 1970); Shumburo, (1968); Abbate et al, (1968); Levitte, (1969,1970); Beyth, (1970, 1972); and Akin et al, (1971). Their works emphasied on description of rocks, construction of the stratigraphy, and lithological and structural mapping on 1: 250, 000 scale

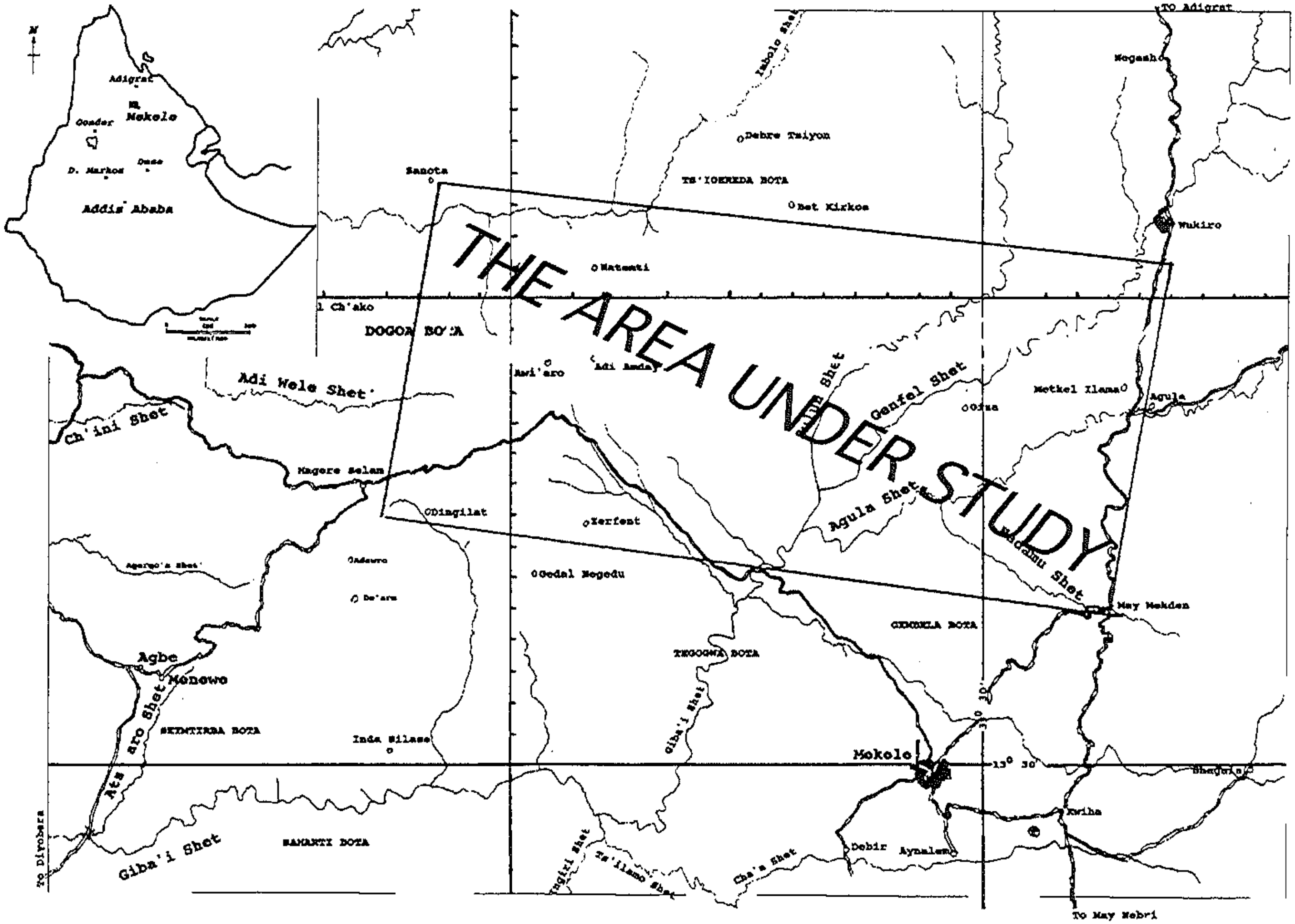

Fig.1.1 Location Map Of the Study Area.

from field survey, laboratory analysis of rock samples and interpretation of small scale aerial photographs.

A detailed geological map of an area is a very important base for a proper study of multi-disciplinary works. Mapping by remote sensing is cost - effective and time efficient. Lithological contacts can be delineated over large area with a minimum ground control, and identification of rock types can be extrapolated on the basis of spectral and geomorphic information. In addition to these, image interpretation provides analysis of small scale features in relation to a more regional context. In the area where this study has been conducted there were no geological and topographic maps larger than 1: 250,000 scale. Hence, the purpose of this work is to apply remote sensing methods for lithological mapping and reconstruction of the stratigraphy of the area to produce a geological map at 1: 100,000 scale. The main objectives are:

-To gain a better understanding of the relationship between geology as mapped from field survey and geology as interpreted from satellite imagery.

- To test if, and to what extent, remote sensing methods help to reconstruct the stratigraphy.

To accomplish these objectives, two field trips, taking 10 and 15 days each were carriedout. Topographic maps, a geological map at scale 1: 250,000 and aerial photographs of 1:50,000 scale were used. A seven-band Landsat Thematic Mapper (TM) image of the 1987, in digital format was also used for lithologic discrimination, passing through all steps of image processing. In addition, interpretation of multispectral SPOT images in red, green and blue (RGB) channels (in the order of band 321) and MSS bands (432 in RGB order) were done to supplant TM image interpretation. TM images were processed using ERDAS version 7.4 image processing soft ware on Compaq Desk Pro-286 computer available at the Ethiopian Mapping Authority Regional Centre of Remote Sensing as well as using DEMPLE version 2.1-881 image processing soft ware on Macintosh Quadra 950 computer found at the Department of Geology and Geophysics. SPOT and MSS colour composite were produced using Photoshop version 2.5 on Macintosh Quadra 950 computer of the Department.

2. FUNDAMENTAL PRINCIPLES OF REMOTE SENSING.

2.1. SCOPE OF REMOTE SENSING

Remote Sensing is a way of obtaining information about an object and phenomena without touching the object and phenomena itself. It includes acquiring of data through a device which is at a distance from the object and analysis of the data for information extraction about the object.

The term remote sensing implies that the sensor and the sensed are located remotely apart. The distance between the two might be several kilometres, and filled with air or vacuum. The only efficient link between the two are electromagnetic waves.

Understanding how electromagnetic radiation is generated, propagated and modified by the intervening media and the object to be sensed is, therefore, indispensable in remote sensing.

2.2. THE NATURE OF ELECTROMAGNETIC RADIATION

Electromagnetic radiation is produced when an electric charge is accelerated or more generally, whenever the size (amplitude / magnitude) and /or direction of the electric (E) or magnetic (H) field is varied with time at its source.

Electromagnetic energy consists of electric and magnetic fields (Fig.2.1) which are transmitted in packets, or quanta, in some form of wave motion. Even though quanta or photons may be considered crudely as energy particles having zero mass at rest they also display wave behaviour under certain conditions. Hence, Pure energy and pure matter are totally abstract concepts.

Combination of Maxwell's electromagnetic wave theory and modern quantum theory give theoretical explanation for all wave and optical phenomena. Maxwell's theory deals primarily with the propagation and macroscopic optical effects of electromagnetic energy, while quantum theory is concerned with the atomic molecular absorption and emission aspects of radiation.

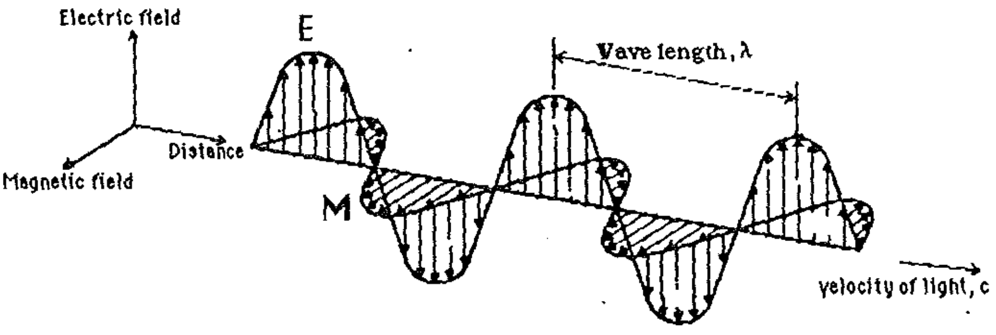

Fig. 2.1. An Electromagnetic wave - the electric and magnetic components are perpendicular to each other and to the direction of motion. λ wavelength; c velocity of light; E electric wave; M magnetic wave (Durary,1987 and Gupta,1991).

Electromagnetic waves have constant velocity in vacuum, but may vary in wavelength and frequency. From basic physics, we have

$$c = \nu\lambda$$

where c is the speed of light, ν is the frequency and λ is the wavelength.

2.3. BLACK BODY RADIATION PRINCIPLE.

A black body is an ideal body which absorbs all radiation incident on it and emits all the radiation it absorbed. It is both good absorber and emitter of radiation. In nature fluctuations in electric and magnetic fields, in one way or the other form are related to the temperature of the body emitting radiation. All matter, at temperatures above absolute zero (-273.1^{o}C), continuously emits EM radiation. Just how much EM energy is emitted and the range of its wavelength is a complex function of both temperature and the nature of the emitting body itself.

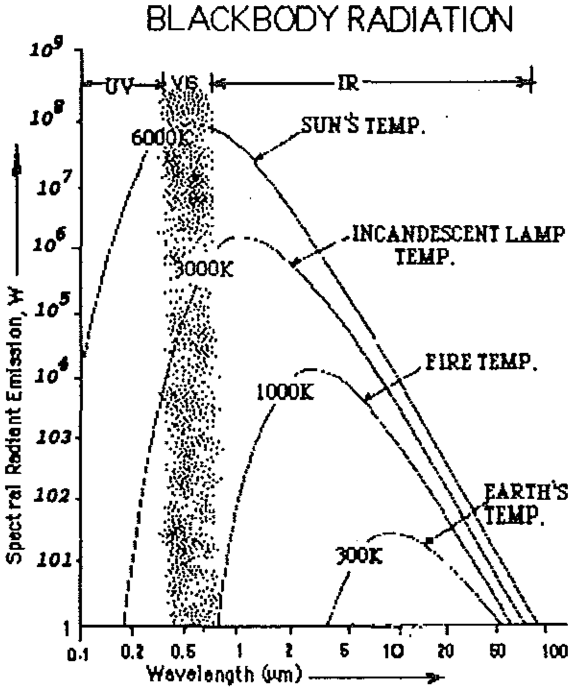

Fig. 2.2. Spectral distribution of energy radiated from blackbodies at various temperatures (Gupta, 1991).

The radiation emitted by a blackbody is proportional to the fourth power of its absolute temperature, i.e.

$$W= sT^4 \quad \text{watts/m}^2$$

where W is the spectral radiance (emittance per unit area), s is the Stefan-Boltzman constant and T is the absolute temperature of the body. The wavelength at which most of the radiation is emitted depends on the temperature of the blackbody. For smaller wavelengths, it is expressed as

$$\lambda_{max.} = A/T$$

where λ_{max} is the wavelength (cm) at which the peak of the radiation occurs; A is a constant (0.29 cm K) and T is the temperature (K) of the object. This is known as Wien's displacement law, and gives the shift in the $\lambda_{max.}$ with temperature of the radiating object (Fig. 2.2). Using this law, one can estimate the temperature of the object by measuring the wavelength of the peak radiation.

2.4. THE ELECTROMAGNETIC SPECTRUM

It may be defined as the ordering of the EM radiation according to wavelength or in other words, according to frequency or energy.

The spectrum has been divided into regions that bear names related to the source that produce them - such as the 'ray' regions; or as extensions from the visible range - such as the ultraviolet and the infrared regions; or according to the way in which the wavelengths in the range are used - such as radio and television (Fig.2.3).

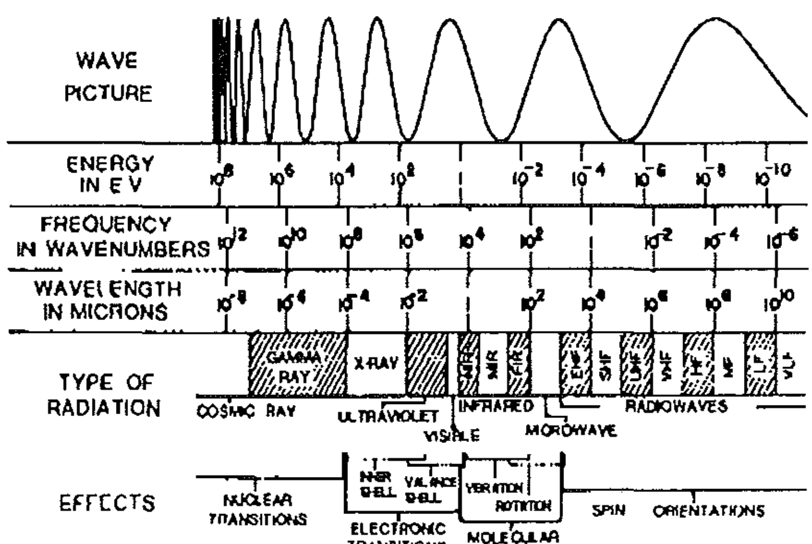

Fig. 2.3. The Electromagnetic spectrum, showing a scheme of the wave, the wavelength ranges, the type of radiation, and the atomic and molecular effects that produce spectral features in the each range (Siegal, 1980).

The EM spectrum, from 0.02 µm to 1m wavelength, can be divided into two main parts (Gupta, 1991): the optical and the microwave range (Table 2.1). The optical range refers to that part of the EM spectrum in which optical phenomena of reflection and refraction can be used to focus the radiation. It extends from x-ray (0.02 µm) through visible up to and including far-infrared (1 mm). The microwave range is from 1 mm to 0.8 m wavelength.

Table 2.1. Major Regions of EM spectrum.

Range	Name	Wavelength range
Optical	X - ray	1 nm - 0.01 µm
	Ultraviolet	0.01 - 0.4 µm
	Visible	0.40 - 0.7 µm
	Near-IR	0.70 - 1.00 µm
	Short wave IR	1.00 - 1.12 µm 1.19 - 1.34 µm 1.55 - 1.75 µm 2.05 - 2.40 µm
	Mid-IR (Thermal IR)	3.50 - 4.16 µm 4.50 - 5.0 µm 8.00 - 9.2 µm 10.20 - 12.4 µm (8-14 for aerial sensing) 17.00 - 22.0 µm
	Far-IR	35.00 - 1 mm
Microwave		2.06 - 2.22 mm 7.50 - 11.5 mm 20.0 + mm

For remote sensing purposes the most important spectral regions are the 0.4 µm - 14 µm and the 2 mm - 0.8 m wavelength ranges lying in the optical and microwave range respectively. The sources for the energy in the ray region are radioactivity and cathode discharge tube; whereas the typical sources of the long wavelength regions are cavity resonators, oscillating dipoles, and electric circuits. The visible and infra-red have large variety of sources.

The visible region of the spectrum is called 'light' and extends from about 0.4 to 0.75 μm. This interval of wavelengths can be further subdivided into many components, each of which represents a colour. The following approximate values of colour band interms of wavelength are given by Mohr (1990);

Colour	Wavelength, micrometer
Violent	0.38 - 0.43
Blue	0.43 - 0.47
Cyan	0.47 - 0.51
Green	0.51 - 0.56
Yellow	0.56 - 0.59
Orange	0.59 - 0.62
Red	0.62 - 0.76

The particular colours perceived at or above the earth's surface by the eye or by a sensor capable of detecting in the visible spectral range are essentially the consequence of certain dominant reflection in one or more narrow wavelengths.

Hue, saturation, and brightness are the three characteristics of colour. Hue is the characteristic which causes one to describe a colour as red, yellow, green, etc. Saturation indicates the purity or amount of white in the colour, i.e. the ratio between the amount of hue in a colour and the total amount of energy in a colour; and brightness is a measure of the amount of black in a colour.

2.5. EFFECT OF THE ATMOSPHERE

How remote sensing data can be used to recognize different materials at the Earth's surface lies in the way in which electromagnetic radiation (EMR) interacts with matter. In satellite-mounted sensors using reflected solar radiation, the radiation must pass down through the atmosphere and then back again through the atmosphere before being received by the sensor. Even for the sensor measuring radiation emitted by the Earth, though the path is single, there is some effect of the atmosphere on EMR. The effect is caused by atmospheric scattering, atmospheric absorption, and atmospheric emission. These terms are explained by several authors such as Gupta, (1991); Durary, (1987) and Siegal et al, (1979).

2.5.1. Scattering

Scattering is a result of diffusion of radiation by matter. In the atmosphere, it is caused by interaction of gas molecules and suspended particles with EMR. The type of scattering depends on the size of the particles involved in the interaction. Scattering has no effect on the wavelength of the radiation.

Although many models were proposed the first type of scattering is explained by the Rayleigh Scattering model known as Rayleigh scattering (after its discoverer, Lord Rayleigh) or Molecular scattering. This type of scattering occurs due to the interaction of radiation mainly with gas molecules and tiny particles, smaller than the wavelength involved. It is inversely proportional to the fourth power of the wavelength, i.e., shorter wavelengths are scattered more than longer ones. The ultraviolet and blue end of the EMS are most affected by Rayleigh scattering, whereas on EM regions beyond 1 mm its effect is negligible, Rayleigh scattering is responsible for the blue colour of the sky.

In remote sensing, Rayleigh scattering causes high path radiance in the blue end of the spectrum resulting reduced contrast and unfocused pictures. This effect is reduced by using appropriate filters which eliminate the shorter wavelength radiations from reaching the detector unit.

The second type of scattering is known as Mie scattering or larger-particle scattering. It is caused by coarse suspended particles of a size larger than the wavelength involved. Dust particles and water vapour molecules are the main scatterer of this type. Mie scattering affects all wavelengths from ultraviolet to infrared but it has greater effect on the wavelength larger than blue light.

In addition to these, presence of aerosol, droplets in cloud or fog, which are much larger than most EMR wave length of interest in remote sensing, scatter all wavelengths in the visible and infrared spectrum. This type of scattering is known as non-selective scattering and responsible for the white colour of cloud and fog.

In general scattering makes interpretation more difficult since; a) atmospheric effects are more pronounced at some wavelengths than others, and cause distortion of spectral signatures. b) Presence of clouds can alter the radiance on a given target by either its own radiance contribution or by its shadowing effect. c) Haze reduces the contrast between adjacent surface features on imagery

2.5.2. Absorption

Significant amount of water vapour (H_2O), ozone (O_3) and carbon dioxide (CO_2) are found in the atmosphere. Interaction of electromagnetic radiation (EMR) with these in different ways cause a net effect of absorption of energy in specific wavelengths. This selective absorption of EMR by a particular type of gas occurs when the incident radiations' photon energy is just sufficient to cause a permissible energy level change.

The spectral regions of least absorption, or those wave bands that pass relatively undiminished through the atmosphere, are called atmospheric windows. These are the regions that can be used to look at ground surface and phenomena from aerial or space platforms across the atmosphere. Important atmospheric windows available for remote sensing are shown in fig.2.4.

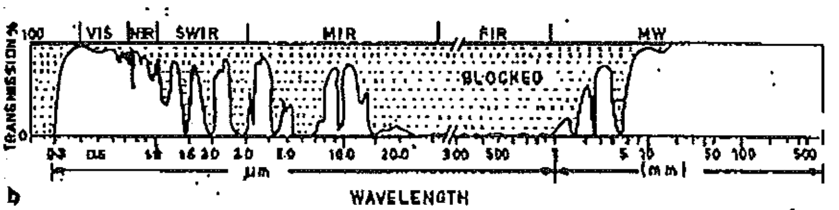

Fig.2.4. Transmission of radiation through the atmosphere: atmospheric windows are unstipled (Gupta, 1991).

Atmospheric windows occur throughout the EM spectrum at intervals. The visible part is marked by an excellent atmospheric window as well as high energy conditions (Fig.2. 4.) In the thermal infrared region, two important windows occur at 8.0 - 9.2 μm and 10.2 - 12.4 μm which are separated by an absorption band due to the ozone present in the upper atmosphere. Therefore, for sensing from aerial platforms the thermal channel in the range 8-14 μm can be used with isolated absorption left in between.

The atmosphere is opaque in the region 22 μm - 1 mm wavelength. The microwaves of wavelength greater than 20 mm propagated through the atmosphere with least attenuation.

2.5.3. Emission

The atmosphere emits EM radiation due to its thermal state. The spectra of emitted radiation is discrete because of its gaseous structure. At relatively lower temperatures the intensity of emission becomes significant only in the mid-IR spectral region, where it would tend to increase the path radiance. Path radiance acts as a background noise, superimposed over the ground signal. As spectral emissivity equals spectral absorptivity, the atmospheric windows are marked by low path radiance. The effect of self emission by the atmosphere can be significantly reduced by restricting the remote sensing observations to the good atmospheric windows.

To sum up, about 50% of the EM spectrum is unusable because most of the energy in these regions can not penetrate the atmospheric layer.

2.6. SPECTRAL RESPONSE AND SPECTRAL SIGNATURE OF MINERALS, ROCKS AND VEGETATION.

Every substance or class of related substances has its own specific spectral signature or spectral response curve. Each class of substance or feature shows some dominant signature or pattern by which members of a class can be identified (Fig.2.5). The signature of these members share some common traits but often show enough variation to allow identification of the individual type.

The energy incident on the earth which is reflected, absorbed and transmitted by the earth's materials, to various degrees, obeys the law of conservation of energy. The energy balance can be written as:

$$E_i(\lambda) = E_r(\lambda) + E_a(\lambda) + E_t(\lambda)$$

where $E_i(\lambda)$ is the spectral incident energy, $E_r(\lambda)$ is the energy component reflected, $E_a(\lambda)$ is absorbed, and $E_t(\lambda)$ is transmitted. The component E_r, E_a, and E_t differ for different wavelengths. These inherent differences build up the avenues for discrimination of objects by remote sensing through multispectral measurements.

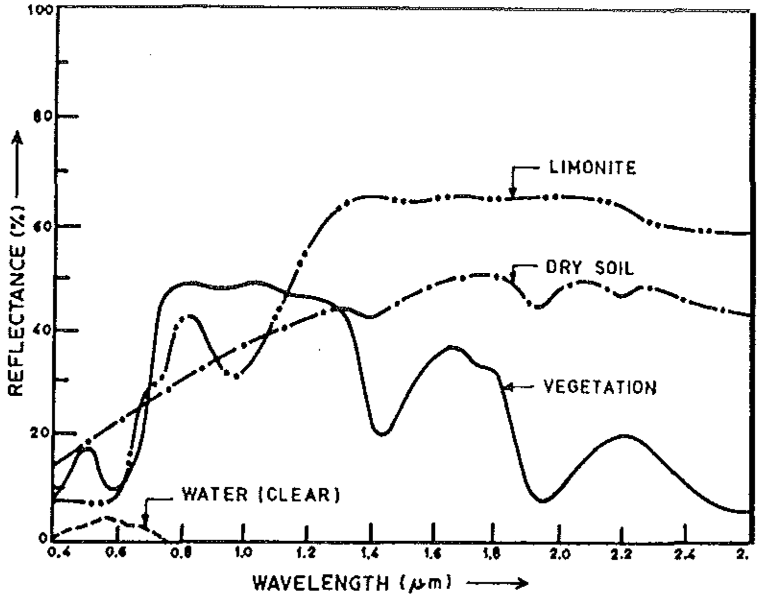

Fig.2.5. Typical spectral reflectance curves for selected common natural objects- water, vegetation and limonite (Gupta, 1991).

The basic principle involved in remote sensing methods is that in different wavelength ranges of the electromagnetic spectrum, each type of object reflects or emits a certain intensity of light, which is dependent upon the physical or compositional attributes of the object. It may be possible to differentiate between different types of objects using the information from one or more wavelength ranges (e.g. dry soil, vegetation, limonite area) (Fig.2.5), and map their distribution on the ground.

The intensity of light emitted or reflected by an object at different wavelengths is called its spectral response. These spectral data acquired from the remote sensors are processed, enhanced and interpreted for application. The graphic relation between the intensity of EM radiation with wavelength is called the spectral response curve (Fig.2.5). A single feature or group of features characteristic of this curve, is known as a spectral signature and is diagnostic in identifying the object.

In the context of remote sensing, objects can be marked by the following types behaviour in spectral response.

1. Selective absorption: If an EM spectrum is incident on an object some of the radiation may be absorbed preferentially. This phenomenon is widely observed in the solar reflection regions(Visible, Near-Infrared (NIR), Short wave-Infrared (SWIR)). Such spectral feature is marked by absorption or relatively weak reflection in comparison with responses at other wavelengths.

2. Selective reflection: from an entire incident wavelengths, a particular wavelength leads to a "resonance-like" phenomenon and is strongly reflected. If the selective reflection is intensive, it may lead to separation of the monochromatic beam called residual rays or Reststrahlen. Among from rocks and minerals this effect is typically observed in silicates at about 9-10 µm.

3. Selective high and low emission: certain objects may be marked by selective higher or lower emission at certain wavelengths.

In general, spectral signatures constitute the basic information needed for designing any remote sensing experiment or interpreting the data.

2.6.1. Spectra of minerals

The spectrum of minerals is governed totally by the effect of the following factors: spectra of dominant anions, spectra of dominant cations, spectra of ions occurring as trace constituents, and crystal field effect.

Hydroxyl ions show absorption band at about 2.74 - 2.77 µm, but the exact location may vary due to the crystal field effect (Fig.2.6). When hydroxyl ions occur in combination with aluminium and magnesium, several sharp absorption features in the 2.1 - 2.4 µm region are seen (Fig.2.8a).

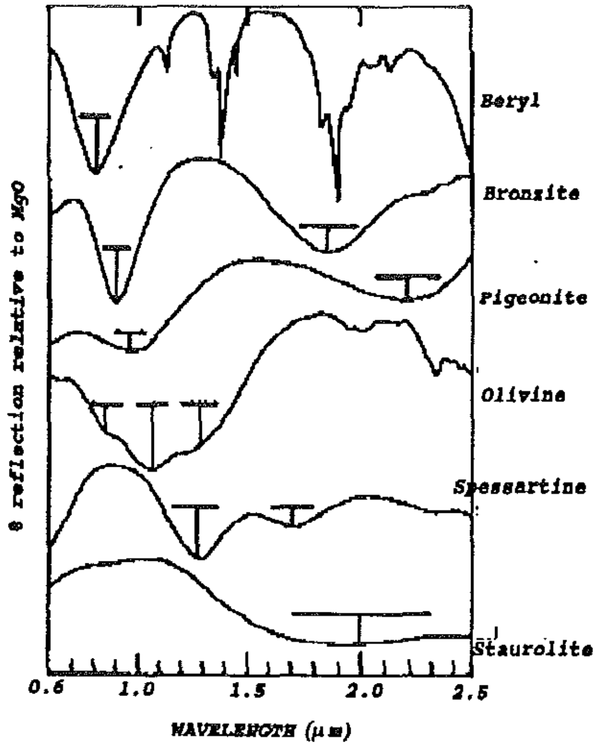

Fig.2.6. Location and appearance of features due to crystal field effect. In the reflection spectra of particular samples of these minerals, the ferrous ion is located in an aluminium octahedral six-fold co-ordinated site in beryl, in a distorted octahedral six-fold co-ordinated site in olivine, in an octahedral eight-fold co-ordinated site in spessartine, and a tetrahedral site in staurolite. The ferrous ion bands are indicated by vertical lines (Siegal, 1980).

Iron exhibits strong absorption of shorter wave lengths resulting in steep fall off in reflectance towards blue and a general rise towards infrared, with a maximum occurring in the 1.3 - 1.6 μm regions. It produces different absorption features at different wavelength due to crystal field effect (Fig.2.6).

Carbonates occur quite commonly in the earth's crust. Combination of 1.4 μm and 2.35 μm and an extra feature at 2.5 μm are diagnostic of carbonates (Fig. 2.8).

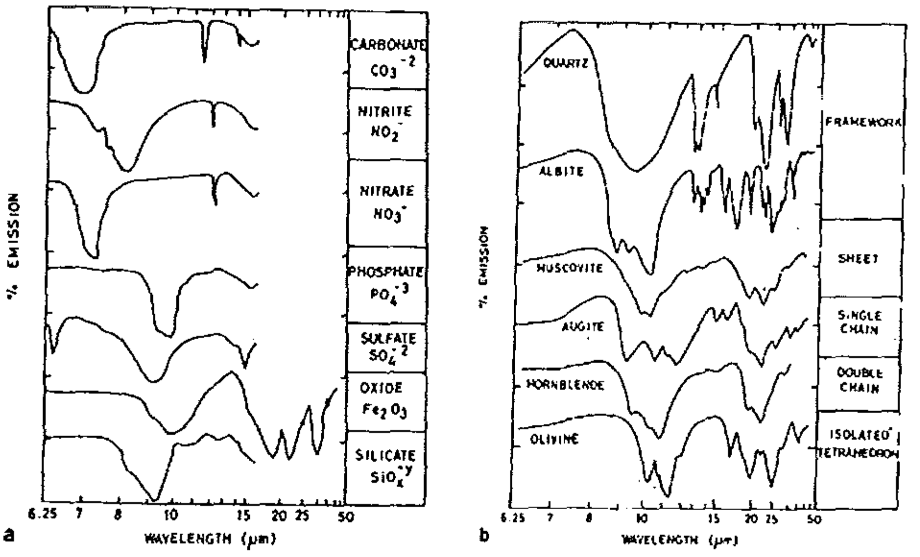

Fig.2.7. Thermal infrared spectra of the major anionic mineral groups. **a.** Carbonate, nitrite, phosphate, sulphate oxide and silicates (Chiristensen et al. 1986). **b.** Emission spectra of silicate minerals showing the correlation between band location and mineral structure (Gupta, 1991).

Water molecules and their characteristic combinations yield absorption bands at 1.9 μm and 1.4 μm. Sharp peaks imply that water molecules occur in well defined sites and when the peaks are broad, it means that they occur in unordered sites.

The EMR in the region 7 - 9 μm, where the earth's emission is the dominant source of radiation, is characterized by absorption features of silicates, carbonates, oxides, phosphates, sulphates, nitrates, nitrites, etc. (Fig.2.7a). Silicates show maximum peak called Christiansen peak, which migrates systematically with composition being at 7 μm for felsic minerals and at 9 μm for ultramafic minerals. In region 8.5 - 12 μm, the position of the peak is sensitive to silicate structures and shifts from nearly 9 μm (framework structure) to 11.5 μm (chain-silicates) being overall centred around 10 μm (Fig 2.7b).

The 12 - 15 μm region is sensitive to silicates and aluminium-silicate structures of the 'tectosilicate type'.

While other silicates show no absorption features in this region. From the point of view of remote sensing, the thermal-infrared (TIR) is the most potentially useful region for compositional investigations of terrestrial materials.

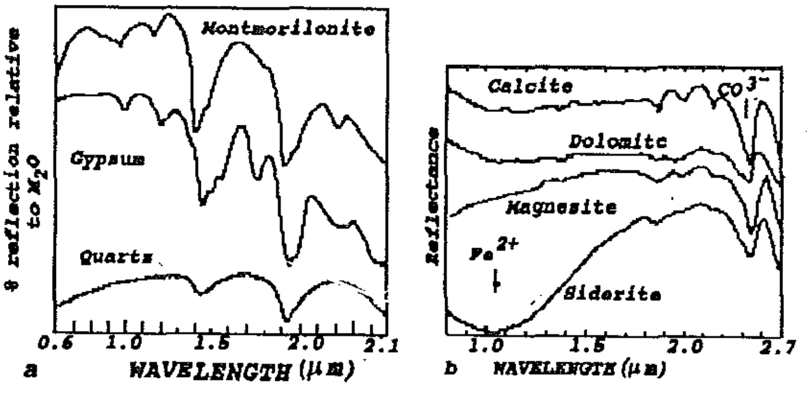

Fig. 2.8. Spectral features in the SWIR region. The region is marked by combination and overtone of vibrational features.
a) Reflectance spectra of selected water-bearing minerals: montimorilonite, gypsum and quartz.
b) Reflection spectra of carbonates-calcite, dolomite, magnesite and siderite (Gupta, 1991).

Generally anion composition, crystal lattice and physical properties affect the spectral band of the minerals.

2.6.2. Spectra of rocks

Defining the diagnostic spectral curve of rocks is difficult because of their complex composition. However, since different mineral groups are present in different rocks, it is possible to broadly describe the spectral character of the constituent minerals. Summary of the spectra of rocks in very-near-infrared (VNIR), short-wave-infrared(SWIR) and thermal-infrared (TIR) regions is given as follows:

In the VNIR and SWIR regions, solar reflection and spectral features are produced due to selective absorption of radiation by ionic constituents. Constituent minerals, their grain size and mixing, control the spectra of the rocks. In addition, depth of penetration which is 50 µm, easily affected by surface coating. Spectral characters of intimate polymineral mixtures are usually complex non-linear combination of optical properties of the end members. This implies that simple additive model may not be applicable for deriving the spectra of mixtures.

In the TIR regions, the bands from 8.0 µm to 14 µm are most useful. The emitted spectral energy depends on the bulk physical properties of the materials and the information is related to the top 10 cm depth surface zone. Hence, in these regions, spectral features of the bedrock material are observable even if surfacial coatings, encrustations, varnish, etc. are present. The mineral spectra are basically additive in this region, and therefore rock spectra are interpretable in terms of relative mineral abundance.

Igneous rocks:- graphic granites display bands at 1.4, 1.9 and 2.2 µm corresponding to vibrational and overtone combinations of OH and H_2O. Biotite granites and granites have less water, and therefore their absorption bands are weaker in VINR and SWIR. Mafic rocks contain ferrous and ferric ion in pyroxenes, amphiboles, and magnetite and, therefore, absorption bands at 0.7 µm, 1.0 µm appear. Ultra mafic rocks contain still larger amounts of opaque minerals and Fe^{2+}-bearing minerals, and therefore the ferrous band becomes still more prominent (Pyroxenite at 0.7 µm, 1.0 µm and 2.0 µm; dunite is almost all olivine and hence, there is a single broad absorption band at 1.0 µm). In TIR the centre of the minimum emission band gradually shifts from about 9 µm in granite to about 11 µm in olivine peridotite due to the shift of the Si-O absorption band in silicate minerals from framework to isolated tetrahedron type (Fig.2.10).

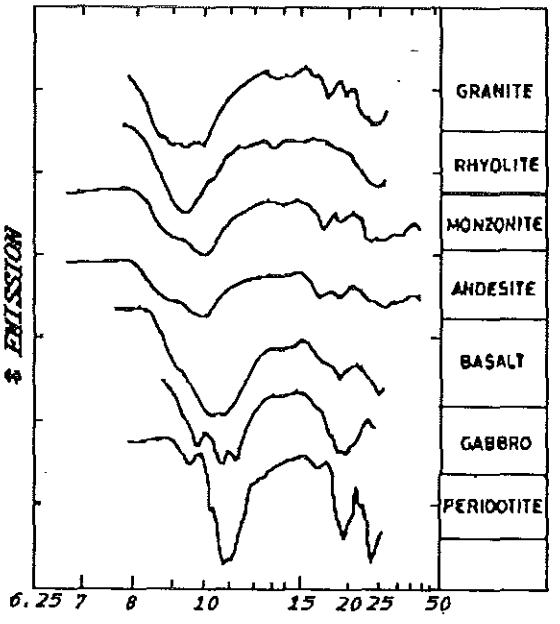

Fig. 2.9. Thermal infrared spectra of common rocks varying from high SiO_2 (granite) to low SiO_2 (peridotite). Note the systematic shift in the absorption band with varying SiO_2 content (Gupta, 1991).

Sedimentary rocks:- all sedimentary rocks have a hydroxyl-water absorption band at 1.4 and 1.9 µm, with varying intensity. Clay shales have additional absorption features between 2.1 and 2.4 µm due to Al-OH and Mg-OH. Presence of ferrous ions may produce further absorption features. Sandstone usually has some iron-oxide stains which produce spectral feature. Limestone is characterized by absorption bands of carbonates at 1.9 µm and 2.35 µm, the later being more intensive.

Metamorphic rocks:- the broad absorption due to ferrous ions is prominent in rocks like hornblendeschists and tremolite. Water and hydroxyl bands are found in schists whereas carbonate bands mark the marbles.

Alteration zones:- these zones are usually characterized by the presence of alteration minerals such as kaolinite, montimorilonite, sericite, muscovite, biotite, chlorite, alunite, zeolites, geothite, hematite, etc. These minerals can be broadly classed into five groups: framework silicates, sheet silicates, carbonates, hydroxyls and metal hydroxyl, and iron oxides. Abundance of Al-OH results in absorption bands in the 2.1 - 2.4 µm range. The spectral feature of this zone is characterized by the spectral value of the altered minerals present.

2.6.3. Spectra of vegetation

Plants use solar energy to convert water and carbon dioxide to carbohydrate and oxygen through the process of photosynthesis. The way they do this has a strong influence on their interaction with EMR. The abundance of water in their structure also controls these interactions.

The function of chlorophyll is to absorb solar radiation and thereby fuel photosynthesis. This is achieved by absorption near the 0.45 µm and 0.68 µm bands in the blue and red parts of the visible spectrum (Fig.2.5) which is why healthy leaves appear green. However, chlorophyll is unstable above a certain temperature. To protect it from thermal breakdown plants have evolved a means of balancing energy which is achieved by strong reflection of near infrared radiation partly by shiny coatings on leaves, but mainly by the internal cells themselves.

The structure of plant cells reflects up to 50% of the incident near-infrared radiation. The remainder is transmitted directly through the leaves. Water in the leaves, at its characteristic overtones around 1.4 and 1.9 µm (Fig.2.5), absorbs some energy; the absorbency depending on the proportion of water in the cells. Beyond 2.0 µm, leaves absorb near-infrared radiation.

The different cell structures, proportions of chlorophyll and other pigments, water content and surface morphology of different plants have marked effect on their spectral properties in the visible and NIR spectrum.

2.7 EMR interaction with water.

The response of water to EMR is rather different and the spectral response curve shows broad features. In the visible range, the interactions depends on reflectance property, illumination angle and the presence and nature of the waves.

Water has a high transmittance for all visible wavelengths, but the transmittance increases as the wavelength decreases. In deep water, only blue light penetrates beyond a certain depth, with longer wavelength having already been absorbed at shallower levels. In clear water, it is therefore, possible to estimate the depth from the intensity of visible radiation, particularly blue light, reflected from bottom. For depths greater than about 40 m, all visible radiation is absorbed and water bodies appear dark. Suspended sediments increase the reflectance of visible light from water. Hence, given the depth, it is also possible to estimate the amount of suspended material in water from remotely sensed data.

In the NIR region, water acts like a perfect blackbody (Fig.2.10). Even if they are shallow, or contain suspended material, they can be distinguished from other surface materials since they are the only natural materials with this property.

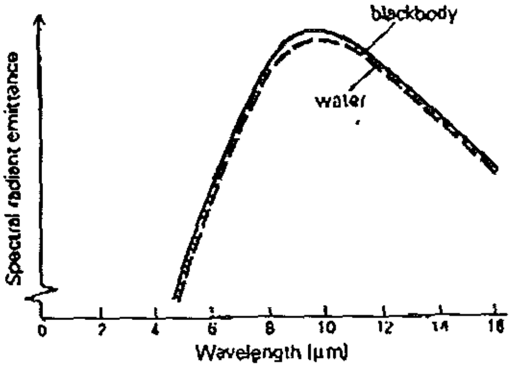

Fig.2.10. The spectral radiant emission of water reveal that it is a nearly perfect blackbody (Durary, 1987).

2.8. Principle of Resolution

Dissection in a regular format is essential for the transmission and computer-processing of many kinds of remotely sensed images. Image dissection by usual system has an important bearing on what the human visual system can and cannot see. Every kind of artificial image is also dissected and may be made either by the line raster of a television picture or as random grains of metallic silver in a photograph.

The elements of image interpretation depend on the acuity of the visual system, mental fusion, the degree of dissection of the image, its scale, and a combination of all these factors which is expressed as resolution. Therefore, resolution of a remote sensing system describes how close two objects are and can still be distinguished as individual entities. In photographic data products it is to denote the closest discriminable spacing of bright and dark lines of equal width.

In general there are two types of resolutions that should be considered during interpretation of remotely sensed data. Namely spatial resolution and spectral resolution. Spatial resolution is a measure of the smallest object that can be resolved by the sensor or the area on the ground represented by each pixel. For example, SPOT's (Satellite probatoire pour i'observation de la terre) 20m resolution provides information on features as small as individual houses, and that of MSS's (Landsat multispectral scanner) 80 m resolution allows to view features the size of a football field and larger, or linear features as small as highways. Spectral resolution refers to the specific wavelength intervals in the electromagnetic spectrum a sensor can record. The size of the interval or band may be as large as panchromatic black and white aerial photographs or as small as Landsat thematic mapper (TM) sensor system. Narrow-band sensors have a capability to give maximum separability between different surfacial materials.

3 Photography versus Imagery

3.1 Relative merits and limitations of:

3.1.1 Imagery

As there is a wealth of data gathering devices, so there has been a great range of platforms at which images of the earth have been taken. The quality, resolution, spectral range and form of the data also vary.

Earth images taken from space can be geometrically and radiometrically compared, except at large scales, to those obtained by airborne cameras. Simultaneous observation over large areas provides for images a new means of analysis of global and detailed works. Imagery opens extended and broad fields of application to its users. In addition to their coverage of the globe, they can be transmitted to users and at a much lower cost than airborne imagery. Production of remotely-sensed images of the earth is from unmanned satellites. These include METOSAT (ESA), MET3 (ESA), GOES-W (USA), GOES-E (USA), INSAT (INDIA), GMS (JAPAN), NOAA (USA), LANDSAT (USA), and SPOT (FRANCE). Some of these are non commercial and their data are open to any researcher. They carry instruments having different channels for sampling radiation at different EM regions.

The image sensed by the TM and MSS are transmitted continuously to the ground in digital form. The data from these sensors are arranged in successive scenes composed of a set of lines formed by adjacent picture elements covering a ground surface of 30 X 30 m (120 X 120 m in the thermal infrared) and 80 X 80 m respectively. These data are rescaled on the ground, and are transformed either to film, using a digital film writer, or to computer compatible tape (CCT). In both cases, the data used are in the range of 0 - 225 (8-bit precision) but only 64 different real ranges are possible in the data. A complete scene covers an area of 185 X 185 km.

Geometric Characteristics of TM, MSS and SPOT images

TM

Ground resolution 30 X 30 m(120 X 120 M in thermal infrared)

Complete scene coverage 185 X 185 km

MSS

Ground resolution 80 X 80 m

Complete scene coverage 185 X 185 km

SPOT

Ground resolution 20 X 20 m

Complete scene coverage 60 X 60 km

Radiometric characteristic(spectral range (μm)):

TM

Band 1	0.45 - 0.52
Band 2	0.52 - 0.60
Band 3	0.63 - 0.69
Band 4	0.70 - 0.90
Band 5	1.55 - 1.75
Band 7	2.08 - 2.35
Band 6	10.40 - 12.50

MSS

Band 1	0.5 - 0.6
Band 2	0.6 - 0.7
Band 3	0.7 - 0.8
Band 4	0.8 - 1.1

SPOT

Band 1	0.50 - 0.59
Band 2	0.61 - 0.69
Band 3	0.81 - 0.91

Capability

TM

Band 1: to map coastal water areas, to differentiate between soil and vegetation and even to differentiate among different vegetation.

Band 2: to measure the health status of vegetation.

Band 3: to differentiate between plant species.

Band 4: for water body delineation.

Band 5: to measure vegetation and soil moisture and to differentiate cloud cover from snow cover.

Band 6: to map thermal areas.

Band 7: for hydrothermal mapping, rock type discrimination.

MSS

Band 1: emphasizes on movement of sediment-laden water and shallow waterbodies, shoals and reefs etc.

Band 2: to map cultural features and sometimes bare soil surfaces.

Band 3: emphasis on vegetation and landform

Band 4: emphasis on vegetation and clear land- water boundaries and also land forms.

SPOT

Band 1: to measure the health status of vegetation, to study water details in shallow areas.

Band 2: for plant differentiation

Band 3: for biomass studies, water body delineation.

3.1.2 Photography

Aerial photographs are the most easily available of all remotely sensed data, and have been acquired at various scales for much of the land area of the Earth. The basic form of an aerial photographic survey consists of a number of approximately parallel flight lines, along which exposures timed to give at least 60% overlap between successive photographs, and whose spacing is such that adjacent lines of images have sufficient sidelap to ensure complete coverage. More often than not an aircraft cannot maintain a perfect course, because of cross winds and turbulence; the aircraft may rise or fall, changing the scale of each image; and it may pitch or roll, imparting a tilt to each image, which produces unreal slope in the stereo model.

In addition for security reasons some countries maintain a tight hold over their aerial photography, so they have been obtained routinely.

Scales may vary, as might the angle of solar illumination on time of day, location and season. Enlarged prints can be ordered but the very fine grain and large format films used in aerial surveys can sustain enlargement up to ten times the contact scale. However, enlargement may render stereoscopic viewing difficult.

In the case of large-scale original frames, reduced mosaics of photographs can sometimes be obtained on a routine basis. Again, this removes their stereoscopic potential.

3.2 Significance of Imagery in comparison to photography in Geologic applications.

The best images for geological work should have the lowest possible cover of cloud or snow, and have a good contrast and low-angle illumination. However the separability of materials in images depend on the relative photographic tone which is a measure of the reflectivity in the recorded wavelength region. Maximum contrast occurs when two materials have large reflectivity difference over the sensed spectral region. But, spectral differences are more evidenced at narrower absorption bands and therefore the width of the sensed wavelength region is crucial. Thus, by narrowing the sensed wavelength region, better separation of materials can be expected.

Black and white aerial photographs record spectral information in the broad wavelength region of 0.5 to 0.7 μm. The relative photographic tones represents the average reflectance of the materials detected by the sensor; and this implies poor separability of materials as compared with imageries which are recorded in narrow wavelength regions.

Aerial photographs are generally taken with a particular objective, such as cartographic or periodic inventories of land use. There is therefore no guarantee about the suitability of airial photographs for a specific kind of geological work.

Images provide extra dimension for discrimination of different rocks, soils and vegetation. They can be used in three main ways for investigating geological features:

1. They might be interpreted in just the same way as photographs.
2. Images of the same area taken at different times of the day give semi-quantitative information about how different materials respond to heating and/or cooling.
3. They show troughs in the emission spectra of minerals depending on chemical composition and molecular structure.

4. DIGITAL IMAGE PROCESSING OF TM IMAGE OF NORTH-WESTERN MEKELE AREA.

4.1 General

To extract the desired information from the raw digital image data different processing techniques are required. For this study, SPOT, landsat TM and MSS data were available in digital format. SPOT images were preferred for their high resolution which helps us to identify the continuity of selected marker beds throughout the area. TM were also preferred for the following reasons:

1) The 30 m resolution of TM bands was acceptable for outlining different structures.

2) TM band 5 and 7 are very important intervals in EMS for geological investigations.

And landsat MSS were chosen to be able to identify geological interests at regional scale.

Generally, bands are individually informative and collectively minimally redundant. Thus it is very important to select the proper bands which lead to extract the maximum geological information. The selection is the process of transformation of raw multispectral data to reduced form, without losing any of the essential information.

Most of the information extraction techniques depend on analysis of the spectral reflectance properties of images and employ special algorithms designed to perform various types of spectral analyses.

4.2 Image Histogram

It is an expression of how the EM energy reflected by the surface is distributed in the image. Histogram of an image provides information about the quality of the original data, whether it is low or high in contrast, whether it is affected by haze or not, whether it is multimodal in nature or not. It is drawn as a range of values on the abscissa while the frequency of the occurrence of each of these values are shown on the ordinate.

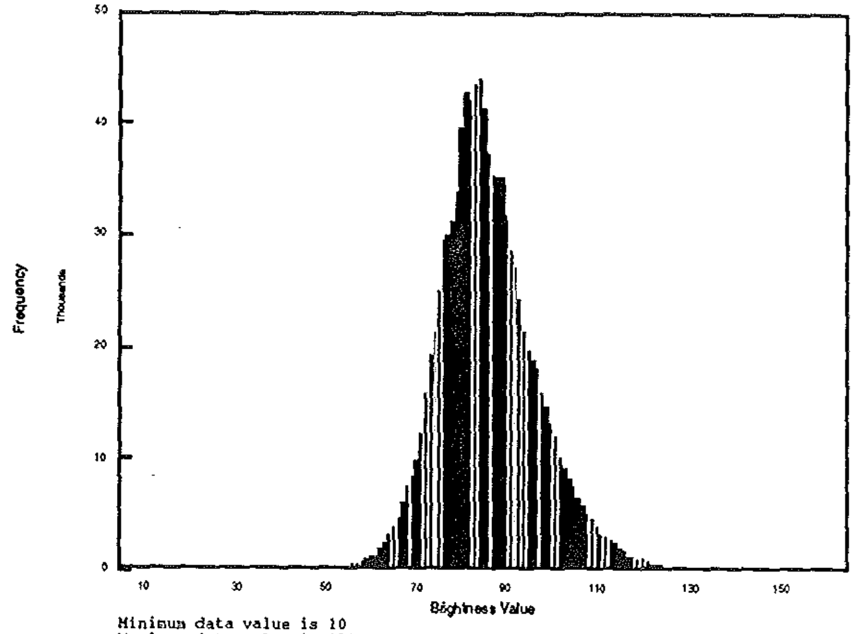

Minimum data value is 10
Maximum data value is 159
Mean = 85.87669
Standard Deviation = 10.84078
Median = 85
Mode = 84

a) Band 1

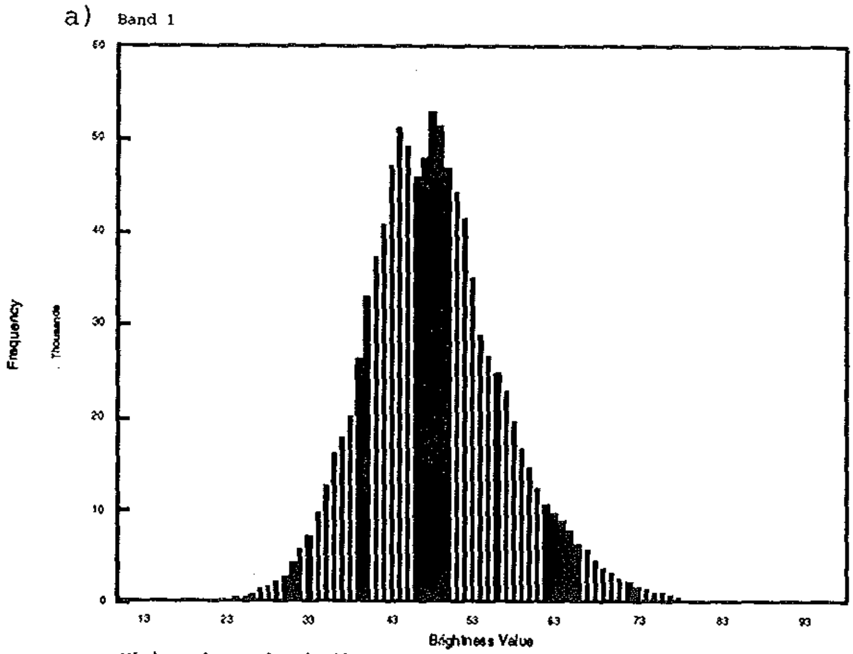

Minimum data value is 13
Maximum data value is 95
Mean = 48.32079
Standard Deviation = 8.598738
Median = 48
Mode = 48

b) Band 2

Fig. 4.1. Histograms of the original TM bands.

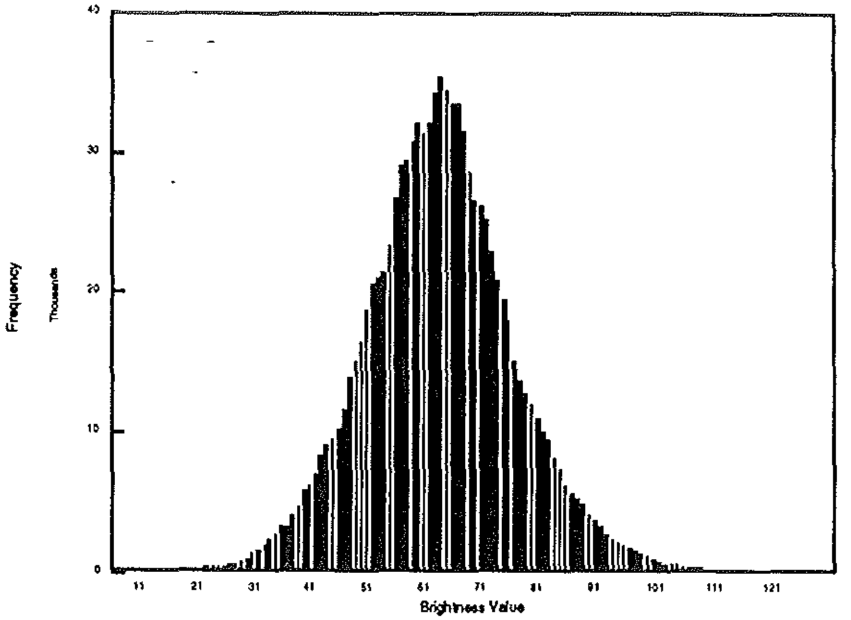

Minimum data value is 11
Maximum data value is 128
Mean = 63.82092
Standard Deviation = 12.91131
Median = 64
Mode = 64

c) Band 3

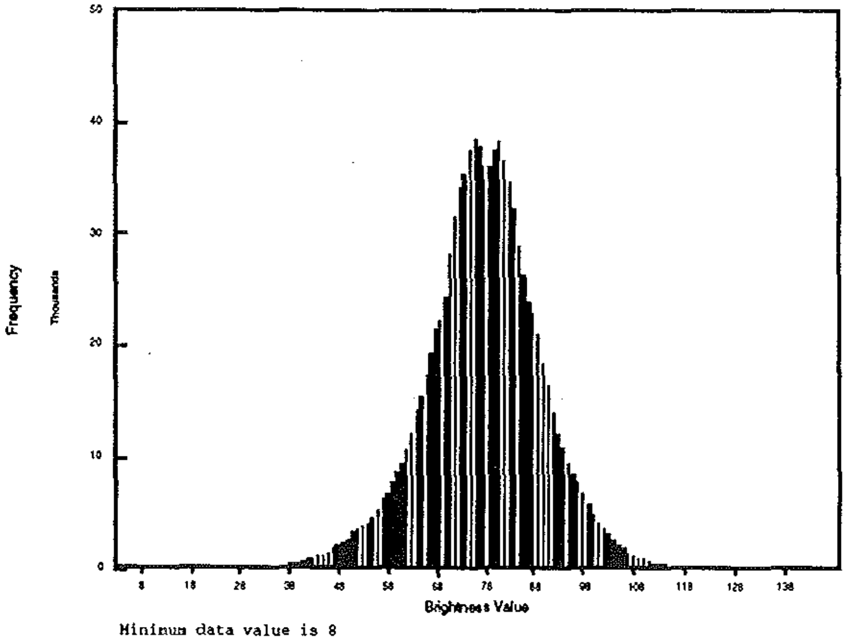

Minimum data value is 8
Maximum data value is 144
Mean = 77.58244
Standard Deviation = 11.90262
Median = 78
Mode = 76

d) Band 4

Fig. 4.1. Histograms of the original TM bands (Cont'd).

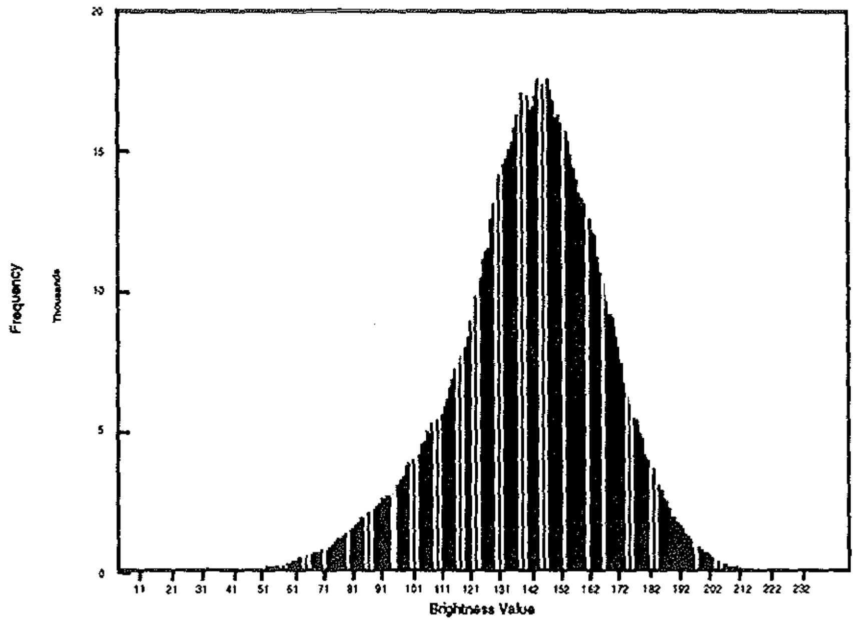

Minimum data value is 11
Maximum data value is 239
Mean = 141.0863
Standard Deviation = 25.76819
Median = 143
Mode = 148

e) Band 5

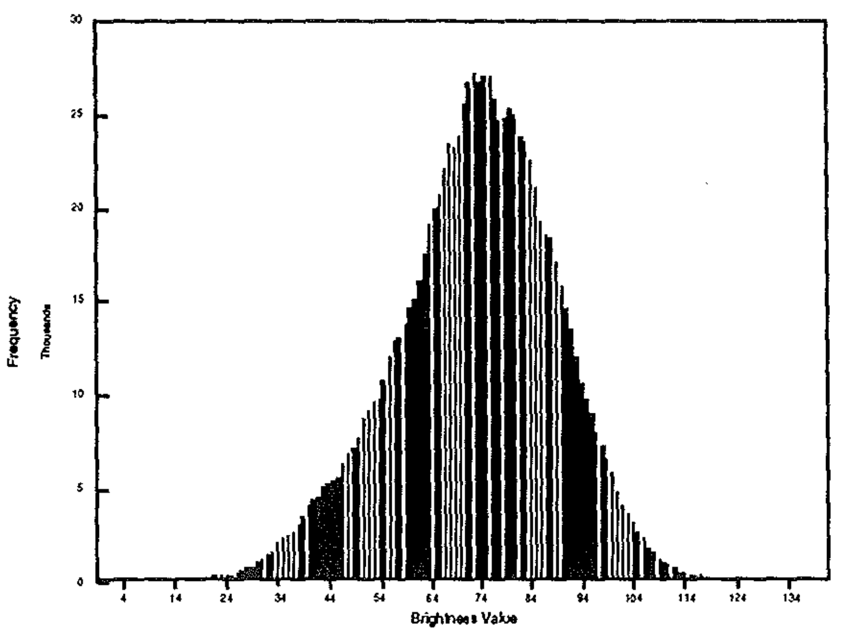

Minimum data value is 4
Maximum data value is 137
Mean value = 73.07256
Standard Deviation = 15.85021
Median = 74
Mode = 73

f) Band 7

Fig. 4.1. Histograms of the original TM bands (Cont'd).

The histograms of the original TM bands are shown in fig.4.1a-g. They are produced using ERDAS statistics module. Histogram's shape indicates the contrast and homogeneity of the scene. The position of the data that will fall into the restricted range of 0 to 255 suggests low contrast (Fig.4.1a). The various peaks and valleys, in the multi-modal histogram correspond to dominant type of land cover in the image.

4.3 Geometric Rectification

Any remote sensing image has to be geometrically corrected to refer it to other maps. Geometric rectification of images needs ground control points. The selection of these points is important and depends basically on the precession of identification of the object on both the image and on the map, which is in fact most difficult thing to do. 17 points have been selected both on the image and topographic map (Table 4.1). In the process of ground control point selection problems were faced because the topographic map of the study area had a scale of 1:250,000 and published back in 1972. Many changes have occurred since then and it was sometimes difficult to identify corresponding features of the image on the topographic map.

The correction is performed with first order of transformation and Root Mean Error of 3. From the selected ground control points 8 were correctly identified. The final image is corrected with these points (Table 4.1.b).

Table 4.1.a. Ground control points

Point count	Point number	X	Y	Image Pixel X	Image Pixel Y
1	1	548000	1512250	879.3750	379.8750
2	2	525750	1525000	41.1250	61.1250

3	3	516750	1498750	35.8750	363.1250
4	4	556750	1517500	1157.8750	155.8750
5	5	561250	1501500	1412.1250	690.1250
6	6	544250	1511500	758.8750	431.1250
7	7	523000	1510000	22.6250	599.1250
8	8	534750	1525250	358.0000	5.0000
9	9	539250	1510250	594.0000	500.0000
10	10	529750	1521250	201.3750	174.3750
11	11	542750	1504250	738.0000	680.0000
12	12	552000	1504000	1064.0000	648.0000
13	13	555500	1508750	1164.0000	472.0000
14	14	556500	1517000	1170.0000	172.0000
15	15	552500	1518750	999.0000	135.0000
16	16	562000	1520750	1331.0000	12.0000
17	17	554750	1520750	1067.0000	51.0000

Order of transformation is 1.

Table 4.1.b. The following are the points that were used.

Point count	Point number	X	Y	Image Pixel X	Image Pixel Y
1	1	548000	1512250	879.3750	379.8750
2	2	525750	1525000	41.1250	61.1250
3	17	554750	1520750	1067.000	51.00000
4	4	556750	1517500	1157.8750	155.8750
5	12	552000	1504000	1064.0000	648.1250
6	15	552500	1518750	999.0000	135.1250
7	7	523000	1510000	22.6250	599.1250
8	10	529750	1521250	201.3700	174.370

Order of transformation is 1.

-0.1010419E+02	0.5578964E+02
0.3468436E-01	-0.5470833E-02
-0.5305328E-02	-0.3465564E-01

The computed result of the above is

Point count	Point number	Image Pixel X	X-pixel residual	Image Pixel y	Y-pixel residual
1	1	879.86	0.4867E+00	383.62	0.3749E+01
2	2	40.49	-0.6332E+00	63.49	0.2365E+01
3	17	1068.89	0.1886E+01	52.12	0.1122E+01
4	4	1155.50	-0.2378E+01	153.81	-0.2063E+01
5	12	1062.37	-0.1632e+01	647.65	-0.3507E+00
6	15	1001.46	0.2457E+01	133.74	-0.1257E+01
7	7	24.69	0.2065E+01	598.37	-0.7554E+00
8	10	199.12	-0.2251E+01	171.57	-0.2810E+01

X RMS error = 1.86672 Y RMS error = 2.10148

Total RMS error = 2.81085

Point count	Point number	Error	Error contribution by point
1	1	3.7800	1.3448
2	2	2.4484	0.8711
3	17	2.1946	0.7808
4	4	3.1485	1.1201
5	12	1.6691	0.5938
6	15	2.7596	0.9818
7	7	2.1985	0.7822
8	10	3.6000	1.2807

4.4 Image Enhancement

To increase the interpretative nature of an image, a number of operations are designed. Any operation that modifies an image to obtain an idealized output of some part of the original scene is image enhancement. This operation falls between detection or recognition of the existence of a relevant feature and the interpretation and classification of that feature (Siegal et. al., 1980). We used different enhancement operations to essentially improve or ease the interpretation of a scene under study relative to some specific information.

4.4.1. Contrast Enhancement

Contrast enhancement is one of the most widely used image processing techniques in lithological mapping. It is done by maximizing the display of information for each component in the entire scene.

The original input brightness is expanded to make use of the total range or sensitivity of the output device. When the data, original bands, are displayed on CRT without any contrast enhancement, we use less than one-half of the full range of brightness values that could be displayed (Fig. 4.1b). In this band, brightness values between 0 and 13 and between 95 and 255 are not used. The image is rather dark, low in contrast. It would be difficult to visually interpret such an image. Thus to increase the visual interpretability all images are linearly stretched since their histograms are more or less Gaussian or nearly Gaussian type. The resulting histograms of the enhanced images, which are produced using DIMPLE analysis module, are shown in figure 4.2.a-f.

	Selected	Cumulative
n	996872	996872
$\bar{x}$	113.5706	113.5706
min.	0	0
max.	255	255
mode	112	112
median	112	112
Σx	113215400	113215400
σ_n	37.3730	37.3730
σ_{n-1}	37.3730	37.3730

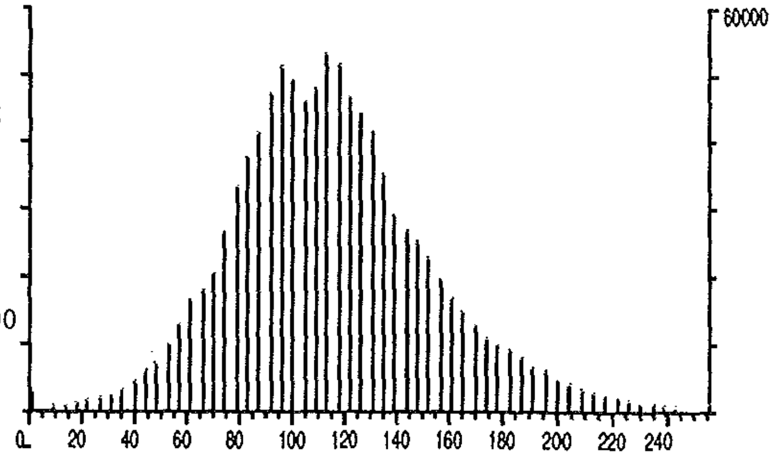

a) band 1

	Selected	Cumulative
n	996872	996872
$\bar{x}$	105.2699	105.2699
min.	0	0
max.	255	255
mode	98	98
median	101	101
Σx	104940641	104940641
σ_n	37.4667	37.4667
σ_{n-1}	37.4667	37.4667

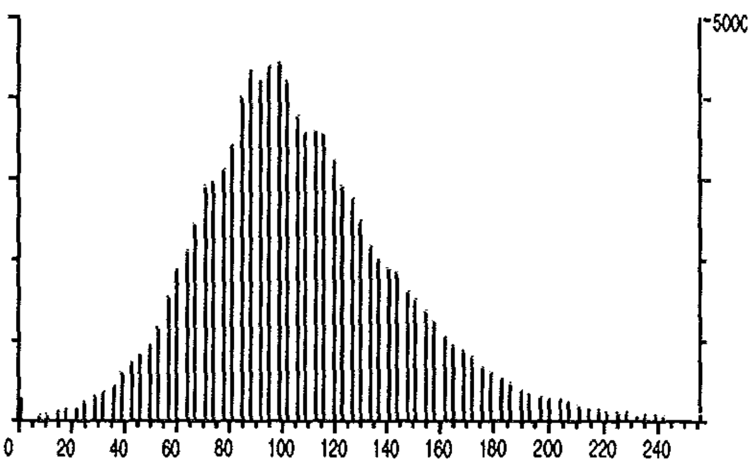

b) band 2

Fig. 4.2 a-f Histograms of the enhanced TM images.

	Selected	Cumulative
n	: 996872	996872
$\bar{x}$	: 117.9399	117.9399
min.	: 0	0
max.	: 255	255
mode	: 119	119
median	: 119	119
Σx	: 117570999	117570999
σ_n	: 38.4824	38.4824
σ_{n-1}	: 38.4825	38.4825

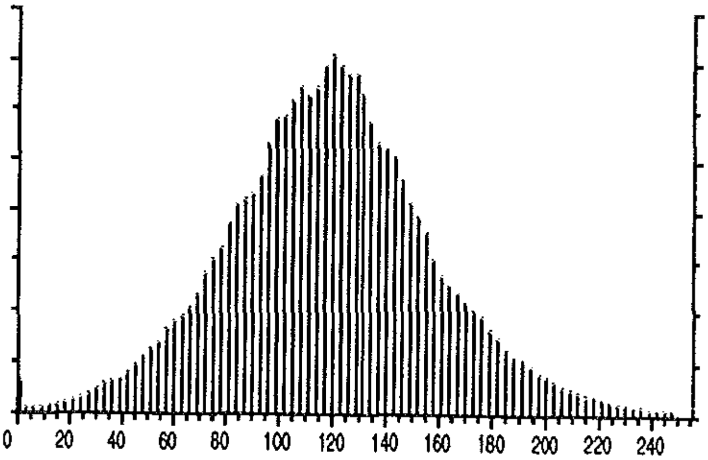

c) band 3

	Selected	Cumulative
n	: 996872	996872
$\bar{x}$	: 130.7281	130.7281
min.	: 0	0
max.	: 255	255
mode	: 126	126
median	: 132	132
Σx	: 130319225	130319225
σ_n	: 36.6502	36.6502
σ_{n-1}	: 36.6502	36.6502

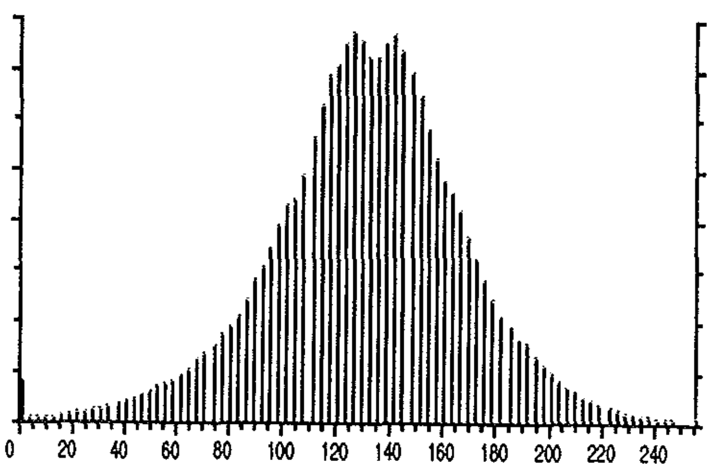

d) band 4

Fig. 4.2 a-f Histograms of the enhanced TM images(cont'd)

		Selected	Cumulative
n	:	996872	996872
$\bar{x}$	:	141.2010	141.2010
min.	:	0	0
max.	:	255	255
mode	:	152	152
median	:	144	144
Σx	:	140759286	140759286
σ_n	:	39.4369	39.4369
σ_{n-1}	:	39.4369	39.4369

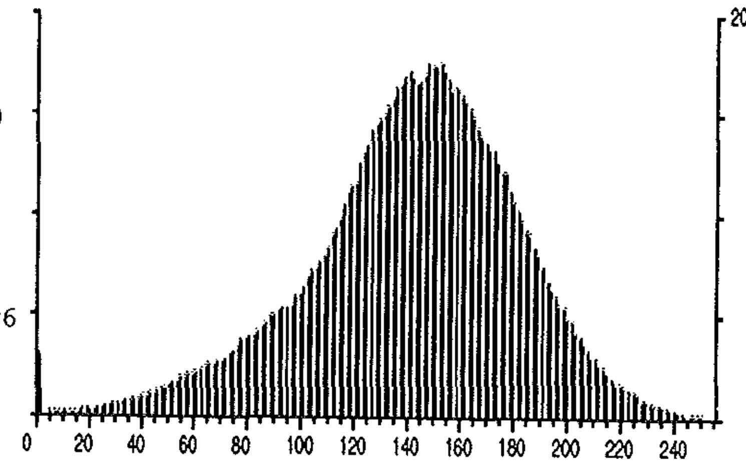

e) band 5

		Selected	Cumulative
n	:	996872	996872
$\bar{x}$	:	133.8522	133.8522
min.	:	0	0
max.	:	255	255
mode	:	134	134
median	:	136	136
Σx	:	133433506	133433506
σ_n	:	40.3869	40.3869
σ_{n-1}	:	40.3869	40.3869

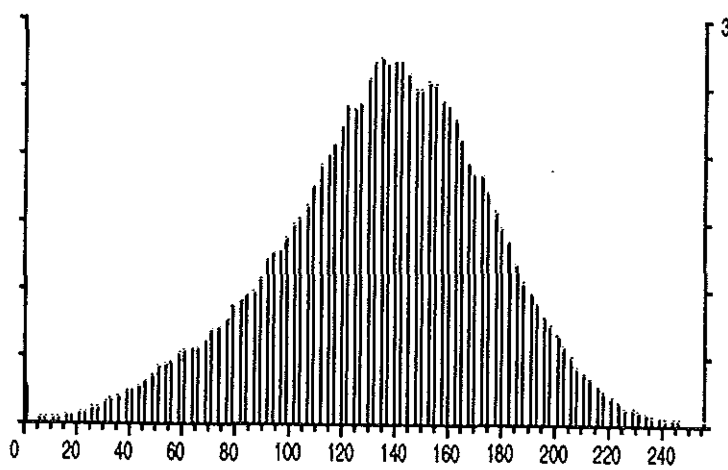

f) band 7

Fig. 4.2 a-f Histograms of the enhanced TM images (cont'd).

4.4.2 Band Ratio

Theoretically, any surface should receive the same proportion of energy in all wave bands, irrespective of its orientation to the sun. It should also reflect energy in the same proportion controlled by its spectral reflectance properties. But, on remotely sensed images the common problem is the effect of varying illumination caused by topography. Where there is appreciable relief, slopes facing the sun are more strongly lit than horizontal surfaces are, and those facing away from the sun receive less radiation. As a result a surface with uniform reflectance properties will show varying brightness value across a scene. In a scene with many different surface types, this can lead to increased confusion both in detailed visual interpretation and in computer assisted classification.

Though ratioing suppresses the difference of the overall ability of a material to reflect radiation of all wavelengths, it is used to reduce the variable effect of illumination caused by topography. The ratio values of shorter wavelength to longer wavelength are found to be decrease with distance. That means in poorly illuminated areas, the ratio values are higher in comparison to those in well-illuminated areas since the path radiance is higher to wards shorter wavelengths. It is important to be recognizant of the general types of materials found in the scene and their spectral properties to select the best ratio images for interpretation.

Images were rectified for path radiance components before constructing a ratio image. All the possible image ratioing among the six bands of TM were done. But, in most of the ratio values the effect of variation in illumination due to topography is not completely removed.

4.4.3 Principal Component Analyses

Correlation between images is common in remotely sensed data (Table 4.3), and only three bands are used to characterize earth surface reflectance from any available number of bands in RGB representation. Thus to overcome data redundancy and to choose the appropriate three bands, principal component analysis is helpful. It is a method of improving the spread of data by redistributing them about another set of axes in multidimensional space, to maximize the separation of difference in the data. The procedure includes setting the means to zero by shifting the axes and setting the variance between the bands to zero by transformation of covariance matrix. This process leads to decorrelation by spreading the data to the limits of the new principal component. The variation within the data on PC, known as eigen value, is recasted as variance on principal components. PC transformation provides statistically the optimum weight factors for linear combination, so that new features axes are orthogonal to each other.

Components are statistical abstraction of the variability inherent in the original band set and ordered in terms of the amount of image variation they can explain. The components produced by PCA are uncorrelated with one another and are ordered in terms of the amount of image variation they can explain. PCA produces compacted data by retaining only the first few components so that one can preserve most of the information while throwing away a large proportion of the data.

Therefore, the original six bands of TM were projected onto 6 new principal components by using loading factors for the contribution of each band to a component (eigenvectors).

Table 4.2. Variance - Covariance matrix.

Var/Covar	Band 1	Band 2	Band 3	Band 4	Band 5	Band 7
Band 1	124.51	95.13	136.78	110.02	246.74	145.43
Band 2	95.13	77.14	112.62	90.17	204.51	121.04
Band 3	136.78	112.62	172.23	133.75	315.02	187.86
Band 4	110.02	90.17	133.75	149.99	262.18	138.65
Band 5	246.74	204.51	315.02	262.18	691.21	409.33
Band 7	145.43	121.04	187.86	138.65	409.33	256.43

Table 4.3. Correlation matrix

Cor Matr	Band 1	Band 2	Band 3	Band 4	Band 5	Band 7
Band 1	1.0000					
Band 2	0.9707	1.0000				
Band 3	0.9341	0.9771	1.0000			
Band 4	0.8051	0.8384	0.8322	1.0000		
Band 5	0.8411	0.8857	0.9130	0.8143	1.0000	
Band 7	0.8108	0.8573	0.8905	0.7041	0.9685	1.0000

Table 4.4. Contribution of each Eigenvector to each Components.

Component	Comp. 1	Comp. 2	Comp. 3	Comp. 4	Comp. 5	Comp. 6
% var.	89.24	5.62	3.85	0.84	0.26	0.20
eigenval.	5.35	0.34	0.23	0.05	0.02	0.01
eigvec.1	0.4094	-0.2348	-0.5225	-0.6222	-0.0557	-0.3376
eigvec.2	0.4222	-0.1551	-0.3489	0.1894	0.1330	0.7889
eigvec.3	0.4235	-0.0170	-0.2069	0.7277	-0.1727	-0.4671
eigvec.4	0.3798	-0.6211	0.6469	-0.0428	0.2134	-0.0651
eigvec.5	0.4136	0.3688	0.3503	-0.1908	-0.7102	0.1717
eigvec.6	0.3994	0.6315	0.1460	-0.0958	0.6321	-0.1084

Table 4.5. Loading factor

Loading	Comp. 1	Comp. 2	Comp. 3	Comp. 4	Comp. 5	Comp. 6
Band 1	0.9474	-0.1363	-0.2512	-0.1393	-0.0069	-0.0367
Band 2	0.9769	-0.0901	-0.1677	0.0424	0.0165	0.0859
Band 3	0.9800	-0.0098	-0.0995	0.1629	-0.0214	-0.0508
Band 4	0.8789	-0.3605	0.3110	-0.0096	0.0264	-0.0071
Band 5	0.9570	0.2141	0.1684	-0.0427	-0.0880	0.0187
Band 7	0.9241	0.3666	0.0702	-0.0215	0.0783	-0.0118

Table 4.2 - 4.5 Summarizes Variance-covariance matrix, correlation matrix, eigenvector and eigenvalues, and loading factor of Landsat TM bands respectively. The loading refers to the degree of correlation between these new components and the original bands. Positive loading factors indicate that the components are roughly an average of all the bands. Negative loading factor for certain bands and positive for others indicate that the components emphasise the difference in spectral responses.

The highest eigenvalue is associated with the first component, and progressively lower eigenvalues with each higher order component (Table 4). In the result, the first PC is generally a weighted average of all the channels. Table 4.5 gives the contribution of each band for each component. It is observed that all six bands, in differing proportions, constitute the first PC. The other PCs are generally differece of various bands; the third PC, for example, is about the difference between the visible and infrared bands, and so on.

4.4.4 Vegetation Indices

Band ratios of TM brightness values have been used to estimate and monitor green biomass (Jonson, 1986). Normalized difference of brightness values for TM band 5 and 2, and band 7 and 4 are computed. The resulting images are considered in the image analysis.

Figure 4.3 shows the distribution of vegetation through out the area. This image is produced using the formula 127 + ((Band 3 - Band 4)/(Band 3 + Band 4)) X 127.

4.5. Selection of Training Site

To pave the way for supervised classification representative training sites must be selected, and their statistics should be analysed to select the appropriate bands to be used in classification process. Therefore, in the study area, training polygons have been chosen according

Fig. 4.3. Vegetation index map of the study area.Dark gray colour represents the distribution and effect of vegetation as well as topography (shadow) throughout the area.

to their tonal and textural homogeneity on the false colour composite (FCC) of PC 156 and TM bands 532 in RGB on the one hand and field survey on the other. Thirty-one training sites were chosen to represent 10 information classes. The number of pixels in each training set is taken into consideration not to violate the conventional image processing rule which requires the number of pixels in each training set must not be less than ten times the number of training sites.

Multivariant statistical parameters (means, standard deviations, covariance matrices, etc.) are calculated for each training site (Table 4.6). The result indicates that all signatures are included inside feature of interest in the acceptable range.

Table 4.6. Training set statistics

Basalt 1	No. Pixel	Minimum	Mean	Maximum	Std. Dev
Chan1:	768	55	78.39	125	11.01
Chan2:	768	23	41.82	76	8.33
Chan3:	768	35	76.83	111	12.48
Chan4:	768	45	103.75	179	21.03
Chan5:	768	20	45.93	87	11.07
Chan6:	768	65	120.68	203	21.49
Chan7:	768	60	102.41	175	18.23
Chan8:	768	61	106.82	186	17.65
Chan9:	768	90	146.29	203	20.18
Chan10:	768	142	189.80	222	9.86
Chan11:	768	51	121.16	183	23.23
Chan12:	768	25	51.63	98	13.12

Training set covariance matrix

	Chan 1	Chan 2	Chan 3	Chan 4	Chan 5	Chan 6	Chan 7	Chan 8	Chan 9	Chan 10	Chan 11	Chan 12
Chan 1	121.13	89.63	88.82	218.46	112.92	230.27	-94.40	-119.55	-72.23	-0.95	131.27	138.84
Chan 2	89.63	69.46	76.60	164.89	82.17	177.22	-56.16	-84.63	-37.01	-6.18	78.02	107.57
Chan 3	88.82	76.60	155.65	180.85	70.60	208.14	76.00	-24.25	-8.79	-3.76	-67.73	115.62
Chan 4	218.46	164.89	180.85	442.48	223.63	11.00	-112.43	-237.40	-93.11	-373.56	255.32	255.35
Chan 5	112.92	82.17	70.60	223.63	122.52	216.90	-92.33	-118.96	-58.97	29.24	181.80	126.96
Chan 6	230.27	177.22	208.14	11.00	216.90	-392.51	-113.51	-214.17	-110.62	-1615.12	197.91	275.31
Chan 7	-94.40	-56.16	76.00	-112.43	-92.33	-113.51	332.38	194.77	52.95	-44.02	-330.39	-95.48
Chan 8	-119.55	-84.63	-24.25	-237.40	-118.96	-214.17	194.77	225.94	44.88	-210.08	-251.36	-147.72
Chan 9	-72.23	-37.01	-8.79	-93.11	-58.97	-110.62	52.95	44.88	-1899.95	-6151.87	-136.97	-93.83
Chan 10	-0.95	-6.18	-3.76	-373.56	29.24	-1615.12	-44.02	-210.08	-6151.87	-53818.36	2057.96	-9.93
Chan 11	131.27	78.02	-67.73	255.32	181.80	197.91	-330.39	-251.36	-136.97	-2057.96	453.95	127.11
Chan 12	138.84	107.57	115.62	255.35	126.96	275.31	-95.48	-147.72	-93.83	-9.93	127.11	172.19

Basalt 2

Chan1:	1200	50	69.20	105	7.74
Chan2:	1200	19	34.13	60	5.73
Chan3:	1200	27	57.38	101	10.20
Chan4:	1200	34	86.84	155	21.22
Chan5:	1200	15	42.69	77	11.45
Chan6:	1200	54	100.40	170	17.83
Chan7:	1200	62	88.98	129	10.05
Chan8:	1200	62	112.08	146	12.14
Chan9:	1200	81	133.49	186	16.86
Chan10:	1200	134	191.05	225	14.49
Chan11:	1200	95	146.07	208	20.07
Chan12:	1200	21	42.25	77	9.04

Training set covariance matrix

	Chan 1	Chan 2	Chan 3	Chan 4	Chan 5	Chan 6	Chan 7	Chan 8	Chan 9	Chan 10	Chan 11	Chan 12
Chan 1	59.84	43.36	68.41	153.39	81.38	134.96	26.95	-35.27	-50.86	68.33	85.31	68.22
Chan 2	43.36	32.88	52.99	113.25	59.36	100.61	23.91	-23.24	-23.65	48.00	56.65	51.06
Chan 3	68.41	52.99	103.97	183.32	90.87	166.44	72.97	-22.64	-40.39	83.18	41.61	82.15
Chan 4	153.39	113.25	183.32	450.33	237.99	368.58	111.63	-127.59	-114.84	197.89	279.87	181.73
Chan 5	81.38	59.36	90.87	237.99	131.16	194.16	49.96	-55.87	-73.76	133.94	175.23	96.26
Chan 6	134.96	100.61	166.44	368.58	194.16	317.98	89.27	-80.94	-100.82	-38.94	197.47	159.35
Chan 7	26.95	23.91	72.97	111.63	49.96	89.27	100.99	-6.32	-3.64	86.53	-9.89	38.03
Chan 8	-35.27	-23.24	-22.64	-127.59	-55.87	-80.94	-6.32	147.28	18.35	-98.48	-99.42	-40.70
Chan 9	-50.86	-23.65	-40.39	-114.84	-73.76	-100.82	-3.64	18.35	175.02	-628.49	-121.61	-57.50
Chan 10	68.33	48.00	83.18	197.89	133.94	-38.94	86.53	-98.48	-628.49	-49802.87	12916.27	83.12
Chan 11	85.31	56.65	41.61	279.87	175.23	197.47	-9.89	-99.42	-121.61	-12916.27	3095.31	99.50
Chan 12	68.22	51.06	82.15	181.73	96.26	159.35	38.03	-40.70	-57.50	83.12	99.50	81.79

	No.Pixels	Minimum	Mean	Maximum	Std.Dev.
Dolorite 1					
Chan1:	630	57	67.64	80	3.49
Chan2:	630	25	33.95	45	3.07
Chan3:	630	44	57.70	77	6.73
Chan4:	630	57	92.98	128	14.40
Chan5:	630	28	48.27	70	7.96
Chan6:	630	76	101.70	130	10.51
Chan7:	630	77	97.60	130	10.17
Chan8:	630	85	122.51	159	10.43
Chan9:	630	103	151.32	200	16.70
Chan10:	630	170	201.84	230	16.85
Chan11:	630	119	161.82	217	15.07
Chan12:	630	26	40.62	58	5.55

Training set covariance matrix

	Chan 1	Chan 2	Chan 3	Chan 4	Chan 5	Chan 6	Chan 7	Chan 8	Chan 9	Chan 10	Chan 11	Chan 12
Chan 1	12.20	9.84	18.78	41.44	21.32	33.46	17.24	-10.57	-11.82	22.46	16.80	16.90
Chan 2	9.84	9.44	16.90	38.52	19.97	30.57	17.01	-9.09	2.73	19.80	17.15	15.84
Chan 3	18.78	16.90	45.33	78.20	35.98	61.77	59.42	-15.24	-10.49	48.11	1.37	28.95
Chan 4	41.44	38.52	78.20	207.48	109.62	147.02	109.67	-65.00	-50.90	150.46	122.69	74.82
Chan 5	21.32	19.97	35.98	109.62	63.40	77.11	51.29	-20.62	-35.68	80.96	89.34	40.03
Chan 6	33.46	30.57	61.77	147.02	77.11	110.47	76.26	-37.18	-32.00	94.83	72.78	56.38
Chan 7	17.24	17.01	59.42	109.67	51.29	76.26	103.46	-21.47	-25.17	91.33	12.38	33.38
Chan 8	-10.57	-9.09	-15.24	-65.00	-20.62	-37.18	-21.47	108.84	23.69	-57.10	-20.84	-23.06
Chan 9	-11.82	2.73	-10.49	-50.90	-35.68	-32.00	-25.17	23.69	-2013.18	-15602.32	169.64	-23.38
Chan 10	22.46	19.80	48.11	150.46	80.96	94.83	91.33	-57.10	-15602.32	62061.38	34271.40	46.99
Chan 11	16.80	17.15	1.37	122.69	89.34	72.78	12.38	-20.84	-169.64	-34271.40	4148.88	43.63
Chan 12	16.90	15.84	28.95	74.82	40.03	56.38	33.38	-23.06	-23.38	46.99	43.63	30.75

Dolorite 2

Chan1:	325	62	74.13	86	3.91
Chan2:	325	29	39.11	50	3.09
Chan3:	325	50	65.84	80	4.78
Chan4:	325	65	103.26	122	9.72
Chan5:	325	31	51.64	66	5.41
Chan6:	325	83	115.25	140	8.52
Chan7:	325	81	95.23	123	6.22
Chan8:	325	85	111.61	139	9.69
Chan9:	325	93	133.89	174	16.35
Chan10:	325	171	198.13	219	6.64
Chan11:	325	119	154.39	192	12.18
Chan12:	325	32	50.65	65	5.28

Training set covariance matrix

	Chan 1	Chan 2	Chan 3	Chan 4	Chan 5	Chan 6	Chan 7	Chan 8	Chan 9	Chan 10	Chan 11	Chan 12
Chan 1	15.32	11.16	13.80	30.76	15.60	31.11	-5.90	-16.07	-21.27	3.77	13.38	18.78
Chan 2	11.16	9.56	11.56	25.76	12.84	25.39	-2.51	-12.74	-1.99	2.53	10.96	15.48
Chan 3	13.80	11.56	22.88	30.98	12.13	32.52	11.88	-10.71	-1.64	3.08	-11.27	17.66
Chan 4	30.76	25.76	30.98	94.49	49.02	78.13	5.13	-55.78	-28.90	39.53	66.02	46.37
Chan 5	15.60	12.84	12.13	49.02	29.32	39.88	-2.07	-19.84	-25.01	22.31	50.93	24.28
Chan 6	31.11	25.39	32.52	78.13	39.88	72.62	-0.92	-39.08	-28.81	19.50	40.22	43.62
Chan 7	-5.90	-2.51	11.88	5.13	-2.07	-0.92	38.66	6.01	25.99	15.41	-25.95	-5.41
Chan 8	-16.07	-12.74	-10.71	-55.78	-19.84	-39.08	6.01	93.81	20.71	-30.58	-30.85	-26.32
Chan 9	-21.27	-1.99	-1.64	-28.90	-25.01	-28.81	25.99	20.71	267.31	-2257.03	-58.00	-24.78
Chan 10	3.77	2.53	3.08	39.53	22.31	19.50	15.41	-30.58	-2257.03	-64885.04	14108.09	10.26
Chan 11	13.38	10.96	-11.27	66.02	50.93	40.22	-25.95	-30.85	-58.00	-14108.09	1671.98	28.58
Chan 12	18.78	15.48	17.66	46.37	24.28	43.62	-5.41	-26.32	-24.78	10.26	28.58	27.87

Dolorite 3

	No.Pixels	Minimum	Mean	Maximum	Std.Dev.
Chan1:	192	70	76.63	83	2.59
Chan2:	192	36	40.33	47	1.99
Chan3:	192	57	64.73	72	3.64
Chan4:	192	105	117.32	146	7.25
Chan5:	192	52	61.92	79	5.32
Chan6:	192	112	123.07	142	6.11
Chan7:	192	82	94.44	108	4.79
Chan8:	192	82	104.93	125	8.90
Chan9:	192	69	110.52	157	15.25
Chan10:	192	201	210.80	227	4.37
Chan11:	192	146	179.13	202	10.42
Chan12:	192	48	55.67	67	3.87

Training set covariance matrix

	Chan 1	Chan 2	Chan 3	Chan 4	Chan 5	Chan 6	Chan 7	Chan 8	Chan 9	Chan 10	Chan 11	Chan 12
Chan 1	6.73	4.12	7.15	11.88	5.29	12.71	-0.42	-6.86	-18.80	-0.17	-3.55	7.43
Chan 2	4.12	3.96	5.46	11.87	7.15	11.38	1.73	0.40	-3.56	0.29	3.39	6.99
Chan 3	7.15	5.46	13.26	17.31	6.65	17.54	9.52	-6.84	-15.56	1.44	-12.94	9.82
Chan 4	11.88	11.87	17.31	52.60	34.22	41.86	16.77	1.48	-37.20	-324.33	32.83	25.63
Chan 5	5.29	7.15	6.65	34.22	28.25	25.99	9.22	20.02	-23.65	14.01	42.31	16.76
Chan 6	12.71	11.38	17.54	41.86	25.99	37.30	10.60	0.81	-34.52	9.03	16.58	22.88
Chan 7	-0.42	1.73	9.52	16.77	9.22	10.60	22.95	4.62	-3.53	12.32	-1.00	5.12
Chan 8	-6.86	0.40	-6.84	1.48	20.02	0.81	4.62	79.13	21.82	0.41	53.48	1.26
Chan 9	-18.80	-3.56	-15.56	-37.20	-23.65	-34.52	-3.53	21.82	232.62	-28.61	-15.77	-25.68
Chan 10	-0.17	0.29	1.44	-324.33	14.01	9.03	12.32	0.41	-28.61	-65860.02	63453.09	5.46
Chan 11	-3.55	3.39	-12.94	32.83	42.31	16.58	-1.00	53.48	-15.77	-63453.09	25625.51	13.68
Chan 12	7.43	6.99	9.82	25.63	16.76	22.88	5.12	1.26	-25.68	5.46	13.68	14.99

Laterite 1

Chan1:	299	69	82.25	90	3.30
Chan2:	299	37	46.58	55	2.35
Chan3:	299	62	79.18	88	4.03
Chan4:	299	110	124.08	147	6.54
Chan5:	299	44	53.79	72	4.54
Chan6:	299	114	134.65	155	5.43
Chan7:	299	80	99.26	120	8.42
Chan8:	299	45	69.86	104	10.21
Chan9:	299	86	135.94	192	17.84
Chan10:	299	183	199.48	221	7.18
Chan11:	299	109	137.08	172	12.20
Chan12:	299	48	63.70	75	3.98

Training set covariance matrix

	Chan 1	Chan 2	Chan 3	Chan 4	Chan 5	Chan 6	Chan 7	Chan 8	Chan 9	Chan 10	Chan 11	Chan 12
Chan 1	10.91	6.42	5.62	5.25	2.59	13.97	-17.85	-3.28	-22.35	-12.62	-3.27	9.73
Chan 2	6.42	5.54	4.94	6.76	3.60	11.62	-8.99	-1.35	0.70	-8.57	-0.03	8.24
Chan 3	5.62	4.94	16.24	2.05	-1.32	12.11	10.53	16.28	-5.59	-12.00	-28.64	6.69
Chan 4	5.25	6.76	2.05	42.77	27.42	24.80	6.53	-18.00	6.86	25.78	56.93	13.94
Chan 5	2.59	3.60	-1.32	27.42	20.64	14.70	3.38	-1.32	4.08	18.57	47.14	7.62
Chan 6	13.97	11.62	12.11	24.80	14.70	29.51	-10.72	-3.79	-15.22	-6.85	12.99	19.53
Chan 7	-17.85	-8.99	10.53	6.53	3.38	-10.72	70.95	33.95	41.08	31.86	-9.27	-14.31
Chan 8	-3.28	-1.35	16.28	-18.00	-1.32	-3.79	33.95	104.19	36.13	-15.71	-30.27	-11.16
Chan 9	-22.35	0.70	-5.59	6.86	4.08	-15.22	41.08	36.13	-781.20	-5493.29	15.19	-22.70
Chan 10	-12.62	-8.57	-12.00	25.78	18.57	-6.85	31.86	-15.71	-5493.29	-65704.41	4558.12	-8.59
Chan 11	-3.27	-0.03	-28.64	56.93	47.14	12.99	-9.27	-30.27	15.19	-4558.12	148.87	6.31
Chan 12	9.73	8.24	6.69	13.94	7.62	19.53	-14.31	-11.16	-22.70	-8.59	6.31	15.82

Laterite 2

	No.Pixels	Minimum	Mean	Maximum	Std.Dev.
Chan1:	126	73	86.69	95	4.57
Chan2:	126	37	47.96	55	3.70
Chan3:	126	56	74.73	87	6.62
Chan4:	126	103	129.92	148	9.29
Chan5:	126	47	59.12	74	5.62
Chan6:	126	108	137.97	156	9.50
Chan7:	126	69	86.53	104	6.60
Chan8:	126	43	66.25	93	9.83
Chan9:	126	98	137.36	177	16.51
Chan10:	126	186	201.74	216	6.90
Chan11:	126	124	155.87	189	13.98
Chan12:	126	45	63.94	76	6.32

Training set covariance matrix

	Chan 1	Chan 2	Chan 3	Chan 4	Chan 5	Chan 6	Chan 7	Chan 8	Chan 9	Chan 10	Chan 11	Chan 12
Chan 1	20.89	15.84	24.80	30.36	11.02	40.41	-7.22	-20.50	-32.92	-13.34	-19.62	26.62
Chan 2	15.84	13.72	21.20	25.91	9.75	33.91	-3.13	-14.21	-12.84	-11.98	-16.21	22.71
Chan 3	24.80	21.20	43.89	37.98	8.34	54.74	10.59	-27.18	-42.12	-20.69	-56.68	37.15
Chan 4	30.36	25.91	37.98	86.33	44.94	77.29	13.43	-31.44	-29.33	14.53	27.09	45.33
Chan 5	11.02	9.75	8.34	44.94	31.61	32.79	5.04	4.83	-6.55	17.82	49.65	17.16
Chan 6	40.41	33.91	54.74	77.29	32.79	90.27	1.95	-36.51	-52.28	-16.49	-26.01	58.37
Chan 7	-7.22	-3.13	10.59	13.43	5.04	1.95	43.51	4.23	0.42	21.62	-6.38	-1.95
Chan 8	-20.50	-14.21	-27.18	-31.44	4.83	-36.51	4.23	96.60	37.38	7.41	54.51	-26.29
Chan 9	-32.92	-12.84	-42.12	-29.33	-6.55	-52.28	0.42	37.38	272.49	-5236.95	-469.14	-40.59
Chan 10	-13.34	-11.98	-20.69	14.53	17.82	-16.49	21.62	7.41	-5236.95	-66012.78	25094.04	-17.38
Chan 11	-19.62	-16.21	-56.68	27.09	49.65	-26.01	-6.38	54.51	-469.14	-25094.04	2426.07	-27.94
Chan 12	26.62	22.71	37.15	45.33	17.16	58.37	-1.95	-26.29	-40.59	-17.38	-27.94	39.91

Limestone 1

Chan1:	812	67	78.69	91	2.98
Chan2:	812	35	45.53	58	2.38
Chan3:	812	58	78.61	92	3.46
Chan4:	812	118	158.56	184	7.96
Chan5:	812	63	89.44	102	5.66
Chan6:	812	119	149.03	176	6.40
Chan7:	812	105	129.11	146	6.49
Chan8:	812	85	118.03	162	10.31
Chan9:	812	40	101.00	170	19.43
Chan10:	812	212	232.36	245	4.76
Chan11:	812	160	200.81	226	7.35
Chan12:	812	47	68.65	83	4.12

Training set covariance matrix

	Chan 1	Chan 2	Chan 3	Chan 4	Chan 5	Chan 6	Chan 7	Chan 8	Chan 9	Chan 10	Chan 11	Chan 12
Chan 1	8.79	5.74	5.94	10.47	3.54	12.83	-8.57	-9.74	7.20	-6.49	-4.06	6.37
Chan 2	5.74	5.64	6.51	12.83	6.61	13.36	-1.20	-1.91	13.93	-4.54	-0.69	7.53
Chan 3	5.94	6.51	11.99	16.93	9.85	18.16	8.42	8.49	2.51	-3.85	-5.24	10.47
Chan 4	10.47	12.83	16.93	-17.49	41.56	46.73	22.02	-3.78	-35.81	-61965.34	28168.65	29.72
Chan 5	3.54	6.61	9.85	41.56	31.98	29.39	21.29	15.80	-41.74	14.42	30.75	19.61
Chan 6	12.83	13.36	18.16	46.73	29.39	40.99	11.02	2.13	-14.18	-57453.84	713.54	25.10
Chan 7	-8.57	-1.20	8.42	22.02	21.29	11.02	42.06	35.77	-42.19	-4263.86	16.39	8.94
Chan 8	-9.74	-1.91	8.49	-3.78	15.80	2.13	35.77	106.33	-18.01	-1210.39	7.87	1.06
Chan 9	7.20	13.93	2.51	-35.81	-41.74	-14.18	-42.19	-18.01	377.70	-1110.92	-63.01	-23.14
Chan 10	-6.49	-4.54	-3.85	-61965.34	14.42	-57453.84	4263.86	-1210.39	-1110.92	-65594.10	65589.62	3.15
Chan 11	-4.06	-0.69	-5.24	-28168.65	30.75	-713.54	16.39	7.87	-63.01	-65589.62	63784.93	11.67
Chan 12	6.37	7.53	10.47	29.72	19.61	25.10	8.94	1.06	-23.14	3.15	11.67	17.02

Limestone 12

	No.Pixels	Minimum	Mean	Maximum	Std.Dev.
Chan1:	576	72	79.51	88	3.52
Chan2:	576	36	44.18	52	3.10
Chan3:	576	61	75.41	86	4.53
Chan4:	576	103	137.52	171	13.30
Chan5:	576	54	73.92	96	8.66
Chan6:	576	112	136.91	161	9.80
Chan7:	576	91	114.93	129	6.18
Chan8:	576	91	118.86	148	9.31
Chan9:	576	98	138.59	184	15.86
Chan10:	576	191	218.87	234	6.29
Chan11:	576	148	181.77	206	12.01
Chan12:	576	44	58.82	73	5.65

Training set covariance matrix

	Chan 1	Chan 2	Chan 3	Chan 4	Chan 5	Chan 6	Chan 7	Chan 8	Chan 9	Chan 10	Chan 11	Chan 12
Chan 1	12.41	9.84	11.96	37.11	22.91	31.20	2.91	-4.39	-18.13	5.73	18.70	17.52
Chan 2	9.84	9.63	11.20	35.61	22.13	29.19	5.33	-2.58	-1.51	5.03	18.72	16.82
Chan 3	11.96	11.20	20.51	39.19	22.23	35.34	16.51	2.66	-13.23	4.27	3.85	19.87
Chan 4	37.11	35.61	39.19	176.84	111.92	124.17	41.77	-26.26	-21.14	-14985.65	1927.78	66.71
Chan 5	22.91	22.13	22.23	111.92	75.03	78.45	24.57	-2.52	-20.27	38.34	89.37	42.23
Chan 6	31.20	29.19	35.34	124.17	78.45	96.04	25.84	-8.96	-27.91	-9316.15	-40.27	53.72
Chan 7	2.91	5.33	16.51	41.77	24.57	25.84	38.14	5.58	2.70	23.37	14.85	11.14
Chan 8	-4.39	-2.58	2.66	-26.26	-2.52	-8.96	5.58	86.73	-12.28	-16.48	-9.39	-5.81
Chan 9	-18.13	-1.51	-13.23	-21.14	-20.27	-27.91	2.70	-12.28	137.48	-15971.02	810.07	-21.83
Chan 10	5.73	5.03	4.27	-14985.65	38.34	-9316.15	23.37	-16.48	-15971.02	65610.43	63768.21	12.80
Chan 11	18.70	18.72	3.85	-1927.78	89.37	-40.27	14.85	-9.39	-810.07	-63768.21	33022.66	38.30
Chan 12	17.52	16.82	19.87	66.71	42.23	53.72	11.14	-5.81	-21.83	12.80	38.30	31.90

Limestone 13

	No.Pixels	Minimum	Mean	Maximum	Std.Dev.
Chan1:	621	69	79.71	90	3.83
Chan2:	621	37	46.37	57	3.65
Chan3:	621	72	83.25	96	3.99
Chan4:	621	111	147.73	176	12.56
Chan5:	621	56	79.84	99	7.97
Chan6:	621	119	145.77	173	10.17
Chan7:	621	115	128.96	143	4.97
Chan8:	621	94	124.75	164	11.52
Chan9:	621	81	131.80	189	18.13
Chan10:	621	207	221.89	235	5.03
Chan11:	621	141	179.13	200	9.91
Chan12:	621	47	64.71	82	6.45

Training set covariance matrix

	Chan 1	Chan 2	Chan 3	Chan 4	Chan 5	Chan 6	Chan 7	Chan 8	Chan 9	Chan 10	Chan 11	Chan 12
Chan 1	14.67	12.69	12.13	39.47	23.03	35.38	-5.34	-13.96	-7.34	-0.17	18.90	21.65
Chan 2	12.69	13.36	12.51	40.22	24.51	35.81	-2.00	-7.28	10.28	-1.28	20.52	22.36
Chan 3	12.13	12.51	15.90	37.55	21.55	35.05	3.94	-6.80	-5.29	-1.35	10.40	22.43
Chan 4	39.47	40.22	37.55	157.74	95.94	122.50	10.96	-49.66	-13.25	-37392.58	958.74	74.96
Chan 5	23.03	24.51	21.55	95.94	63.55	75.23	7.24	-8.11	-9.66	15.92	69.92	45.99
Chan 6	35.38	35.81	35.05	122.50	75.23	103.41	2.30	-27.09	-8.32	-31173.78	354.51	64.46
Chan 7	-5.34	-2.00	3.94	10.96	7.24	2.30	24.73	4.28	-13.11	-197.32	5.24	1.38
Chan 8	-13.96	-7.28	-6.80	-49.66	-8.11	-27.09	4.28	132.66	31.29	-973.55	-4.87	-17.43
Chan 9	-7.34	10.28	-5.29	-13.25	-9.66	-8.32	-13.11	31.29	117.29	-10501.98	221.19	-13.89
Chan 10	-0.17	-1.28	-1.35	-37392.58	15.92	-31173.78	197.32	-973.55	-10501.98	65616.45	64344.85	4.18
Chan 11	18.90	20.52	10.40	-958.74	69.92	-354.51	5.24	-4.87	-221.19	-64344.85	31295.65	40.34
Chan 12	21.65	22.36	22.43	74.96	45.99	64.46	1.38	-17.43	-13.89	4.18	40.34	41.67

No.Pixels Minimum Mean Maximum Std.Dev.

Limestone 14

	No.Pixels	Minimum	Mean	Maximum	Std.Dev.
Chan1:	728	64	71.31	81	2.59
Chan2:	728	30	36.04	43	2.36
Chan3:	728	44	56.26	65	5.80
Chan4:	728	92	108.07	132	6.54
Chan5:	728	44	59.72	73	4.49
Chan6:	728	94	111.20	132	6.81
Chan7:	728	77	93.39	131	6.54
Chan8:	728	99	116.21	148	7.23
Chan9:	728	71	127.94	174	17.37
Chan10:	728	197	214.67	228	4.92
Chan11:	728	124	192.59	214	13.82
Chan12:	728	35	46.89	60	4.89

Training set covariance matrix

	Chan 1	Chan 2	Chan 3	Chan 4	Chan 5	Chan 6	Chan 7	Chan 8	Chan 9	Chan 10	Chan 11	Chan 12
Chan 1	6.71	5.20	10.10	11.72	5.92	15.22	2.05	0.43	-23.06	-4.34	-9.67	10.18
Chan 2	5.20	5.56	10.78	12.36	6.34	15.42	5.30	2.57	-11.37	-4.84	-10.29	10.66
Chan 3	10.10	10.78	33.64	20.29	5.06	31.41	29.21	9.83	-29.19	-13.63	-61.59	20.44
Chan 4	11.72	12.36	20.29	42.77	25.58	39.61	13.83	-2.36	-39.52	6.64	8.32	26.73
Chan 5	5.92	6.34	5.06	25.58	20.13	21.63	0.45	5.92	-32.51	7.46	29.46	15.65
Chan 6	15.22	15.42	31.41	39.61	21.63	46.38	18.44	7.55	-54.64	-7.42	-23.68	32.12
Chan 7	2.05	5.30	29.21	13.83	0.45	18.44	42.72	11.09	-2.28	-2.42	-61.08	10.05
Chan 8	0.43	2.57	9.83	-2.36	5.92	7.55	11.09	52.29	-17.01	-11.78	-10.22	5.47
Chan 9	-23.06	-11.37	-29.19	-39.52	-32.51	-54.64	-2.28	-17.01	301.62	-4512.98	-902.48	-48.23
Chan 10	-4.34	-4.84	-13.63	6.64	7.46	-7.42	-2.42	-11.78	-4512.98	-65601.96	62787.01	-5.90
Chan 11	-9.67	-10.29	-61.59	8.32	29.46	-23.68	-61.08	-10.22	-902.48	-62787.01	56600.84	-12.47
Chan 12	10.18	10.66	20.44	26.73	15.65	32.12	10.05	5.47	-48.23	-5.90	-12.47	23.91

Limestone 15

Chan1:	648	74	91.40	118	8.36
Chan2:	648	37	51.41	72	6.45
Chan3:	648	64	83.71	103	6.48
Chan4:	648	115	153.56	195	15.02
Chan5:	648	55	82.12	106	9.44
Chan6:	648	119	155.57	204	16.02
Chan7:	648	67	105.93	140	9.41
Chan8:	648	77	114.03	154	10.59
Chan9:	648	60	130.74	191	18.55
Chan10:	648	191	214.43	232	6.18
Chan11:	648	132	182.02	203	9.24
Chan12:	648	47	68.22	97	9.59

Training set covariance matrix

	Chan 1	Chan 2	Chan 3	Chan 4	Chan 5	Chan 6	Chan 7	Chan 8	Chan 9	Chan 10	Chan 11	Chan 12
Chan 1	69.93	52.81	48.97	115.19	70.93	131.45	-62.02	-5.19	-25.89	-33.01	35.25	77.83
Chan 2	52.81	41.58	38.21	89.49	54.99	101.92	-46.38	-2.68	-2.52	-26.95	26.98	60.69
Chan 3	48.97	38.21	42.01	83.97	48.84	95.87	-30.71	-1.82	-7.32	-23.41	10.91	55.70
Chan 4	115.19	89.49	83.97	-2002.88	137.26	-3211.63	-80.98	-28.59	-34.27	-33559.90	6397.54	135.55
Chan 5	70.93	54.99	48.84	137.26	89.17	143.25	-54.54	2.51	-33.56	-20.77	64.19	84.17
Chan 6	131.45	101.92	95.87	-3211.63	143.25	-4402.72	-106.17	-10.28	-139.41	-36217.20	9546.88	151.97
Chan 7	-62.02	-46.38	-30.71	-80.98	-54.54	-106.17	88.56	0.29	22.57	44.82	-38.76	-67.42
Chan 8	-5.19	-2.68	-1.82	-28.59	2.51	-10.28	0.29	112.23	-1.78	-15.82	5.55	-7.56
Chan 9	-25.89	-2.52	-7.32	-34.27	-33.56	-139.41	22.57	-1.78	141.42	-6908.68	-142.24	-31.59
Chan 10	-33.01	-26.95	-23.41	-33559.90	-20.77	-36217.20	44.82	-15.82	-6908.68	-65599.10	64823.13	-35.50
Chan 11	35.25	26.98	10.91	-6397.54	64.19	-9546.88	-38.76	5.55	-142.24	-64823.13	40735.29	45.71
Chan 12	77.83	60.69	55.70	135.55	84.17	151.97	-67.42	-7.56	-31.59	-35.50	45.71	92.03

Limestone 16

Chan1:	480	68	75.72	88	3.39
Chan2:	480	33	39.69	51	2.90
Chan3:	480	63	75.14	92	4.13
Chan4:	480	90	124.54	157	8.31
Chan5:	480	42	57.55	82	6.35
Chan6:	480	100	124.95	155	7.60
Chan7:	480	96	118.67	149	8.00
Chan8:	480	60	85.97	124	10.47
Chan9:	480	81	127.14	179	15.49
Chan10:	480	203	220.26	237	4.86
Chan11:	480	98	151.35	188	13.65
Chan12:	480	38	53.10	70	4.99

Training set covariance matrix

	Chan 1	Chan 2	Chan 3	Chan 4	Chan 5	Chan 6	Chan 7	Chan 8	Chan 9	Chan 10	Chan 11	Chan 12
Chan 1	11.48	9.02	6.36	21.78	15.51	23.57	-12.53	1.15	-16.04	-5.92	21.72	15.36
Chan 2	9.02	8.39	5.42	20.06	14.46	20.91	-9.70	2.77	-0.38	-5.74	21.21	13.68
Chan 3	6.36	5.42	17.07	16.13	5.48	17.81	16.94	0.32	-13.28	-0.40	-16.91	9.51
Chan 4	21.78	20.06	16.13	69.14	48.09	59.25	-6.14	2.45	-22.27	-814.32	74.14	36.41
Chan 5	15.51	14.46	5.48	48.09	40.29	41.54	-13.66	22.86	-11.83	2.92	75.19	25.34
Chan 6	23.57	20.91	17.81	59.25	41.54	57.70	-13.61	7.50	-24.04	-552.63	57.28	36.46
Chan 7	-12.53	-9.70	16.94	-6.14	-13.66	-13.61	64.03	4.30	-0.80	-113.47	-56.32	-14.79
Chan 8	1.15	2.77	0.32	2.45	22.86	7.50	4.30	109.53	30.74	-6.20	46.02	-2.23
Chan 9	-16.04	-0.38	-13.28	-22.27	-11.83	-24.04	-0.80	30.74	240.02	-4809.70	-2.55	-20.92
Chan 10	-5.92	-5.74	-0.40	-814.32	2.92	-552.63	-113.47	-6.20	-4809.70	-65649.20	35839.08	-5.77
Chan 11	21.72	21.21	-16.91	74.14	75.19	57.28	-56.32	46.02	-2.55	-35839.08	771.54	37.29
Chan 12	15.36	13.68	9.51	36.41	25.34	36.46	-14.79	-2.23	-20.92	-5.77	37.29	24.87

	No.Pixels	Minimum	Mean	Maximum	Std.Dev.
Limestone 41					
Chan1:	812	74	87.19	118	6.55
Chan2:	812	38	50.11	75	5.49
Chan3:	812	53	71.36	102	6.82
Chan4:	812	104	139.45	198	14.13
Chan5:	812	53	74.47	109	8.50
Chan6:	812	113	143.73	205	14.15
Chan7:	812	56	85.76	120	7.33
Chan8:	812	78	104.37	134	8.41
Chan9:	812	125	166.83	209	15.77
Chan10:	812	185	205.28	220	5.45
Chan11:	812	154	189.98	219	7.94
Chan12:	812	45	64.14	99	8.11

Training set covariance matrix

	Chan 1	Chan 2	Chan 3	Chan 4	Chan 5	Chan 6	Chan 7	Chan 8	Chan 9	Chan 10	Chan 11	Chan 12
Chan 1	42.92	34.91	39.37	82.97	50.63	89.85	-18.99	9.23	1.21	-11.29	16.19	51.21
Chan 2	34.91	30.18	34.14	71.33	42.83	76.46	-13.00	7.02	17.75	-10.39	12.09	43.88
Chan 3	39.37	34.14	46.51	86.70	49.14	90.68	1.57	5.62	7.81	-6.56	0.59	51.26
Chan 4	82.97	71.33	86.70	-1012.59	117.02	-1342.11	-4.17	-3.68	-462.05	-5976.21	-2782.39	107.78
Chan 5	50.63	42.83	49.14	117.02	72.29	115.35	-9.45	10.54	8.48	-0.12	36.26	64.33
Chan 6	89.85	76.46	90.68	-1342.11	115.35	-1739.13	-21.33	13.17	-1271.78	-7045.16	-3520.32	113.68
Chan 7	-18.99	-13.00	1.57	-4.17	-9.45	-21.33	53.75	-16.07	-3.95	27.79	-18.86	-15.31
Chan 8	9.23	7.02	5.62	-3.68	10.54	13.17	-16.07	70.74	-2.31	-20.26	6.67	6.70
Chan 9	1.21	17.75	7.81	-462.05	8.48	-1271.78	-3.95	-2.31	-11872.64	43823.18	24244.25	10.21
Chan 10	-11.29	-10.39	-6.56	-5976.21	-0.12	-7045.16	27.79	-20.26	-43823.18	65587.13	64715.24	-11.46
Chan 11	16.19	12.09	0.59	-2782.39	36.26	-3520.32	-18.86	6.67	-24244.25	64715.24	58685.06	18.45
Chan 12	51.21	43.88	51.26	107.78	64.33	113.68	-15.31	6.70	10.21	-11.46	18.45	65.72

	No.Pixels	Minimum	Mean	Maximum	Std.Dev.
Limestone 42					
Chan1:	1311	71	92.46	118	6.55
Chan2:	1311	35	54.45	76	6.26
Chan3:	1311	48	81.49	102	7.43
Chan4:	1311	120	164.75	201	13.87
Chan5:	1311	54	86.80	110	9.54
Chan6:	1311	110	161.09	208	14.74
Chan7:	1311	70	100.62	159	10.74
Chan8:	1311	61	93.79	133	10.91
Chan9:	1311	99	161.86	227	20.33
Chan10:	1311	194	216.03	235	6.06
Chan11:	1311	109	192.52	230	14.02
Chan12:	1311	41	72.10	100	9.35

Training set covariance matrix

	Chan 1	Chan 2	Chan 3	Chan 4	Chan 5	Chan 6	Chan 7	Chan 8	Chan 9	Chan 10	Chan 11	Chan 12
Chan 1	42.96	39.28	32.34	83.51	55.01	93.43	-39.43	10.66	33.00	-26.27	29.00	58.03
Chan 2	39.28	39.22	33.76	80.17	51.73	90.86	-33.17	12.03	56.90	-28.72	21.89	57.45
Chan 3	32.34	33.76	55.19	65.59	31.55	81.83	15.38	17.10	48.99	-28.16	-43.65	48.62
Chan 4	83.51	80.17	65.59	-6511.20	125.48	-5806.36	-62.16	9.37	-6921.01	-56368.86	28686.53	121.39
Chan 5	55.01	51.73	31.55	125.48	91.05	127.15	-57.94	25.08	39.87	-23.40	83.39	79.22
Chan 6	93.43	90.86	81.83	-5806.36	127.15	-5085.65	-68.35	27.93	-5853.99	-52787.64	22607.10	135.70
Chan 7	-39.43	-33.17	15.38	-62.16	-57.94	-68.35	115.33	2.18	-22.18	-373.57	-112.68	-49.80
Chan 8	10.66	12.03	17.10	9.37	25.08	27.93	2.18	119.06	14.80	-20.87	6.38	13.64
Chan 9	33.00	56.90	48.99	-6921.01	39.87	-5853.99	-22.18	14.80	-10592.67	45789.15	22983.79	57.72
Chan 10	-26.27	-28.72	-28.16	-56368.86	-23.40	-52787.64	373.57	-20.87	-45789.15	65549.35	64274.32	-39.45
Chan 11	29.00	21.89	-43.65	-28686.53	83.39	-22607.10	112.68	6.38	-22983.79	64274.32	56284.49	38.81
Chan 12	58.03	57.45	48.62	121.39	79.22	135.70	-49.80	13.64	57.72	-39.45	38.81	87.51

Limestone 51

	No.Pixels	Minimum	Mean	Maximum	Std.Dev.
Chan1:	1147	70	78.93	91	2.75
Chan2:	1147	38	43.03	53	2.09
Chan3:	1147	67	74.35	87	3.00
Chan4:	1147	115	136.25	161	6.37
Chan5:	1147	60	73.17	85	3.99
Chan6:	1147	119	135.56	161	5.65
Chan7:	1147	103	114.41	126	3.67
Chan8:	1147	90	114.65	136	7.10
Chan9:	1147	67	118.49	184	14.27
Chan10:	1147	212	221.20	231	2.92
Chan11:	1147	160	182.79	201	6.38
Chan12:	1147	49	59.31	73	3.47

Training set covariance matrix

	Chan 1	Chan 2	Chan 3	Chan 4	Chan 5	Chan 6	Chan 7	Chan 8	Chan 9	Chan 10	Chan 11	Chan 12
Chan 1	7.57	4.96	6.27	13.49	6.88	13.75	-3.24	-5.38	-7.73	-1.88	1.22	7.40
Chan 2	4.96	4.36	4.95	11.54	6.25	11.24	-1.18	-2.74	3.97	-1.90	2.34	6.42
Chan 3	6.27	4.95	9.01	12.73	5.40	13.46	3.24	-2.37	2.59	-2.49	-5.94	6.78
Chan 4	13.49	11.54	12.73	40.60	23.21	34.31	0.40	-14.79	-10.78	-4056.56	18.09	20.34
Chan 5	6.88	6.25	5.40	23.21	15.95	19.35	-0.72	-0.42	-12.04	3.08	18.00	12.06
Chan 6	13.75	11.24	13.46	34.31	19.35	31.95	-1.41	-8.94	-9.15	-1888.12	10.33	18.60
Chan 7	-3.24	-1.18	3.24	0.40	-0.72	-1.41	13.49	4.79	9.45	3.66	-6.81	-1.82
Chan 8	-5.38	-2.74	-2.37	-14.79	-0.42	-8.94	4.79	50.46	14.67	-5.22	3.07	-6.70
Chan 9	-7.73	3.97	2.59	-10.78	-12.04	-9.15	9.45	14.67	146.47	-992.37	-81.85	-12.11
Chan 10	-1.88	-1.90	-2.49	-4056.56	3.08	-1888.12	3.66	-5.22	-992.37	-65584.64	65583.84	0.11
Chan 11	1.22	2.34	-5.94	18.09	18.00	10.33	-6.81	3.07	-81.85	-65583.84	36787.61	9.14
Chan 12	7.40	6.42	6.78	20.34	12.06	18.60	-1.82	-6.70	-12.11	0.11	9.14	12.05

Limestone 52

	No.Pixels	Minimum	Mean	Maximum	Std.Dev.
Chan1:	1247	73	86.35	123	7.47
Chan2:	1247	36	48.18	72	5.56
Chan3:	1247	49	80.64	107	8.26
Chan4:	1247	100	138.83	194	15.86
Chan5:	1247	52	69.68	109	10.24
Chan6:	1247	106	144.32	207	15.39
Chan7:	1247	70	104.12	135	8.89
Chan8:	1247	69	99.04	141	10.16
Chan9:	1247	80	128.26	181	16.14
Chan10:	1247	196	209.60	228	5.14
Chan11:	1247	126	166.12	207	12.54
Chan12:	1247	44	64.83	99	7.74

Training set covariance matrix

	Chan 1	Chan 2	Chan 3	Chan 4	Chan 5	Chan 6	Chan 7	Chan 8	Chan 9	Chan 10	Chan 11	Chan 12
Chan 1	55.79	40.31	51.06	109.44	69.76	111.67	-9.70	35.11	-8.16	-3.77	39.88	54.69
Chan 2	40.31	30.92	39.30	82.49	52.00	84.14	-4.42	26.18	8.40	-4.33	27.71	41.99
Chan 3	51.06	39.30	68.27	111.56	62.23	113.35	28.42	29.36	-4.54	0.50	-1.33	54.90
Chan 4	109.44	82.49	111.56	-695.17	157.04	-1234.43	15.14	61.56	-4.47	-10344.95	1006.98	115.52
Chan 5	69.76	52.00	62.23	157.04	104.86	148.95	-4.66	55.34	-4.08	9.16	85.18	72.14
Chan 6	111.67	84.14	113.35	-1234.43	148.95	-1709.30	3.52	70.12	-4.83	-13464.20	1919.79	116.66
Chan 7	-9.70	-4.42	28.42	15.14	-4.66	3.52	79.01	-9.55	-5.36	24.49	-52.81	-2.73
Chan 8	35.11	26.18	29.36	61.56	55.34	70.12	-9.55	103.15	18.40	-11.07	50.16	30.08
Chan 9	-8.16	8.40	-4.54	-4.47	-4.08	-4.83	-5.36	18.40	260.52	-2287.93	-51.53	-7.87
Chan 10	-3.77	-4.33	0.50	-10344.95	9.16	-13464.20	24.49	-11.07	-2287.93	-65562.23	48424.66	-2.79
Chan 11	39.88	27.71	-1.33	-1006.98	85.18	-1919.79	-52.81	50.16	-51.53	-48424.66	8364.77	37.82
Chan 12	54.69	41.99	54.90	115.52	72.14	116.66	-2.73	30.08	-7.87	-2.79	37.82	59.93

Limestone 53

Chan1:	1085	70	89.45	113	6.29
Chan2:	1085	35	49.91	68	4.59
Chan3:	1085	73	83.07	99	4.48
Chan4:	1085	98	145.74	180	10.79
Chan5:	1085	41	74.93	98	7.55
Chan6:	1085	111	149.49	191	11.00
Chan7:	1085	53	106.16	151	11.04
Chan8:	1085	76	108.38	141	10.12
Chan9:	1085	95	142.31	234	16.30
Chan10:	1085	171	211.46	228	6.12
Chan11:	1085	94	171.58	202	12.41
Chan12:	1085	39	64.48	88	6.71

Training set covariance matrix

	Chan 1	Chan 2	Chan 3	Chan 4	Chan 5	Chan 6	Chan 7	Chan 8	Chan 9	Chan 10	Chan 11	Chan 12
Chan 1	39.53	27.69	16.32	56.04	38.66	66.37	-54.71	-1.27	-21.38	-20.98	41.33	39.80
Chan 2	27.69	21.04	12.76	41.66	28.34	49.13	-37.76	-0.17	0.28	-16.71	29.05	29.88
Chan 3	16.32	12.76	20.06	24.98	11.69	31.99	-1.67	1.69	0.25	-10.25	-11.02	17.65
Chan 4	56.04	41.66	24.98	116.41	76.86	49.55	-57.89	-20.86	-81.72	-12398.47	390.59	63.57
Chan 5	38.66	28.34	11.69	76.86	56.98	74.16	-49.30	4.35	-21.48	-5.24	79.40	43.25
Chan 6	66.37	49.13	31.99	49.55	74.16	-120.75	-80.00	-4.18	-143.68	-18165.62	828.96	72.13
Chan 7	-54.71	-37.76	-1.67	-57.89	-49.30	-80.00	121.81	0.39	27.23	-16.14	-82.97	-53.65
Chan 8	-1.27	-0.17	1.69	-20.86	4.35	-4.18	0.39	102.40	10.28	-17.31	3.56	-5.71
Chan 9	-21.38	0.28	0.25	-81.72	-21.48	-143.68	27.23	10.28	-641.21	-13198.57	279.52	-18.35
Chan 10	-20.98	-16.71	-10.25	-12398.47	-5.24	-18165.62	-16.14	-17.31	-13198.57	65256.74	60088.49	-20.03
Chan 11	41.33	29.05	-11.02	-390.59	79.40	-828.96	-82.97	3.56	-279.52	-60088.49	11756.24	47.16
Chan 12	39.80	29.88	17.65	63.57	43.25	72.13	-53.65	-5.71	-18.35	-20.03	47.16	44.98

	No.Pixels	Minimum	Mean	Maximum	Std.Dev.
Sandstone 3					
Chan1:	972	64	82.14	103	7.18
Chan2:	972	31	46.80	66	6.65
Chan3:	972	42	74.55	101	11.05
Chan4:	972	74	147.38	198	24.36
Chan5:	972	40	79.15	107	14.26
Chan6:	972	88	143.58	192	20.58
Chan7:	972	70	109.07	133	10.88
Chan8:	972	67	104.92	151	11.59
Chan9:	972	82	140.88	202	17.75
Chan10:	972	185	220.00	240	6.39
Chan11:	972	142	191.56	227	10.67
Chan12:	972	37	63.82	91	11.31

Training set covariance matrix

	Chan 1	Chan 2	Chan 3	Chan 4	Chan 5	Chan 6	Chan 7	Chan 8	Chan 9	Chan 10	Chan 11	Chan 12
Chan 1	51.53	46.51	74.81	165.29	94.09	143.76	51.65	-4.15	-18.42	20.74	27.85	77.47
Chan 2	46.51	44.17	69.67	156.34	90.04	135.34	50.20	-0.49	-5.08	19.19	29.95	73.87
Chan 3	74.81	69.67	122.19	252.24	142.87	219.10	101.72	9.84	-23.65	35.69	26.07	116.51
Chan 4	165.29	156.34	252.24	-1768.84	341.98	-1192.36	209.79	-16.84	-237.90	-40055.36	14173.06	265.41
Chan 5	94.09	90.04	142.87	341.98	203.27	286.28	119.17	11.98	-34.19	59.52	92.43	154.95
Chan 6	143.76	135.34	219.10	-1192.36	286.28	-521.52	170.60	1.92	-179.60	-35901.10	6043.01	229.45
Chan 7	51.65	50.20	101.72	209.79	119.17	170.60	118.38	20.75	-12.29	51.07	21.03	85.25
Chan 8	-4.15	-0.49	9.84	-16.84	11.98	1.92	20.75	134.22	-34.50	-12.51	-1.16	0.35
Chan 9	-18.42	-5.08	-23.65	-237.90	-34.19	-179.60	-12.29	-34.50	-494.68	-19993.71	3859.58	-38.04
Chan 10	20.74	19.19	35.69	-40055.36	59.52	-35901.10	51.07	-12.51	-19993.71	65562.68	64687.09	35.33
Chan 11	27.85	29.95	26.07	-14173.06	92.43	-6043.01	21.03	-1.16	-3859.58	-64687.09	57052.99	57.10
Chan 12	77.47	73.87	116.51	265.41	154.95	229.45	85.25	0.35	-38.04	35.33	57.10	127.83

Sandstone 1

	No.Pixels	Minimum	Mean	Maximum	Std.Dev.
Chan1:	840	61	84.24	119	7.62
Chan2:	840	28	47.56	70	6.43
Chan3:	840	49	79.00	102	9.76
Chan4:	840	65	130.77	172	20.85
Chan5:	840	32	73.51	100	13.23
Chan6:	840	87	143.53	196	18.67
Chan7:	840	54	101.07	155	14.57
Chan8:	840	73	134.79	184	13.60
Chan9:	840	14	90.89	170	22.92
Chan10:	840	167	202.97	229	10.31
Chan11:	840	84	174.71	206	14.06
Chan12:	840	28	68.33	100	11.14

Training set covariance matrix

	Chan 1	Chan 2	Chan 3	Chan 4	Chan 5	Chan 6	Chan 7	Chan 8	Chan 9	Chan 10	Chan 11	Chan 12
Chan 1	58.01	46.04	58.69	121.39	75.73	127.37	-9.98	20.16	-50.91	0.44	43.94	73.21
Chan 2	46.04	41.37	53.75	117.21	74.51	116.49	6.54	23.34	-29.42	7.81	48.27	68.78
Chan 3	58.69	53.75	95.70	182.34	108.94	167.65	73.09	43.21	-43.93	40.10	39.90	90.47
Chan 4	121.39	117.21	182.34	434.58	267.56	372.28	142.27	45.66	-104.77	-7140.32	188.55	209.17
Chan 5	75.73	74.51	108.94	267.56	174.94	235.05	75.63	60.30	-97.69	69.90	139.71	137.09
Chan 6	127.37	116.49	167.65	372.28	235.05	-42.01	73.52	70.60	-123.05	-15558.25	1251.82	201.76
Chan 7	-9.98	6.54	73.09	142.27	75.63	73.52	212.28	29.66	17.29	45.16	10.04	23.38
Chan 8	20.16	23.34	43.21	45.66	60.30	70.60	29.66	34.16	-80.73	-1735.92	-46.34	43.64
Chan 9	-50.91	-29.42	-43.93	-104.77	-97.69	-123.05	17.29	-80.73	525.12	-263.49	-111.90	-99.02
Chan 10	0.44	7.81	40.10	-7140.32	69.90	-15558.25	45.16	-1735.92	-263.49	-62852.07	50554.12	26.94
Chan 11	43.94	48.27	39.90	188.55	139.71	-1251.82	10.04	-46.34	-111.90	-50554.12	21829.79	102.39
Chan 12	73.21	68.78	90.47	209.17	137.09	201.76	23.38	43.64	-99.02	26.94	102.39	124.18

Sadstone 2

	No.Pixels	Minimum	Mean	Maximum	Std.Dev.
Chan1:	432	57	75.86	103	7.55
Chan2:	432	24	40.18	60	6.28
Chan3:	432	29	59.34	82	9.10
Chan4:	432	57	115.79	154	17.60
Chan5:	432	24	60.19	86	10.61
Chan6:	432	67	119.49	167	17.05
Chan7:	432	45	86.34	110	10.66
Chan8:	432	58	94.38	140	12.82
Chan9:	432	83	135.41	177	16.53
Chan10:	432	167	209.47	231	10.11
Chan11:	432	148	186.07	218	11.60
Chan12:	432	25	53.28	85	9.90

Training set covariance matrix

	Chan 1	Chan 2	Chan 3	Chan 4	Chan 5	Chan 6	Chan 7	Chan 8	Chan 9	Chan 10	Chan 11	Chan 12
Chan 1	57.04	46.13	61.22	109.10	66.58	123.14	-11.52	24.85	-40.90	-18.32	14.42	71.94
Chan 2	46.13	39.38	51.89	94.57	57.69	104.41	-5.46	21.59	-17.31	-14.08	15.32	61.27
Chan 3	61.22	51.89	82.80	139.05	83.42	146.70	26.36	46.12	-34.37	-2.85	5.37	81.09
Chan 4	109.10	94.57	139.05	309.90	183.29	281.74	62.66	15.14	-46.18	-97.26	101.61	153.80
Chan 5	66.58	57.69	83.42	183.29	112.68	170.75	33.26	28.88	-37.01	27.17	66.56	94.04
Chan 6	123.14	104.41	146.70	281.74	170.75	290.75	18.14	54.29	-66.77	-156.18	58.97	165.65
Chan 7	-11.52	-5.46	26.36	62.66	33.26	18.14	113.69	14.46	17.53	83.58	15.35	-5.20
Chan 8	24.85	21.59	46.12	15.14	28.88	54.29	14.46	164.28	-34.83	-46.86	-36.00	28.67
Chan 9	-40.90	-17.31	-34.37	-46.18	-37.01	-66.77	17.53	-34.83	273.36	-7753.34	-764.21	-43.72
Chan 10	-18.32	-14.08	-2.85	-97.26	27.17	-156.18	83.58	-46.86	-7753.34	-64369.40	61821.53	-14.82
Chan 11	14.42	15.32	5.37	101.61	66.56	58.97	15.35	-36.00	-764.21	-61821.53	43809.46	32.20
Chan 12	71.94	61.27	81.09	153.80	94.04	165.65	-5.20	28.67	-43.72	-14.82	32.20	97.93

Sandstone 4

Chan1:	870	64	79.98	93	4.38
Chan2:	870	29	43.03	53	3.81
Chan3:	870	48	78.21	90	6.46
Chan4:	870	70	130.54	167	16.81
Chan5:	870	29	65.87	89	9.56
Chan6:	870	85	132.97	162	12.37
Chan7:	870	69	117.13	143	10.19
Chan8:	870	78	112.90	183	12.64
Chan9:	870	91	140.82	199	15.34
Chan10:	870	170	215.25	231	9.52
Chan11:	870	82	162.51	194	13.41
Chan12:	870	32	55.05	75	6.73

Training set covariance matrix

	Chan 1	Chan 2	Chan 3	Chan 4	Chan 5	Chan 6	Chan 7	Chan 8	Chan 9	Chan 10	Chan 11	Chan 12
Chan 1	19.17	15.63	21.13	63.31	36.36	50.69	11.58	-15.65	-17.59	20.24	40.62	27.20
Chan 2	15.63	14.51	19.46	56.63	32.67	45.40	12.80	-11.05	-1.66	16.53	35.45	24.85
Chan 3	21.13	19.46	41.71	86.90	46.97	68.39	50.92	-1.93	-6.28	35.84	31.12	32.84
Chan 4	63.31	56.63	86.90	282.64	156.67	200.85	99.97	-92.03	-26.54	-6733.10	182.25	102.02
Chan 5	36.36	32.67	46.97	156.67	91.30	114.11	49.48	-35.04	-23.29	68.42	111.71	59.25
Chan 6	50.69	45.40	68.39	200.85	114.11	153.01	63.60	-44.62	-27.31	-3316.40	124.31	80.33
Chan 7	11.58	12.80	50.92	99.97	49.48	63.60	103.81	-2.67	11.22	71.67	24.13	22.24
Chan 8	-15.65	-11.05	-1.93	-92.03	-35.04	-44.62	-2.67	84.23	5.29	-132.63	-65.91	-25.25
Chan 9	-17.59	-1.66	-6.28	-26.54	-23.29	-27.31	11.22	5.29	9.15	-15481.40	111.59	-21.87
Chan 10	20.24	16.53	35.84	-6733.10	68.42	-3316.40	71.67	-132.63	-15481.40	64917.50	51120.23	32.97
Chan 11	40.62	35.45	31.12	182.25	111.71	124.31	24.13	-65.91	-111.59	-51120.2[illegible]	[illegible]2685.87	67.63
Chan 12	27.20	24.85	32.84	102.02	59.25	80.33	22.24	-25.25	-21.87	32.97	67.63	45.25

	No.Pixels	Minimum	Mean	Maximum	Std.Dev.
Shadow					
Chan1:	27	60	63.33	66	1.39
Chan2:	27	25	29.11	31	1.70
Chan3:	27	37	50.19	55	3.72
Chan4:	27	51	63.52	71	5.04
Chan5:	27	21	29.07	33	2.87
Chan6:	27	73	82.63	88	3.99
Chan7:	27	69	82.89	92	5.29
Chan8:	27	104	119.18	135	8.01
Chan9:	27	109	147.59	189	20.45
Chan10:	27	151	172.00	186	8.10
Chan11:	27	97	118.22	163	12.47
Chan12:	27	28	31.96	35	1.79

Training set covariance matrix

	Chan 1	Chan 2	Chan 3	Chan 4	Chan 5	Chan 6	Chan 7	Chan 8	Chan 9	Chan 10	Chan 11	Chan 12
Chan 1	1.92	1.50	3.17	4.32	2.17	4.21	2.38	1.94	3.68	2.65	1.04	1.55
Chan 2	1.50	2.87	4.86	6.36	2.84	6.08	4.97	3.82	26.74	0.38	-0.72	2.12
Chan 3	3.17	4.86	13.85	11.78	4.06	12.65	17.56	10.23	33.58	2.81	-18.35	4.20
Chan 4	4.32	6.36	11.78	25.41	12.11	18.05	16.94	-2.56	43.87	27.96	21.73	6.87
Chan 5	2.17	2.84	4.06	12.11	8.23	8.68	5.97	6.33	13.61	14.69	24.87	3.50
Chan 6	4.21	6.08	12.65	18.05	8.68	15.93	15.26	7.92	39.77	11.77	4.35	5.99
Chan 7	2.38	4.97	17.56	16.94	5.97	15.26	27.95	10.21	36.88	14.38	-18.97	4.73
Chan 8	1.94	3.82	10.23	-2.56	6.33	7.92	10.21	64.08	28.00	-24.85	0.23	0.93
Chan 9	3.68	26.74	33.58	43.87	13.61	39.77	36.88	28.00	-2102.21	-33.96	-32.68	5.87
Chan 10	2.65	0.38	2.81	27.96	14.69	11.77	14.38	-24.85	-33.96	-4975.69	58.35	5.50
Chan 11	1.04	-0.72	-18.35	21.73	24.87	4.35	-18.97	0.23	-32.68	58.35	155.49	4.05
Chan 12	1.55	2.12	4.20	6.87	3.50	5.99	4.73	0.93	5.87	5.50	4.05	3.19

Shale 1

Chan1:	357	86	101.62	115	5.83
Chan2:	357	46	59.53	70	4.87
Chan3:	357	68	86.43	101	6.02
Chan4:	357	117	157.30	184	14.81
Chan5:	357	58	84.30	103	9.94
Chan6:	357	135	168.97	196	12.91
Chan7:	357	41	80.60	108	11.10
Chan8:	357	75	110.27	140	11.31
Chan9:	357	92	140.52	189	17.07
Chan10:	357	168	198.23	216	8.51
Chan11:	357	152	181.07	200	9.94
Chan12:	357	59	78.51	93	6.83

Training set covariance matrix

	Chan 1	Chan 2	Chan 3	Chan 4	Chan 5	Chan 6	Chan 7	Chan 8	Chan 9	Chan 10	Chan 11	Chan 12
Chan 1	33.99	26.84	27.09	61.56	43.54	68.53	-20.18	32.82	6.07	-6.37	27.70	36.98
Chan 2	26.84	23.73	24.81	55.18	38.31	59.68	-10.81	29.86	26.76	-4.74	23.28	32.46
Chan 3	27.09	24.81	36.25	77.52	48.70	71.68	18.90	25.72	18.75	12.45	23.62	36.51
Chan 4	61.56	55.18	77.52	-516.98	142.95	-3321.80	65.24	58.54	40.50	-29753.15	3938.16	82.78
Chan 5	43.54	38.31	48.70	142.95	98.89	118.68	31.22	60.51	26.41	40.23	84.36	56.15
Chan 6	68.53	59.68	71.68	-3321.80	118.68	-10510.64	9.31	72.77	-693.90	-46001.68	18512.30	85.43
Chan 7	-20.18	-10.81	18.90	65.24	31.22	9.31	123.25	-20.87	3.00	82.37	25.01	-7.34
Chan 8	32.82	29.86	25.72	58.54	60.51	72.77	-20.87	128.00	45.21	-13.89	57.65	36.50
Chan 9	6.07	26.76	18.75	40.50	26.41	-693.90	3.00	45.21	-445.10	-5545.04	-1272.54	20.99
Chan 10	-6.37	-4.74	12.45	-29753.15	40.23	-46001.68	82.37	-13.89	-5545.04	-63070.36	55916.15	-0.17
Chan 11	27.70	23.28	23.62	-3938.16	84.36	-18512.30	25.01	57.65	-1272.54	-55916.15	40400.88	33.91
Chan 12	36.98	32.46	36.51	82.78	56.15	85.43	-7.34	36.50	20.99	-0.17	33.91	46.61

Shale 2

	No.Pixels	Minimum	Mean	Maximum	Std.Dev.
Chan1:	336	80	97.97	124	7.55
Chan2:	336	42	56.92	75	5.45
Chan3:	336	65	79.77	91	4.75
Chan4:	336	118	153.78	185	11.81
Chan5:	336	59	86.34	112	8.60
Chan6:	336	123	162.24	202	12.94
Chan7:	336	39	79.96	108	11.89
Chan8:	336	92	123.65	154	10.27
Chan9:	336	107	154.80	224	17.10
Chan10:	336	184	201.58	221	6.55
Chan11:	336	173	194.33	214	8.18
Chan12:	336	51	72.97	94	7.15

Training set covariance matrix

	Chan 1	Chan 2	Chan 3	Chan 4	Chan 5	Chan 6	Chan 7	Chan 8	Chan 9	Chan 10	Chan 11	Chan 12
Chan 1	57.05	39.59	27.67	71.37	54.25	92.62	-72.24	40.96	-2.27	-29.22	35.54	50.39
Chan 2	39.59	29.71	21.31	54.51	40.58	68.65	-47.80	29.86	17.61	-21.18	25.76	37.97
Chan 3	27.67	21.31	22.55	47.18	31.78	53.87	-16.68	20.57	3.21	-8.45	11.43	29.07
Chan 4	71.37	54.51	47.18	-643.12	98.06	-2009.19	-49.82	45.81	-778.36	-15265.07	11668.29	76.23
Chan 5	54.25	40.58	31.78	98.06	73.87	104.65	-46.68	50.33	-3.42	-9.15	57.99	55.99
Chan 6	92.62	68.65	53.87	-2009.19	104.65	-4332.18	-94.96	69.42	-1749.80	-32900.69	22233.46	91.25
Chan 7	-72.24	-47.80	-16.68	-49.82	-46.68	-94.96	141.27	-51.35	-16.85	65.60	-40.62	-54.62
Chan 8	40.96	29.86	20.57	45.81	50.33	69.42	-51.35	105.39	0.79	-28.74	41.01	36.20
Chan 9	-2.27	17.61	3.21	-778.36	-3.42	-1749.80	-16.85	0.79	-3033.44	-20186.43	15464.41	6.16
Chan 10	-29.22	-21.18	-8.45	-15265.07	-9.15	-32900.69	65.60	-28.74	-20186.43	65688.69	65535.81	-21.56
Chan 11	35.54	25.76	11.43	-11668.29	57.99	-22233.46	-40.62	41.01	-15464.41	65535.81	61556.58	36.17
Chan 12	50.39	37.97	29.07	76.23	55.99	91.25	-54.62	36.20	6.16	-21.56	36.17	51.13

Shale 3

Chan1:	224	85	103.38	124	7.19
Chan2:	224	45	59.25	74	5.67
Chan3:	224	62	81.41	96	7.24
Chan4:	224	124	153.53	180	10.23
Chan5:	224	61	84.73	103	7.10
Chan6:	224	135	166.67	200	12.78
Chan7:	224	35	68.72	104	13.40
Chan8:	224	87	115.79	147	11.23
Chan9:	224	93	139.50	202	19.20
Chan10:	224	176	196.20	217	7.27
Chan11:	224	151	189.89	216	11.73
Chan12:	224	56	76.42	96	7.66

Training set covariance matrix

	Chan 1	Chan 2	Chan 3	Chan 4	Chan 5	Chan 6	Chan 7	Chan 8	Chan 9	Chan 10	Chan 11	Chan 12
Chan 1	51.69	37.98	30.99	61.05	45.66	86.69	-62.33	42.64	2.66	-31.87	19.27	49.45
Chan 2	37.98	32.20	28.80	47.91	33.40	70.29	-42.73	31.50	33.34	-30.25	4.36	42.44
Chan 3	30.99	28.80	52.41	55.92	23.44	72.44	15.76	6.04	15.64	-15.93	-48.66	42.15
Chan 4	61.05	47.91	55.92	104.76	63.72	-3111.89	-29.78	23.25	7.64	-6775.98	-4988.93	66.75
Chan 5	45.66	33.40	23.44	63.72	50.43	79.49	-54.45	44.66	0.51	-19.64	38.70	44.02
Chan 6	86.69	70.29	72.44	-3111.89	79.49	-8653.17	-74.18	60.70	-1729.86	-30616.22	22918.76	95.28
Chan 7	-62.33	-42.73	15.76	-29.78	-54.45	-74.18	179.66	-93.53	-32.91	68.91	-107.55	-47.68
Chan 8	42.64	31.50	6.04	23.25	44.66	60.70	-93.53	126.01	24.14	-50.07	56.43	34.75
Chan 9	2.66	33.34	15.64	7.64	0.51	-1729.86	-32.91	24.14	-1394.80	-3592.65	-3844.42	29.00
Chan 10	-31.87	-30.25	-15.93	-6775.98	-19.64	-30616.22	68.91	-50.07	-3592.65	-64013.78	62601.03	-36.90
Chan 11	19.27	4.36	-48.66	-4988.93	38.70	-22918.76	107.55	56.43	-3844.42	-62601.08	55112.59	-0.84
Chan 12	49.45	42.44	42.15	66.75	44.02	95.28	-47.68	34.75	29.00	-36.90	-0.84	58.60

Shale 4

	No.Pixels	Minimum	Mean	Maximum	Std.Dev.
Chan1:	378	73	97.13	122	7.55
Chan2:	378	41	58.52	77	6.23
Chan3:	378	70	83.30	105	6.14
Chan4:	378	121	167.06	205	14.69
Chan5:	378	57	89.64	111	9.91
Chan6:	378	129	168.22	215	14.82
Chan7:	378	61	90.28	154	13.05
Chan8:	378	74	100.37	148	9.81
Chan9:	378	108	168.81	234	19.16
Chan10:	378	186	208.63	223	6.20
Chan11:	378	128	193.59	212	11.88
Chan12:	378	49	77.06	105	8.73

Training set covariance matrix

	Chan 1	Chan 2	Chan 3	Chan 4	Chan 5	Chan 6	Chan 7	Chan 8	Chan 9	Chan 10	Chan 11	Chan 12
Chan 1	56.92	45.66	30.62	98.08	67.29	108.60	-65.81	11.99	27.48	-23.48	50.42	63.67
Chan 2	45.66	38.87	25.19	81.38	55.82	90.18	-54.21	11.10	45.19	-21.69	42.03	53.52
Chan 3	30.62	-25.19	37.72	60.75	35.41	66.75	4.86	22.05	12.53	-6.79	-8.14	34.61
Chan 4	98.08	81.38	60.75	-11604.96	141.97	-11439.25	-77.25	2.21	-11233.98	47294.38	29788.58	116.47
Chan 5	67.29	55.82	35.41	141.97	98.19	139.65	-66.60	12.35	43.60	-12.67	87.18	79.73
Chan 6	108.60	90.18	66.75	-11439.25	139.65	-11079.76	104.87	23.84	-12269.76	51491.09	30670.00	126.78
Chan 7	-65.81	-54.21	4.86	-77.25	-66.60	-104.87	170.24	5.13	-61.12	-288.17	-107.22	-74.54
Chan 8	11.99	11.10	22.05	2.21	12.35	23.84	5.13	96.25	21.39	-21.48	-18.79	9.61
Chan 9	27.48	45.19	12.53	-11233.98	43.60	-12269.76	-61.12	21.39	-16321.15	49243.32	31422.77	40.96
Chan 10	-23.48	-21.69	-6.79	-47294.38	-12.67	-51491.09	288.17	-21.48	-49243.32	65671.39	64501.57	-26.66
Chan 11	50.42	42.03	-8.14	-29788.58	87.18	-30670.00	107.22	-18.79	-31422.77	64501.57	59832.15	62.46
Chan 12	63.67	53.52	34.61	116.47	79.73	126.78	-74.54	9.61	40.96	-26.66	62.46	76.29

4.6 Feature(band) selection

The constraint of computer hardware and software requires efficient methods to reduce the dimensionality while retaining good standards of accuracy for classification.

Feature selection is a process of determination of those bands that are most effective in discriminating each class from all other. It includes deleting those bands that provide only redundant spectral information from the analysis.

Separability analysis is one of those methods used to identify subsets of bands from large data sets to facilitate more efficient display and classification of multispectral data. Several measures of separability are available to predict best channels combinations for classification. They are based on measurements of the statistical distances between spectral classes of interest.

In this study, interpretation of twelve set of loadings for twelve eigenvector transformation is used to identify the best channel subsets for use in classification. Those loadings with highest positive and negative values are most likely discriminate between feature of interest. Also, high loadings on original data bands in eigenvectors with greater total variance are more influential in best channel selection than those eigenvectors which accounts for very little variance in the data.

Table 4.7. Eigenvalue and Variance associated with Eigenvectors 1 to 12.

Eigen vec.	Eigenvalue (Variance).	Chan1	Chan 2	Chan 3	Chan 4	Chan 5	Chan 6
1	2083.30 (56.16%)	0.21	0.18	0.27	0.21	0.57	0.35
2	500.88 (13.50%)	0.21	0.11	0.07	0.06	-0.02	-0.03
3	427.10 (11.51%)	0.10	-0.12	-0.17	-0.08	0.11	0.04
4	418.29 (11.28%)	-0.20	-0.04	-0.05	-0.34	-0.09	0.10
5	234.60 (6.32%)	-0.04	-0.02	-0.04	0.07	-0.06	0.11
6	37.73 (1.02%)	-0.31	0.05	-0.15	0.05	-0.11	-0.09

7	4.89 (0.13%)	-0.49	0.16	0.76	-0.05	-0.28	-0.04
8	2.76 (0.07%)	0.22	0.11	0.02	0.54	-0.34	-0.55
9	0.20 (0.01%)	0.12	0.04	-0.05	0.36	-0.53	0.73
10	0.05 (0.00%)	-0.18	-0.18	-0.30	-0.31	-0.34	0.02
11	0.01 (0.00%)	-0.62	-0.30	-0.25	0.55	0.21	0.00
12	0.00 (0.00%)	-0.29	0.88	-0.36	-0.02	0.02	0.00

Chan 7	Chan 8	Chan 9	Chan 10	Chan 11	Chan 12
0.51	0.03	-0.01	0.00	0.14	0.28
0.12	-0.26	0.07	0.83	-0.41	-0.17
-0.19	0.50	-0.12	0.55	0.49	0.25
-0.15	-0.49	0.09	0.04	-0.04	0.76
0.00	0.25	0.95	-0.01	-0.06	0.06
0.07	-0.48	0.20	0.09	0.71	-0.25
0.08	-0.07	0.03	0.04	0.24	-0.04
0.15	0.16	-0.05	0.01	-0.01	0.42
-0.11	0.03	-0.15	0.02	0.00	0.02
0.79	0.09	-0.05	0.00	0.00	0.00
0.04	-0.34	0.02	-0.01	0.00	0.00
0.00	0.00	-0.01	-0.05	0.00	0.00

Table 4.7 Shows the loadings and the percent variance associated with each one of the twelve eigenvectors. Most analysts who utilize eigenvector or component analysis would include the first five eigenvectors (which accounts in this work for 98.77% the total data variance) in there determination. The value of the six eigenvector (1.02%) and the seventh eigenvector (0.13%) are under question. However, eigenvectors with lower variance contains valuable data for selected feature discrimination (Mausel et al., 1990). Eigenvectors with very low variance are dominated by noise; thus, in principle the six through 12 eigenvectors are not considered as important discriminating channels. However, how many eigenvectors should be considered and how high a loading needs to be for consideration is depending on the research problem.

In this analysis, loadings greater than $\pm$ 0.48 were considered important. The loadings of the first five eigenvectors contained 98.77% of the total variance which was seems sufficient to permit identification of the requisite seven most influential channels for feature discrimination. But, addition of channels after evaluation of eigenvector 6 through 12 will increase classification accuracy provided that there is no constraint of hardware and time.

Channel 5 and 7 were identified as important in the first eigenvectors discrimination with a 0.57 and 0.51 loadings. Channel 10 (0.83) was important in the second eigenvector. Channel 8 (0.50), channel 10 (0.55) and channel 11(0.49) were also important in the third eigenvector. Channel 12 had strong loading(0.76) in the fourth eigenvector. Channel 9 (0.95) had strong loading in lower variance fifth eigenvector. Another high loadings (0.76), (-0.55 and 0.54),(-0.53 and 0.73), (0.79),(-0.62 and -0.62), (-0.88) were found on channel 3, 6 and 4, 6 and 5, 7, 1 and 4, and 2 in the relatively low variance of eigenvector 7,8,9,10,11,12. Thus based on the analysis of eigenvectors, channel 5 and channel 7 had the most discriminating power followed in order by channels 10,8,11,12,9,3,6,4,1,2.

At last, six original TM bands (band 1,2,3,4,5 and 7) and eight transformed bands (four PC, two normalized ratio of B5 and B3, and B7 and B4), totally 12 bands were prepared according to the above mentioned parameters for supervised classification.

5. SPECTRAL ANALYSIS OF TM IMAGES OF NORTH-WESTERN MEKELE AREA.

Classification of images allow the preparation of thematic maps from spectral classes according to the users interest. The classes that are part of a legend are information defined by users. In most cases correspondence between spectral classes and information classes is very rare. But, classification process will group together a certain number of spectral classes to define an information. To accomplish quantitatively this goal, supervised and unsupervised classification processes are performed.

5.1 Unsupervised Classification

Unsupervised classification has been performed before supervised classification to examine how automatically classified classes are correlated to field survey data. Thus unsupervised classification was run to produce 11 spectral classes with spectral distance (cut-off) of 30 pixels.

Clustering algorithms used for the unsupervised classification of remotely sensed data generally vary with the efficiency of the clustering (Jonson, 1986). In this work automatic clustering was run on 12 bands using DIMPLE program. The resulting image helps to understand the spectral characteristics of the terrain, and certain classes seem to partially correspond with representative information classes (Fig.5.1). But in general, it can be stated that unsupervised procedure does not seem to be suitable for of lithologic discrimination in the natural condition (relief, vegetation, soil) of the area.

5.2 Supervised Classification

To accomplish supervised classification successfully, it is important to establish the types of land cover for the selected training sites in advance. The analysis of the spectral reflectance characteristic of these sites is

Fig. 5.1 Automatically classi

necessary in order to use the procedure for the classification of the entire image.

The selection of these features on the image needs a field control and interpretation of aerial photographs, as well as compilation of the previous maps of the area. The number of pixels in each feature must be more than ten times the number of classes/features so as to be able to calculate inverse of the covariance matrix of each class/feature.

Univariant and multivariant statistics are performed for the selected training sites (table 4.6), since they represent the fundamental information on the spectral characteristics of the classes. It is very difficult to apply only this information to select the optimum bands for supervised classification, so feature (band) selection is also done (see sec.4.6).

After the selection of twelve bands based on statistical parameters, the appropriate classification algorithms are considered. Parametric and non-parametric are the two types of classification algorithms. The former assumes that the observed measurement vectors are obtained for each class of spectral band during the training phase, while the later make no assumption.

Therefore for the present work, non parametric classification algorithm is used. The most frequent classification techniques of this type are:-

Parallelepiped
Minimum distance, and
Maximum likelihood
Gaussian
City block

The efficiency of the techniques depends on the precise selection of the training site. Maximum likelihood classification technique is recommended for very good training sites. For training sites that are not well defined, minimum distance classifier with standardized distance option performs much better. In this research the result of all the classification techniques are evaluated by producing ten information classes. From these Parallelepiped classification method gives relatively good result (Fig.5.2). The resulting thematic image gives separation of the main landscape units. However, it is still far from a real lithologic map, even if some of the lithological units appear to have been properly recognised, i.e.. the units including Basalt and Ama Aradam formation.

5.3 Post Classification editing.

At this stage of the process, the output map was evaluated so as to check whether the classes obtained on the basis of the training statistics have been matched with the field information. In the result, some of the training sets were found exactly matched with the field information while others represented information class other than they were expected. More than one classes in the map represent single information class, and the numbers of classes were more than what was needed. Therefore, it was necessary to merge the classes that represented the same information class to reach at ten information classes from thirty-one training classes.

Table 5.1 summarises the relationship between training sets and expected information classes and how information classes are merged to produce the actual field information classes.

Table 5.1 Training set evaluation.

No.	Training Set	Expected information Classes	Actual Field information class
1	Basalt 1	Basalt	Basalt
2	Basalt 2	Basalt	Basalt
3	Dolorite 1	Mekele Dolorite	Mekele Dolorite
4	Dolorite 2	Mekele Dolorite	Mekele Dolorite
5	Dolorite 3	Mekele Dolorite	Basalt

6	Laterite 1	Amba Aradam Formation	Amba Aradam Formation
7	Laterite 2	Amba Aradam Formation	Amba Aradam Formation
8	Limestone 1	Antalo Unit 1	Antalo Unit 3
9	Limestone 12	Antalo Unit 1	Antalo Unit 1
10	Limestone 13	Antalo Unit 1	Antalo Unit 1
11	Limestone 14	Antalo Unit 1	Antalo Unit 1
12	Limestone 15	Antalo Unit 1	Antalo Unit 5
13	Limestone 16	Antalo Unit 1	Antalo Unit 3
14	Limestone 21	Antalo Unit 2	Antalo Unit 4
15	Limestone 22	Antalo Unit 2	Antalo Unit 2
16	Limestone 31	Antalo Unit 3	Antalo Unit 1
17	Limestone 32	Antalo Unit 3	Antalo Unit 3
18	Limestone 41	Antalo Unit 4	Antalo Unit 4
19	Limestone 42	Antalo Unit 4	Antalo Unit 2
20	Limestone 51	Antalo Unit 5	Antalo Unit 3
21	Limestone 52	Antalo Unit 5	Antalo Unit 5
22	Limestone 53	Antalo Unit 5	Antalo Unit 5
23	Sandstone 1	Adigrat Sandstone	Adigrat Sandstone
24	Sandstone 2	Adigrat Sandstone	Antalo Unit 2
25	Sandstone 3	Adigrat Sandstone	Adigrat Sandstone
26	Sandstone 4	Adigrat Sandstone	Antalo Unit 5
27	Shale 1	Agula Shale	Agula Shale
28	Shale 2	Agula Shale	Agula Shale
29	Shale 3	Agula Shale	Agula Shale
30	Shale 4	Agula Shale	Antalo Unit 4
31	Shadow	Shadow due to relief	Basalt

5.4 Visual Interpretation

Interpretation of images follow conventional photo geological techniques with an understanding of the physical properties of earth materials.

To supplant digital image processing, visual interpretation of enhanced images are done. Different false colour composites were produced from enhanced images to improve their appearance for visual interpretation (Annex-1). Those combinations which seem more informative on the screen were selected to digitize different features from the screen. Lithologic contacts, structures and lineaments, roads and drainage patterns were digitized separately. These digitized images are joined together and georeferenced to produce a map from image interpretation (Fig.5.3).

Previous workers like Beyth (1972) etc. mapped the Antalo Limestone in five units. In this work, five mappable units are also identified based on their radiometric characteristic, land form, and stratigraphic position.

The lower two units, according to Beyth, Jta and Jtb are mapped in this work as single unit, Antalo unit 1, because of their similarity in brightness value, and Jtc as Antalo unit 2. Jtd of Beyth is mapped as two separate units, Antalo unit 3 and Antalo unit 4 because of their difference in brightness value. The lower cliff forming sub - unit is mapped as limestone unit 3, whereas the upper sub - unit which forms gentle slope and is constituted by intercalation of limestone, marl and mud rocks as Antalo unit 4. The upper most unit (Jte) is also mapped here as Antalo unit 5.

6. GEOLOGY OF THE STUDY AREA FROM FIELD SURVEY.

The rocks and surfacial materials present in an image generally cannot be outlined on the basis of radiometric criteria alone. Either because these surface materials are in a sort of continuum or because of convergence phenomena appear for completely different features. Therefore, within two field trips, 10 and 15 days each, geological field works were accomplished.

Many outcrops in the study area have been considered. Traverses were made along river valleys, road cuts, hill sides and across fault escarpments.

6.1 Description of the outcrops and stratigraphy of the study area

The area comprises Mesozoic sedimentary rocks (Adigrat Sandstone, Antalo Limestone, Agula Shale, and Amba Aradam Formation), trap volcanics and dolorite intrusions. The description of each unit from oldest to the youngest is given below:

ADIGRAT SANDSTONE:

Adigrat Sandstone is exposed in the vicinity of the upper part of Giva river and at the upper part of Hayeku river, south-western part of the study area.

Exposure thickness of the upper part goes up to 150m along Agula river. Down the stream from Suluh river and Genfel river junction, sandstone forms gentle slope and is characterized by reddish colour, friable nature, cross bedded structure, and coarse grain . Along the Agula river it turns into cliff forming, finning up sequences made by cross bedded, reddish, well bedded sandstone at the base.

Adigrat sandstone is overlain by Antalo limestone with a clear transitional contact. The transitional contact is a few meters thick, with an increase in limestone and marine fossils up wards. At the upper part of Hayeku River, the contact is characterized by dolorite intrusion, 60 cm thick intercalation of marl and shale, and a 2 m thick sandstone outcrop with maximum bed thickness of 25 cm. Near Hagere Selam, the passage between Adigrat Sandstone And Antalo Limestone is characterized by a 50 m thick intercalation of layers of fossiliferuos sandstone and coquinoid limestone. The sandstone layers are generally thicker at the base, but on the top they are very thin with coquinoid limestones prevailing.

ANTALO LIMESTONE:

Antalo limestone consists of five units (Beyth 1972). The bottom most unit, having a total thickness of 155 m, forms the first distinct cliff next to Adigrat sandstone. It is exposed, within the study area, in the vicinity of the upper part of Hayeku River and around the junction of Suluh River and Genfel River. The contact between Adigrat Sandstone and Antalo Limestone is characterized by fossiliferous sandstone, which is gradually changed into fossiliferous limestone. Maximum bed thickness measured is around 3 m. Within this unit of the Antalo limestone, bed thickness increases upwards, and the rock becomes massive and jointed near the top. The upper part is non-fossiliferous. Shale occurs along the bedding plane. In the middle part, 30 cm thick beds are measured, intercalated with shale and marl. Near the bottom, bed thickness reaches up to 10 cm intercalated with 2 to 7 cm thick marl. Fossil content increases downwards and become fossiliferous near the contact.

The second unit outcrops in the central and south western part of the area overlaying the basal unit. It forms gently terraced slope. The bottom most part of this unit, whose exposure thickness is about 10 m, consists of intercalation of fossiliferous limestone and marl. Along the new road to Hagere Selam, 3 to 4 km from the junction to Wukro road, the lower part of Antalo Formation is characterized by very fossiliferous coquinoid limestone, intercalated with fossiliferous, cross bedded reddish sandstone. The most abundant fossils, which form fossil horizons along the beds, are ostreid bivalves. These are followed by limestone beds which are 14 m thick and non fossiliferous. The maximum bed thickness is 1.5 m. Overlaying this, about 13 m thick intercalation of limestone, yellow marl, and mud rock, which is non fossiliferous, is observed. The thickness of the limestone beds ranges from 10 to 120 cm. Altered laminated soft materials appeared along the bedding plane of the limestone beds. Their thickness is about 60 to 80 cm. Mud rock with a thickness of 60 cm, white grey in colour, is intercalated with limestone. No fossils are observed with the exception of the top 20 cm thick, altered mud rocks which is highly fossiliferous.

The next unit is exposed in the north central and south western part of the study area. Its base consists of a 14 m thick fossiliferous, cliff forming limestone beds intercalated with 40 cm mud rock. Bed thickness ranges from 8 to 80 cm. Overlaying this 28.5 m thick limestone beds of bed thickness 20 to 25 cm, intercalated with 2 to 7 cm marl, both are non fossiliferous, and arranged in beds followed. A 2 m thick limestone bed without observable fossils and white grey in colour is overlain by a 2 cm thick calcite bed along the bedding plane. It is followed by a non fossiliferous, yellowish white limestone intercalated with marl and mud rocks. A 110 cm thick limestone bed overlies the intercalated rocks and it is intern followed by intercalation of marl, limestone and mud rocks. The lower part of it is fossiliferous with calcite inter growth along joints. Altered soft sediments are observed along the bedding plane. Overlying this, non fossiliferous limestone beds intercalated with laminated mud rocks are observed.

The 4th unit of Antalo limestone is exposed in most of the central part of the study area. It forms cliff and gently terraced slopes. This unit consists of two sub units.

The lower sub unit is characterized by more massive (up to 3 m thick), jointed limestone beds intercalated with shale and marl of 10 cm thick. It displays karst features, solution channels, stylolite structures, and caves. The upper sub unit consists of two cliff forming fossiliferous (rich in corals, echinoderms, and gastropods) limestone beds(up to 210 cm thick) separated by gently terraced slope constituted by intercalation of non fossiliferous marl and limestone, and rarely fossiliferous limestone . Fossils are weathered into brownish circular materials.

The upper most unit, which is exposed in north and central south western part of the area, consists of two sub units. The lower most sub-unit forms distinct cliff. It is constituted by massive, rarely fossiliferous limestone beds. Maximum bed thickness measured is about 70 cm. The top sub unit is characterized by yellowish marl intercalated with thin layers of limestone. The bottom part is characterized by intercalation of jointed, friable, up to 1m thick sandstone, 3 m thick layered (maximum bed thickness of 40 cm) black limestone, white pinkish, rarely fossiliferous and grey colour, non fossiliferous limestone, and 10 cm thick shale. The top most part of this sub unit is made of about 20 m mudstone-wackestone forming the last cliff of the landscape.

AGULA SHALE:

Agula shale is exposed in the study area at the eastern and western part, covering flat land form and gentle slopes. It ranges in colour from pale yellowish grey , which is friable, to light blue dark and indurated. All variety of Agula shale are fossiliferous rich in bivalves and gastropods. Generally the orientation of bivalves on the bedding plane of the friable shale is uniform. In most places, Agula shale is cut by dolorite which forms cliffs within the Agula shale. Shale beds are intercalated with lenses of cherts beds mostly near the contact of dolorite and shale. The bottom most part of this unit is characterized by intercalation of variegated shale, marl, black limestone and limestone. On the beds of limestone that is non fossiliferous burrow structures are observed while ripple marks are common on fossiliferous beds. The middle part consists of intercalation of 10 cm marl and 7 cm shale yellowish in colour, fossiliferous overlaying the non fossiliferous, grey colour intercalation of jointed marl and shale. This is followed by isolated patches of gypsum beds of 10 m thick. Gypsum beds are intercalated with 30 cm thick marl and shale, and 10 cm thick fossiliferous limestone. Maximum bed thickness measured on the gypsum outcrop is 30 cm. Gypsum beds are highly affected by weathering and display nodular structures. Within the white nodular gypsum beds, pinkish nodular gypsum beds are observed. Overlaying these are intercalation of shale with about 10 cm thick reddish siltstone beds. The upper most part of this unit is composed of intercalation of fossiliferous limestone, 10 to 15 cm thick, variegated shale, non fossiliferous, yellowish sandy limestone, yellowish siltstone, and non fossiliferous sandstone. Fossils, within the upper part of the Agula shale, decrease in abundance towards the top. The distribution of gastropods increases towards the top while the abundance of bivalves decreases. Agula shale is overlain by 1 m thick coarse grain sandstone, part of the Amba Aradam formation, which is followed by a 40 cm thick chert without a clearly observable contact with the shale.

AMBA ARADAM FORMATION:

This unit outcrops at the flank of the mesas formed by trap volcanic at the eastern part of the study area. The overall thickness of this formation is about 20 m. Amba Aradam formation consists of medium grained, cross bedded, pinkish up to 2m thick sandstone intercalated with red and variegated lateratized siltstone and sandstone without defined structures. This unit forms steep cliff near the base of mesas.

TRAP VOLCANICS:

Trap volcanics unconformably overlays the lateratized Amba Aradam formation forming mesas in the vicinity of Hagere Selam. Near the bottom part of this unit patches of very light coloured materials most probably chert, are observed.

6.2 Regional Stratigraphy of the Area

Arkin et al., 1971, Beyth, 1972 summarises the regional stratigraphy of the area from the youngest to the oldest as:

Cenozoic

Tertiary

Mekele dolorite

-Andesine dolerite

Trap volcano

-Olivine basalt with minor interbedded lacustrine deposits.

Mesozoic

Cretaceous

Amba Aradam formation

-Laterites.

-Clay, silt, sandstone, pebble conglomerate and lateritized silty clay .

Jurassic

undifferentiated

-Limestone and sandstone

-Finely crystalline limestone, marl and shale.

-Limestone and limestone with minor marl.

Agula Shale

-Marl and shale with minor coquina and black limestone characterized by thin gypsum and dolerite beds.

Antalo Limestone

-Marl interbedded with coquina and fine grained limestone

-Finely crystalline limestone with some coquina and marl

-Marl with black coquina and sandy limestone

-Coquina, Oolitic limestone, and marl

-Finely crystalline sandy limestone and marl

Adigrat Sandstone

-Siltstone and fine to coarse grained sandstone

-Minor calcareous sandstone

-Ferrigenous silt and clay

Palaeozoic

Ordovician

Edaga Arbi Glacial

-Tillite, containing granite boulders up to 6 meter in diameter.

Enticho sandstone

-Sandstone, commonly calcareous, with lenses of polymict conglomerate and tillite

6.3. Geological structures of the Area

According to Merla and Minucci, (1938), Beyth, (1972) and Arkin et al., (1971), geological structures of the Mekele outlier are characterized by two system of faults. The first system of faults run in en echelon form in west-north-west direction including four fault belts. These are the Wukro, Mekele, Chelekwot and Felega Mariam fault belts. They are normal, but the first three dip southward at moderate to steep angles whereas the last fault belt dips towards the north. A large part of the displacement probably occurred after the deposition of the Agula shale, but before deposition of the Amba Aradam formation.

The 2nd system of faults are normal, dipping eastward, and trending 360^0 in the north and 340^0 in the south. They are part of the Rift Valley faults which formed the western escarpment of the Rift Valley.

A few lineaments up to 30 km long are also identified crossing the exposed rock units.

6.4 Reconstruction of the composite stratigrafic column of the area in relation to the Mekele outlier.

The Mesozoic sedimentary succession of Tigray outlier is constituted primarily by the following formations:

1) Adigrat Sandstone
2) Antalo Limestone
3) Agula Shale
4) Amba Aradam Sandstone

The entire sedimentary succession either lies (unconformably) on the basement (Precambrian-Early Palaeozoic) or lies on the continental and glacial deposit (Late Palaeozoic, known as Enticho Sandstone and Edaga Arbi Tillites). The stratification is almost horizontal, with the exception of local dips and folds, which are related to faults in the Ethiopian rift.

1) Adigrat Sandstone.

For this formation Merla and Minucci (1938) reported a thickness varying from 100 to 500 m; whereas Beyth (1972) reported a value ranging from 670 to 80 m for the region around the Tekeze river, disappearing completely towards the Adigrat-Axum road.

Near Enticho village, this formation lies on continental and glacial sediments (Late Palaeozoic), whereas North and South of this area, it lies directly on the basement. In general, Adigrat Sandstone is sub horizontally layered, with each bed about 30 cm thick, and is made up of fine-medium grained sandstone at the base and at the top, forming a classic finning up, point bares sequences, intercalated with a red clay and silt. Moving upwards the bed thickness increases up to one meter, displaying coarse tabular, plannar cross-bedded sand.

Occasionally, reactivation surfaces are present with the bottom filled with pebbles and silicified wood fragments. On the other hand, near Adigrat, the more common lithologies are argilloschists and sublaminar red clays intercalated with thin cross-bedded fine sand, a few decimetre thick.

Adigrat sandstone is clearly emphasized by the smoother and wavy (?) morphology; on the other hand sandstones are characterized by steep cliffs.

Regarding the age of this formation, Merla and Minucci (1938) and Russo et al. (1994) gave an age ranging from Trias to Oxfordian. The base of the formation is not precisely dated; whereas a late Callovian age has been given for the top, the reason being that the base of the overlying Antalo Limestone is dated Oxfordian due to the presence of the Benthic foraminifer *Kurnubia palestiniensis* (Russo et al. 1994).

From a paleoenvironmental point of view, the Adigrat Sandstone shows the typical feature of a continental, fluviodeltaic deposit, as described by Beyth (1972), Bosellini (1989), Russo et al. (1994).

2) Antalo Limestone

The Antalo Limestone outcrops in the middle part of Mekele outlier and, to the East, reaches the Danakil Alps. This formation is subdivided in to five lithological members (Jta-Jte) by some authors (Beyth, 1972); and a total thickness of approximately 700-800 m is given. A composite stratigraphical succession, sampled near Wukro for the basal part and near Mekele for the remaining part, is shown in figure 6.1.

The basal part, which is very well exposed along the Wukro-Atsbi road, is transitional with the underlying

Adigrat Sandstone; it is made up of quartz - rich packstone with a few bioclasts. Upwards it grades first to wackestone with benthic forams and other bioclastic debris, then oolithic packstone-graystone - rich in mainly silicified seleratinian corals, stromatoporoids and molluscs. The fossil content is constituted by *Kurnubia palestiniensis, Nautiloculina oolithica, Valvulinids* (benthic forams), *Dermoseris sp.* and *Amphiastraea sp.*(sleractinian corals), and *Steineria somaliensis* (stromatoporoid). Finally it changes to alternating wackstone and marl, and ends with a thick oolithic bed. The succession continues along the road built on the cliff north of Mekele, where, at the base, marly lithotypes are interbedded with hardened layer made up of mainly *Nanogyra sinuata* (Ficcarelli) coquina. The main beds, however, contain brachiopods, as *Somalirhynchia somalica* (Dacque), *Terebratula pelagica* (Rollier), *Zeilleria Ltifrons* (Krumbeck), and bivalves, As *Venilicardia hunti* (cox), *Pholadomya aubryi* (Douville), *Mactromya quadrata* (Rollier). *Mactronia sp.* and *Cyprinids*. Above the base, silty and burrowed limestones are interbedded with thin marly beds rich in *Nanogyra sinuata* and *Gryphaea sp.* The upper part of the cliff is made up of thick beds of mudstone-wackestone with scattered lenses of coarser bioclastic debris. The succession continues with about 30 m of marls and limestones, including two key beds constituted by oolithic, low-angle cross bedded limestone very rich in Nerineids.

Approximately ten km north, still along the Mekele-Wukro road, planar cross-bedding grainstones outcrop; they grade upwards and include large lenses of Nerineids at the base and scattered ones at the top. The succession continues with packstone-grainstone which, upwards, are separated from an other grainstone bed by a thin clay bed. Above this, a reactivation surface, rich in bioclatic fragments at its base, is transitional to a wackestone-mudstone containing stromatoporoids, ostreids, echinods and gastropods. Among

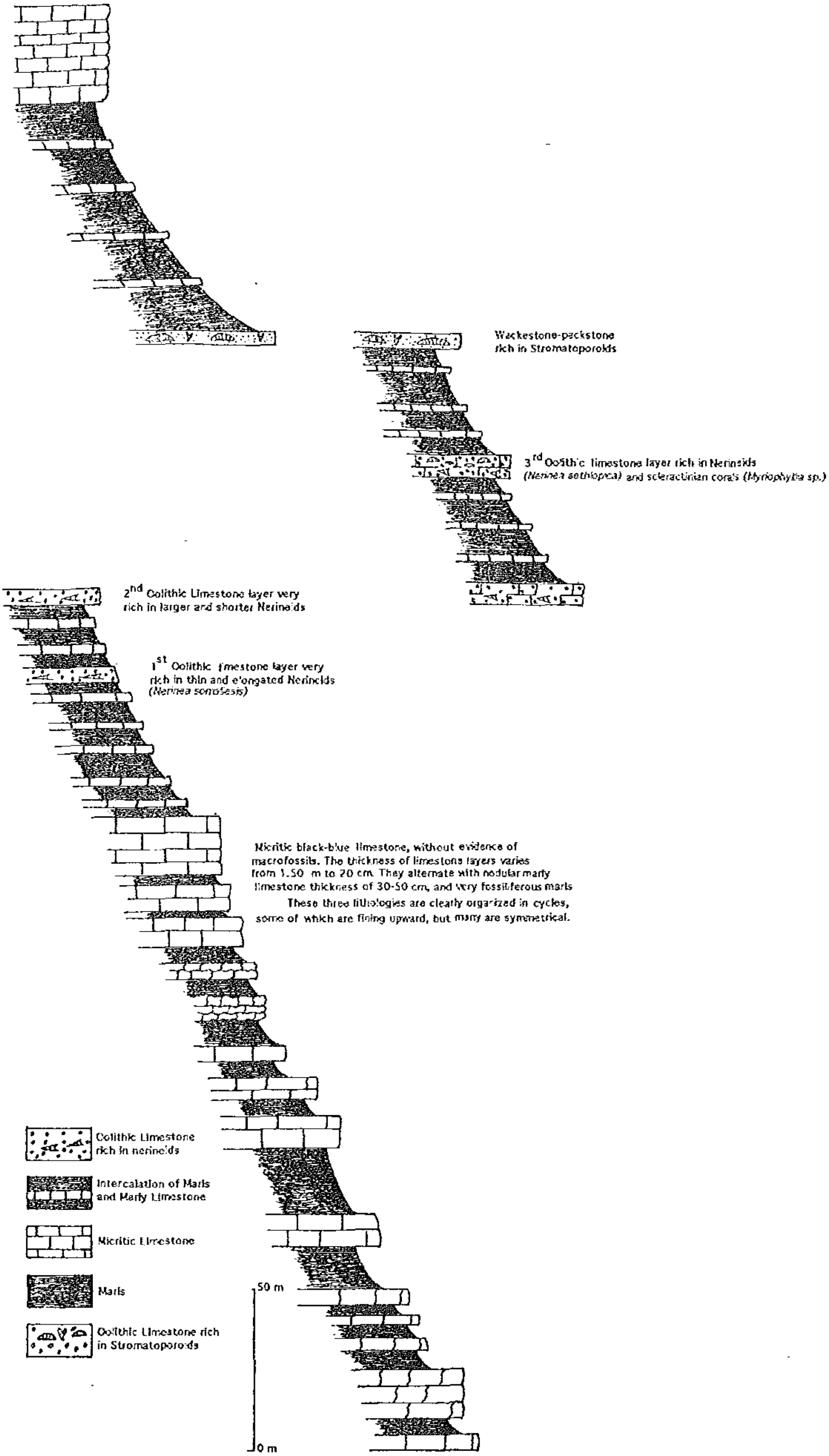

Fig. 6.1 Composite Stratigraphy of Antalo limestone in the study area.

the stromatoporoids, *Promillepora pervinquieri, Stromatopora gortanii, Stromatopora douvillei and Burgunia sp.* are present. Among the gastropods, *Ampullina (Ampullina aff. heamispherica)* is the most common species, whereas the Nerineids are represented mainly by *Nerinea desvoidyi aethiopica* Jaboli. Moving upwards, there is a layer very rich in bivalve *Lima (Plagiostoma) bianchii* Jaboli, which is followed by a patch - reef made up of small groups of ostreids. These, in turn, are colonized by tabular colonies of scleractinian corals (mainly genus *Myryophyllia*). Stems of crinoids of different species are in abundance also are small brachiopods (*Zeilleria hararina* Jaboli, *Terebratula suprajurensis* Muir-Wood, *Terebratula gortani* Jaboli), some bivalves (*Pholadomya protei* Brongnart), one species of regular echinoid (*Recrosalenia sp. aff. somaliensis* Currie), one species of irregular echinoid (*Clypeus* sp.aff. *williei pentagonus* Currie).

Clay marls interbedded with thin calcareous beds outcrop above and along this patch reef. The top ends with a thick bed of stramatolitic limestone intensely burrowed at its base.

Upwards the succession continues with intercalations of marls and thin beds of coquinoids limestones capped by a thick bed very rich in stromatoporoids and ostroids. The last part of this formation is made by about 100 m intercalated with very thin limestone beds, which ends with 20-30 m of micritic limestone. The passage to Agula shale is gradual and indistingushable.

7. EVALUATION OF REMOTE SENSING TECHNIQUES IN LITHOSTRATIGRAPHIC MAPPING OF NORTH WESTERN MEKELE AREA.

7.1. In Lithological Mapping.

Maps made from remotely sensed images are not as accurate as those produced by conventional field mapping because of different approaches. In conventional mapping, in the field, geologists closely examine individual bedrock outcrops and the result is a bedrock map that depict the distribution of various rock types where surfacial materials including vegetation are stripped off. In contrast, image interpretation map depicts additional units which represent surfacial cover. These materials might not necessarily correspond to geologic units which might be mapped in the field due to the following factors:

1) vegetation cover:- natural vegetation may be specific to a particular lithology. Moreover, the type and extent of vegetation cover often reflects only the influence of topography, relative rain fall, and the maturation stage of the floral community.

2) soil cover:- soil cover and other surfacial deposits can greatly affect the spectral appearance of the ground and can mask structural features and other indicators useful for lithological identification.

In addition to these spectral features of most rock types and derived soils are not very distinctive in the wavelength region sensed by most existing instruments (visible and NIR). Even the EM response recorded over a rock unit is a function of several factors such as composition of the rock, state of weathering, moisture content, and so on.

Many methods are applied to improve the above mentioned problems. Contrast enhancement, band ratioing, and classification helps lithologic mapping in many aspects. In general unsupervised classification has met less success for geological application. Whereas for supervised classification, even with carefully chosen training areas, accuracy doesn't exceed 75%,. This is due to the influence of soils, vegetation cover, topography, intercalated facies and transported surfacial materials which mask and alter the spectral characteristics of the underlying rocks. These factors make difficult selection of representative training areas which correspond to the bedrock; especially in this area where the terrain is highly dissected and affected by active weathering.

In this work, Remote Sensing techniques are found to be very helpful in visual interpretation because of their capability to provide scene-optic view of a very large area with significant detail for lithological mapping. Specially they provide:-

-the possibility to examine small scale features in relation to a more regional context.

-the possibility to extend lithological contacts over large area with minimum ground control.

-the possibility to extrapolate the identified rock types on the basis of spectral and geomorphic information.

-the possibility to interpolate structures, starting from mapping lineaments which were not evident during field survey.

7.2 In Reconstruction of the Stratigraphy.

Determination of the lithology of the individual lithostratigraphic unit was a problem since SPOT's 20 m and TM's 30m resolution didn't permit recognition of micro morphologic features and certain rock characteristics, such as texture, resistance, etc., which are criteria for lithologic identification. This was only partly compensated by tone differences of some rock types. But tone has relatively limited help to identify lithologic units on 3 bands of SPOT and 6 bands of TM. But, colour composites were produced to discriminate at least ten surfacial units in this work.

Intercalated facies and thickness variation of several units, shadow effect, and illumination angle of the sun give different tone for the same lithologic units, and created many problems to correlate units from one part of the image with those of another.

It was also very difficult to correlate lithostratigraphic units and sub-unit that are differentiated on the basis field data such as structure, texture, fossil content with stratigraphic units extracted from image processing and interpretation.

Under these circumstances, the geological map prepared here shows ten different units with only a very generalized correlation with field observation. It is preferable, in the absence of a sufficiently accurate determination of the lithology of the units, to give a generalized description of the main stratigraphic subdivisions.

8. Paleogeography of the Mekele Sedimentary Basin in reference to other Main Sedimentary Basins

The history of the Mesozoic sedimentary basin of Tigray outlier is related to the following main stages and events which affected the entire Horn of Africa.

After the *intra continental rift stage* which preceded the Gondwana break-up, in Late Palaeozoic-Jurassic time, and formed fault-controlled aulacogen-like basins (Fig.8.1), the entire East African Craton is covered by the besal clastic sediments (Adigrat sandstone) corresponding to the *post rift stage* (Russo et al. 1994).

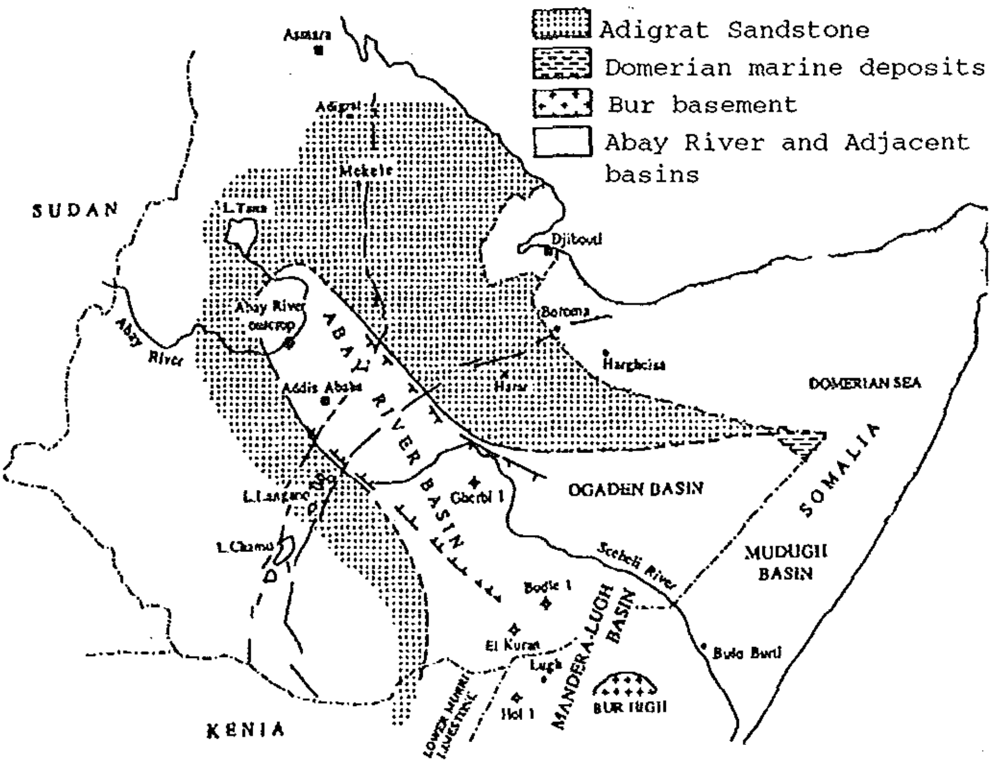

Fig. 8.1. Paleogeographic map of Ethiopia in the Early-Middle Jurassic time (Russo et al., 1994).

The Adigrat sandstone, which levelled the previous topography related to the former aulacogen-like basins, has different facies, thickness and age. In the Mekele outlier the thickness varies from few meters north of Adigrat-Axum road to about 700 meters near Abi Adi. The age is dichronous ranging form Triassic to Callovian.

This post rift stage is followed by *early flooding of craton* which restricted only the rifted basins, sited near the future continental margin (Early Liassic time). In Ethiopia, the lower part of the Gohatsion Formation outcoping in the Abay River Basin, which constitutes one of these rifted fault controlled basins, represents the beginning of this marine transgression over the Ethiopian craton, in Toarcian time (Russo et al.1994). On the contrary the marginal areas, which are higher with respect to these depressed areas, were subjected either to erosion or underwent continental deposition (Harrar, Tigray, etc.).

As a consequence of the Gondwana break-up and formation of the African continental margin, the entire East African craton was drowned by a Callovian-Oxfordian transgression. The Callovian-Kimmeridgian Antalo Formation is the equivalent of this sequence in the Abay River Basin and Tigray Outlier. This sequence starts with open shelf where fossiliferous marl and marly limestone are intercalated and continues with open sea, where ammonite-rich marl is deposited, followed by gradual return to carbonate, and generally, shallow sediments rich in corals, nerineids and stromatoporoids (upper most oolitic, reefal limestone). The age of this sequence is Oxfordian-Kimmeridgian in Tigray (Russo et al.1994).

From Oxfordian the transgression was spread over the entire East African craton. At the end of Jurassic time, the sea began to withdraw from the Horn of Africa, probably as a result of the intra-plate effect of the separation of South America and Africa (Bosellini 1989). The deposition of supratidal-fluviatile Mugher Mudstone unit and continental Debre Libanos Sandstone in the Abay River Basin, and of the continental, fluviatile Amba Aradam sandstone is an effect of these events.

9. Conclusion

It is Known that the use of spectral signature in the VIS, NIR and SWIR regions is limited to the knowledge of the significance of the physical values that are taken into account in the satellite data. Mapping by remote sensing techniques strictly depends on the response of the upper 50 μm thick surface materials in the above spectral regions. This information shows that some rock units are theoretically distinguishable and that discrimination processing techniques may be carried out. In the vegetated, highly dissected and weathered areas, spectral values are poorly differentiated in the NIR bands, and in this case the image shows only main variations of the topography. Geological features are generally better exposed by the geomorphology than from variation in spectral signatures.

In the area under study, active erosion resulted in topographic differentiation of the rock that weathered differently. The different rock units are covered by homogeneous soil. Different rock types appear intercalated with each other, for instance, the sandstone unit consists of variegated shale intercalated with it; shale unit consists of silt stone, sandstone and marl; different limestone units are intercalated with different mud rocks. Rugged topography of the area creates shadow. As a result, the same rock may show different colours. For these reasons, the processing techniques exposing geology are not very efficient.

An important result has been obtained through image visual interpretation by following conventional photo interpretation techniques. Different features (structures, lineaments, drainage patterns) have been digitized separately and joined together to prepare a final geological map.

Satellite images, in general, and SPOT and TM images in particular, are found very helpful to identify and follow (trace) marker beds in regional scale to control the stratigraphy of the area. However, the resolution of these sensors doesn't permit to identify micro morphological features and typical rock characteristics (texture, structure, resistance, fossil content, etc.) which are criteria for lithostratigraphical identification.

Adigrat sandstone is the oldest unit in the area deposited during Triassic and Callovian time. This is conformably overlain by Antalo limestone, which has been deposited starting from Late Jurassic (Oxfordian) up to Kimmeridgian under marine environment. Agula shale, which is overlain the Antalo limestone conformably, has been deposited under shallow marine environment and semi-arid condition. Amba Aradam Formation which consists of lateratized sandstone, siltstone and shale has been deposited under arid environment.

Presence of sand beds intercalated with Antalo limestone and Agula shale indicates the influence of continental sediments during the deposition. Intercalation of marl and mud rocks with limestone indicates that fluctuation of the sea level that has taken place during the time of deposition.

Two major fault systems, which are part of Mekele fault belt and the rift valley faults, are observed from field survey as well as from image interpretation. The first system of faults run in en echelon form in west-north-west direction. These faults dip Southwest, and affect the whole sequence with the exception of the Amba Aradam formation and the trap volcanic. And, the second system of faults dip eastwards, and their effect is evident on the whole sequence.

10. References

1. Arkin, Y., Beyth, M., Dow, D.B., Levitte,D., Hailu,T., Hailu, T. (1968-71). Geological Map of Mekele Sheet.
2. Beyth, M. (1971). The Geology of Central - Western Tigray. Geological Survey of Ethiopia, Min. Mines, Addis Ababa. Unpublished Report.
3. Beyth, M. (1972). Paleozoic - Mesozoic Sedimentary Basin of Mekele Outlier, Northern Ethiopia. Vol.56, No.12, 2426 - 2439.
4. Bosellini, A. (1989). The Continental Margins of Somalia: their structural evolution and sequence stratigraphy, Vol.XLI, 373-458.
5. Chorowicz, J ,Kim, J., Manoussis, S., and Rudant, J.P. (1989). A new Technique for Recognition of Geological and Geomorphological pattern in Digital Terrain Model. R. S. Environment-29:229 - 239.

6 Chrowicz, J., Deroin, J.P., Gess, G., Huger, J., Becue, B., Curnelle, R., Perrin, G. and Ronfola, d.(1991). A Methodology for the use of SPOT imagery in oil exploration, Example of the BAS LanGuedoc Exploration permits area (France). Int. J. R. S., Vol.12, No.10, 2087-2108.

7. Chrowicz, J., Lavreau, J., Tamian, G., Theunissen, K., Bardinet, C., Girault, F., Klerkx, J., Lepage, A., Nanyaro, J., Nimpagaritse, G., Nkanira, T., Ntungicimpaye, A., Roggeri, I., Rudant, J. P., Ruder J., Tack. L. Temu, E., Thoun, C., Tretois, P., and Yanda, P. (1990). The evaluation of satellite imagery and field spectro - radiometer data for the study of the lithology and the ancient and reactivation tectonics in the vicinity of the East African Rift. ISPRS J. of photogrammetry and R.S., 45(1990), 355 - 381.
8. Durary, S. A. (1987). Image Interpretation in Geology.

9. Ethiopian Meteorological Service (1979). Meteorological Maps of Ethiopia.
10. Freund, J. E.(1979). Modern Elementary Statistics, 5th Ed.
11. Ficcarelli, G., Radrizzani, p. C., and Turi, A. (1975). Analyses of the Microfacies of Antalo Limestone in the Dire Dawa, Ethiopia. Boll. Soc. Geol. It., 94(1975), 759 - 770.5ff.
12. Gupta, R. (1991). Remote Sensing in Geology.
13. Jackson, K.C. (1970). Textbook of Lithology.
14. Jensen,J.R. (1989). Introductory Digital Image Processing
15. Levitte, D. and Tsegaye H. (1968). Preliminary Geochemical Survey on the Enticho Gossan. Geological Survey of Ethiopia. Minor Investigation Note 1968/5.
16. List, F. k. and Schoele, R. (1990). Satellite Remote Sensing Application in Geology, Land Use, and Mineral exploration in Egypt and Sudan. Berliner Geowiss, Abh. Reihe A, Band 120.1, 399-418.
17. Liwang and He, D. C. (1990). A New Statistical Approach for Texture Analysis. Photogrammetric Engineering and R. S. Vol. 56, No.1, 61-66.
18. Lyberis, N. (1990). Geological Features of the Spirsbergen region obtained from multispectral SPOT data and field radiometer measurements. int. J. R. S. vol.11, No.2, 253-265.
19. Merla, G. and Minucci, E. (1938).Missione Geologica nel Tigrai. Rend. Accad. Itl., Cent. studi I'A.O.I., 3:1-362;Roma.
20. Mausel, P. W, Kramber, W. J., and Lee, J. K. (1990). Optimum Band selection for Supervised Classification of multispectral Data. Photogrammetric Engineering and R. S., Vol.56, No.1, 55-60.
21. Mohr, M. H., Woldai, T., and Dijk, P.M.P. (1992). Image processing for detecting environmental pollution in a

coal mining district, Montalban area, Spain. ITC J., (1992-2), 148 - 153.

22. Mohr, M.D.V.H. (1990). Camera and Multispectral scanning systems in remote sensing as applied to Geology. Part I: data collection. Itc

23. Morton, W. H. and Black, R.(1975). The Geology of Enticho, Tigray. Bull. Geophys. Obs. Addis Ababa 15, 1 - 15.

24. Short N. M. (1982). The Landsat Tutorial Workbook.

25. Peng Gong and Howarth, P. J. (1990). The use of Structural Information for improving Land-cover classification Accuracies at the Rural-Urban Fringe. Photogrammetric Engineering and R. S., Vol.56, No.1, 67 - 73.

26. Russo, A., Assefa, G., and Atnafu, B. (1994). Sedimentary evolution of the Abay River (Blue Nile) Basin, Ethiopia. N. Jb. Palaont. Mh. 291-308

27. Sesoren and Voute (1990). Remapping from the first SPOT images of Djebel Amour. ITC Journal, 1990-4,369 - 372.

28. Siegal, S. B.(1979). Remote Sensing in Geology.

29. Turi, A., Bigi, L. and Radrizzini, P.C. (1980). Microfacies of the Antalo Limestone (Middle to Upper Jurassic) in some sections of East - Central Ethiopia. Boll. Soc. Geol. It., 99(1980), 473 - 454,8 ff.

30. Weber, c. (1985). Geological Remote Sensing. ITC Journal, 1985-4, 227 - 241.

31. Valenlvela, C. R. and Baumgardner, M. f. (1990). Selection of appropriate cell size for thematic maps. ITC J. (1990-3), 219 - 224.

Annex 1. Description of False Colour Composites

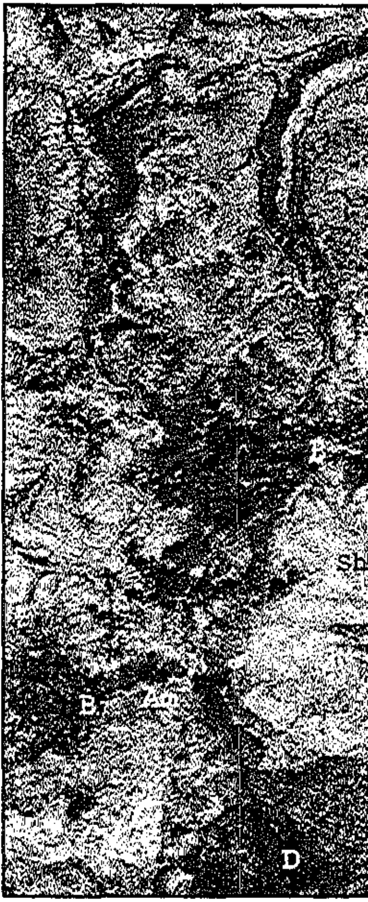

COLOR PLATE 1. False color co
easly the Basalt unit (B), three
Formation and Basalt have mor
Agula Shale (Sh) has similar col

COLOR PLATE 2. False color com
band 4. Vegetation distribution is
which were similar in appearance
similar in appearance.

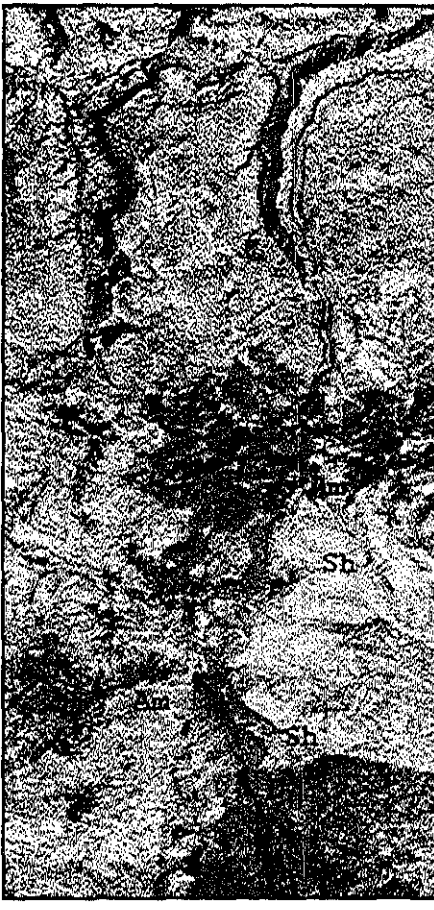

COLOR PLATE 3. False color compos
No clear tracable contact is observed

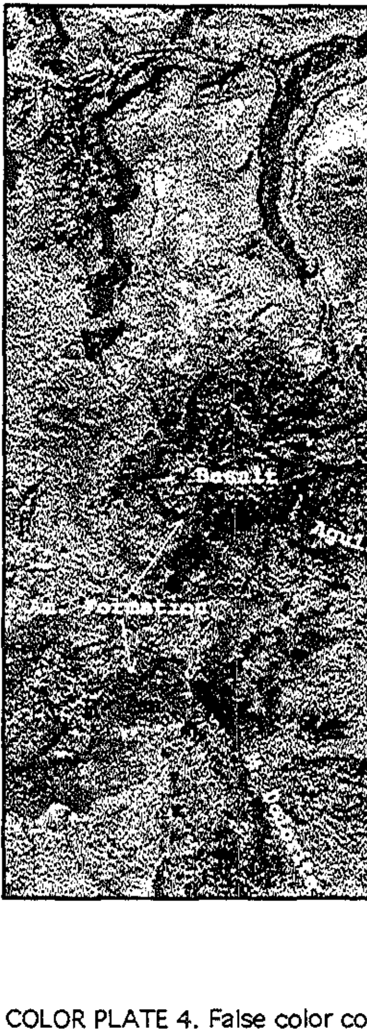

COLOR PLATE 4. False color co
features which are mostly asso

COLOR PLATE 5. False color co
other combinations and in each
with its surrounding. Five distin
(SS), Basalt (B), Amba Aradam
of the image.

Annex 2. Image cross plots and correlation matrix

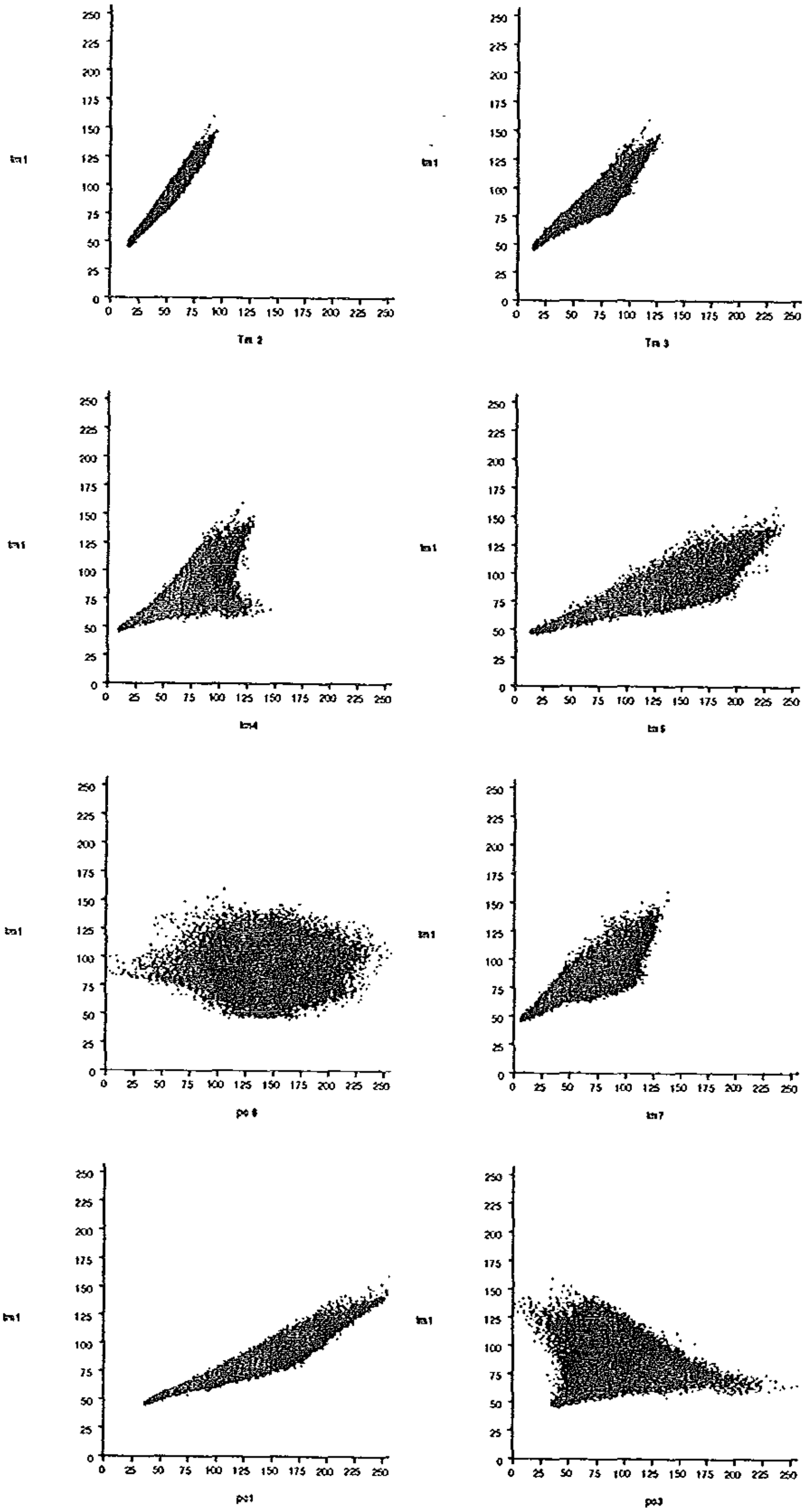
tm1
Tm 2
Tm 3
tm4
tm7
po1
po3
0 25 50 75 100 125 150 175 200 225 250

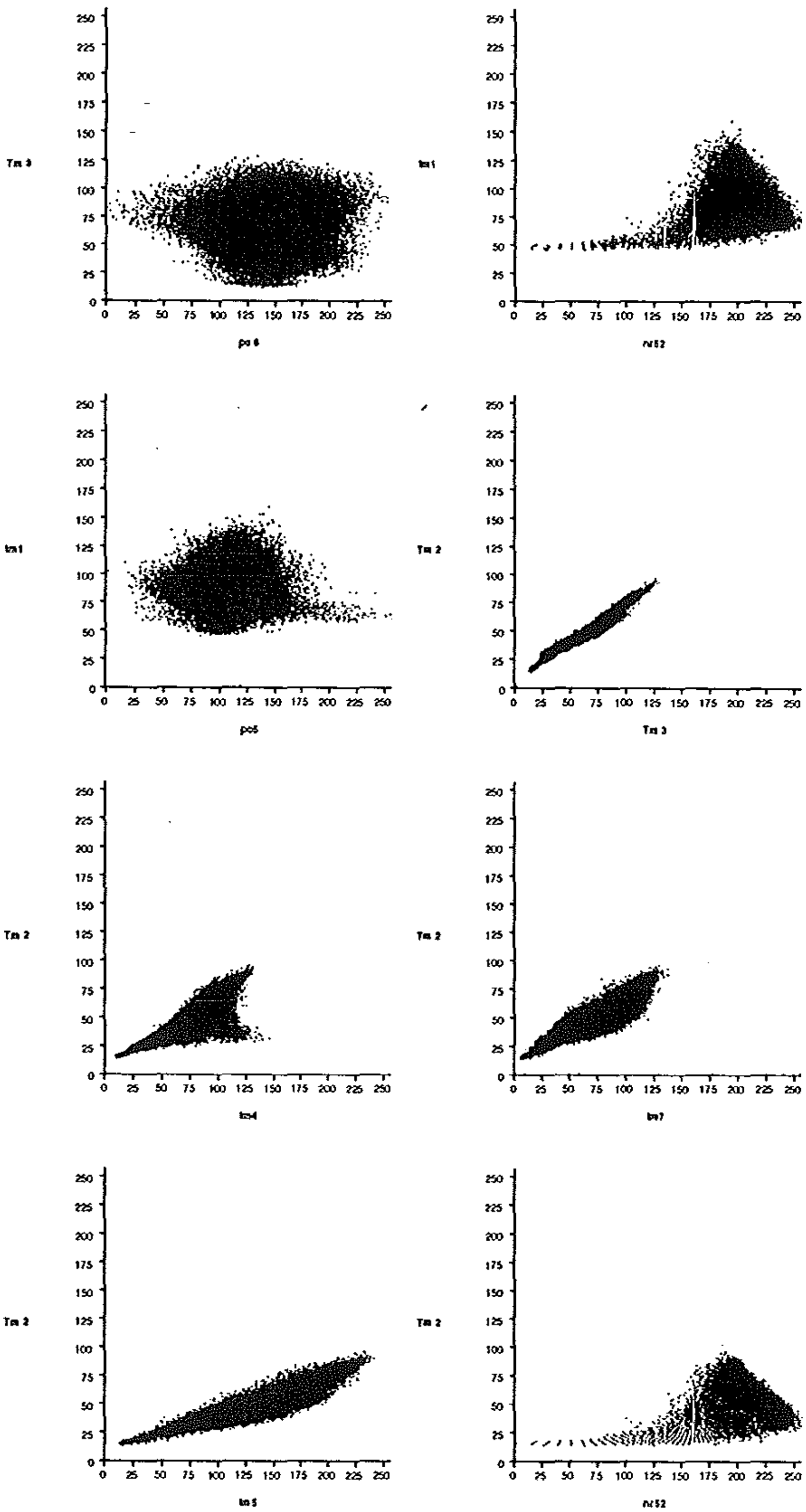

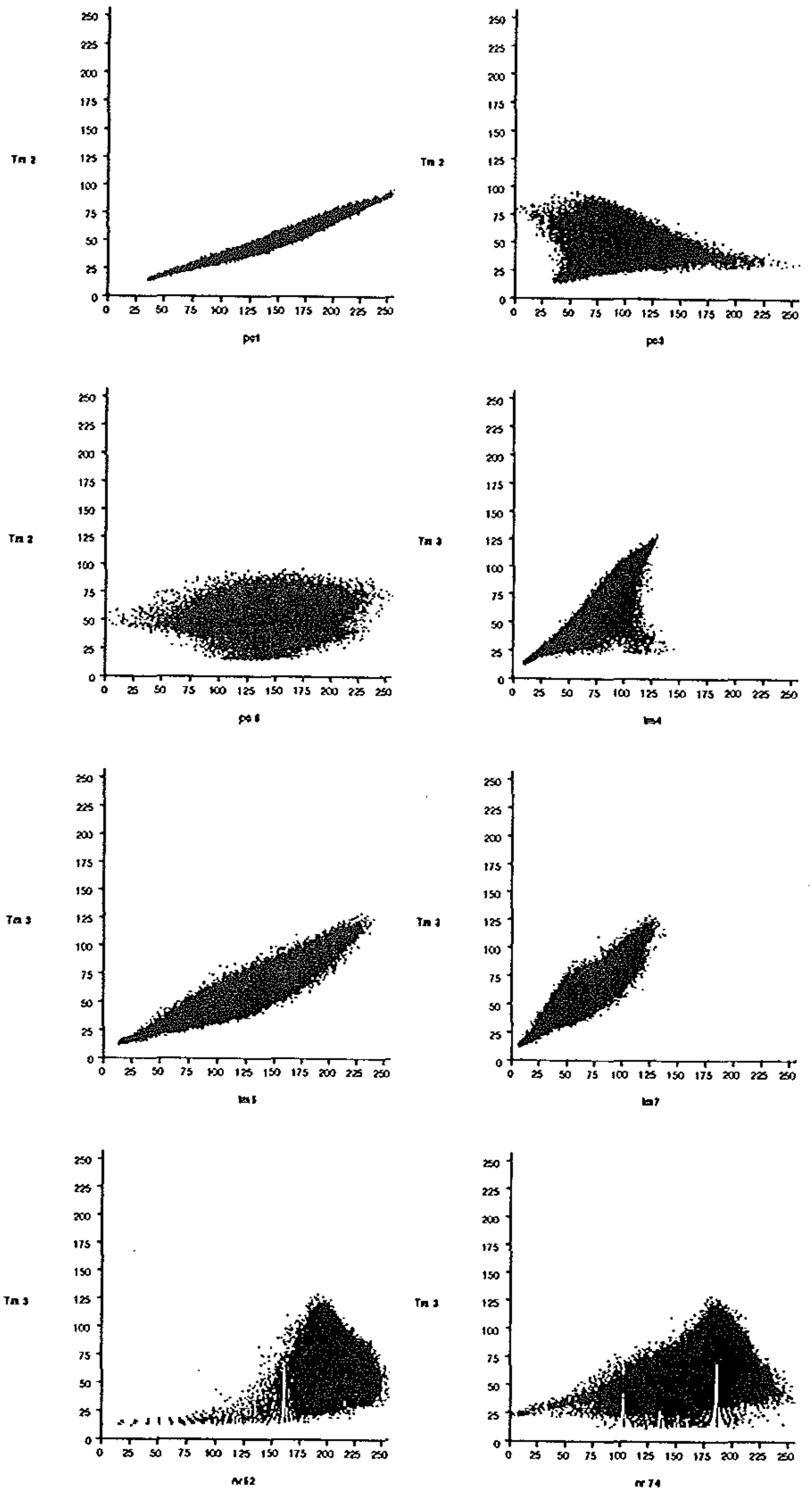

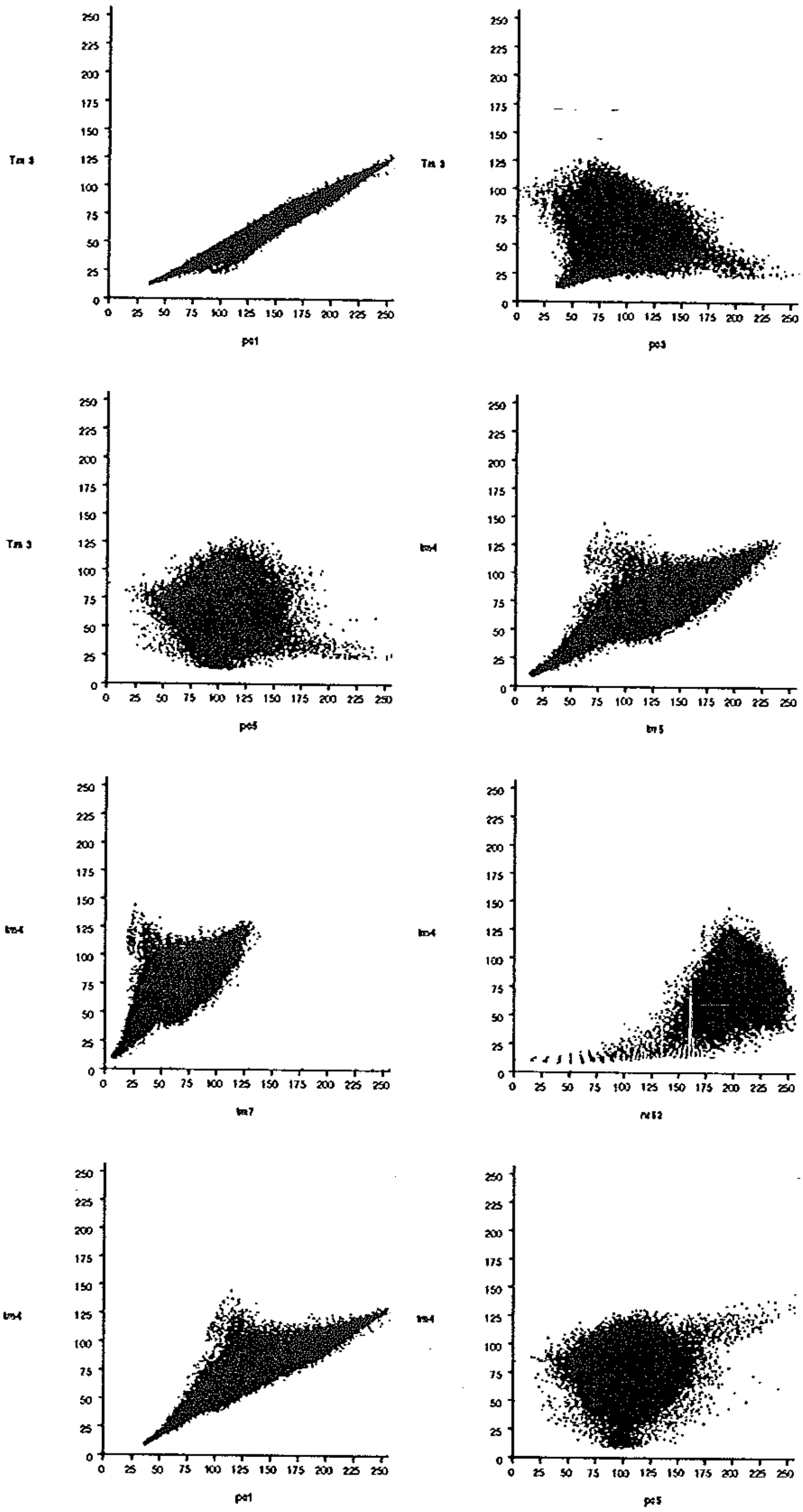

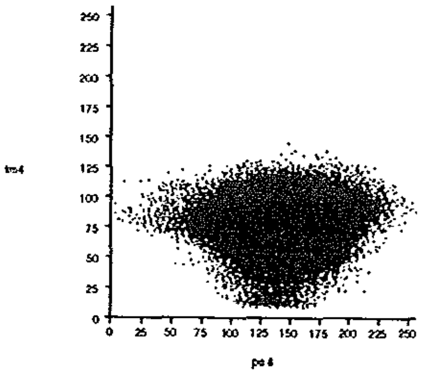

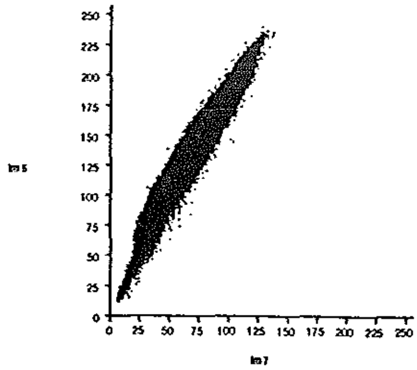

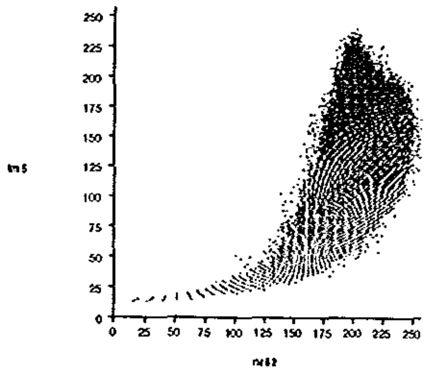

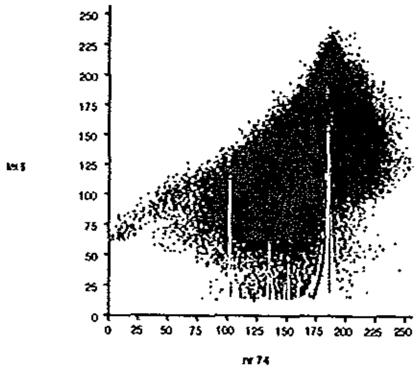

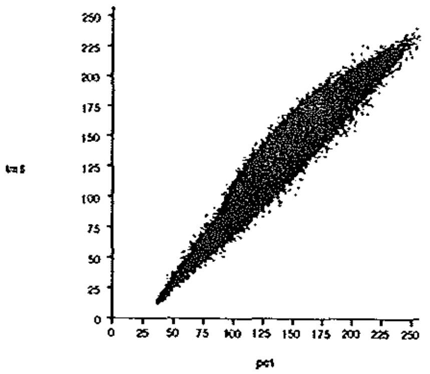

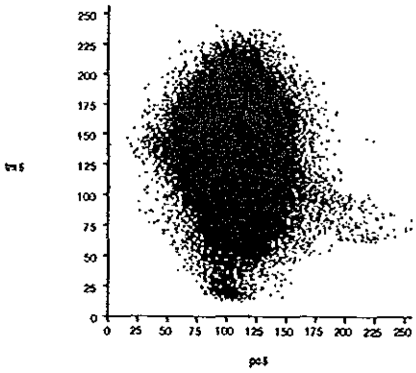

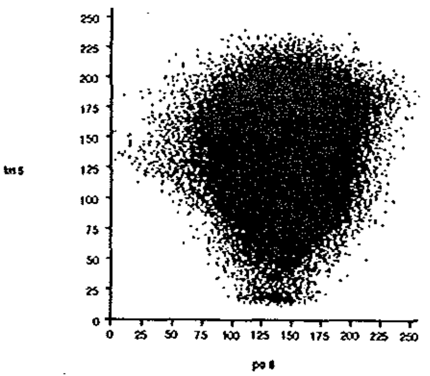

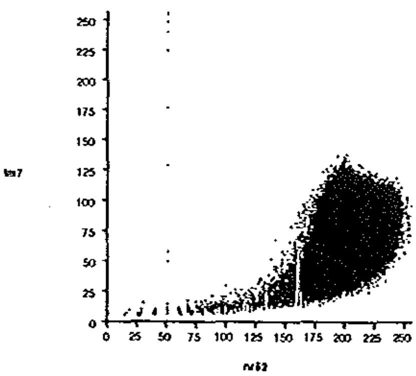

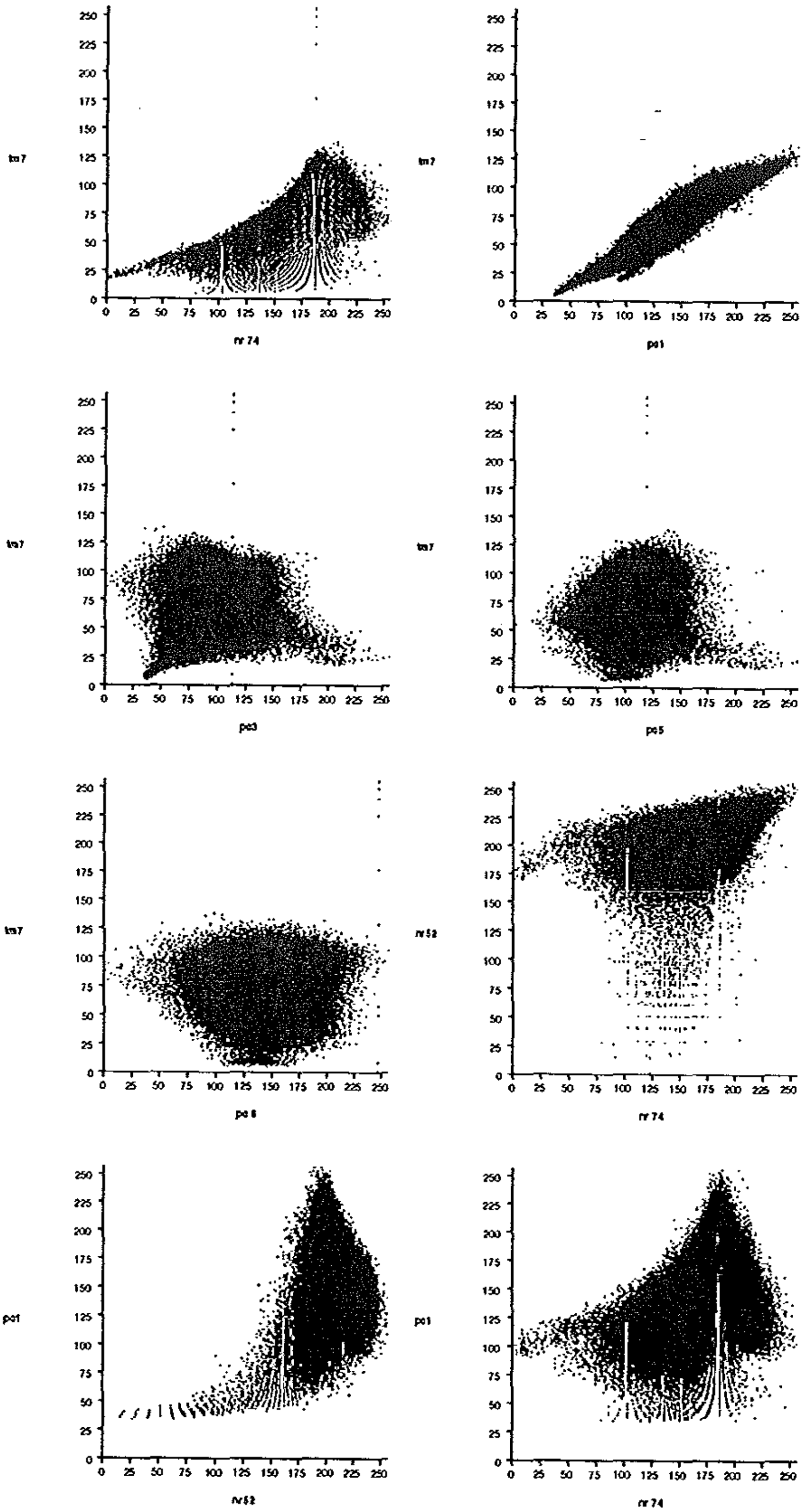

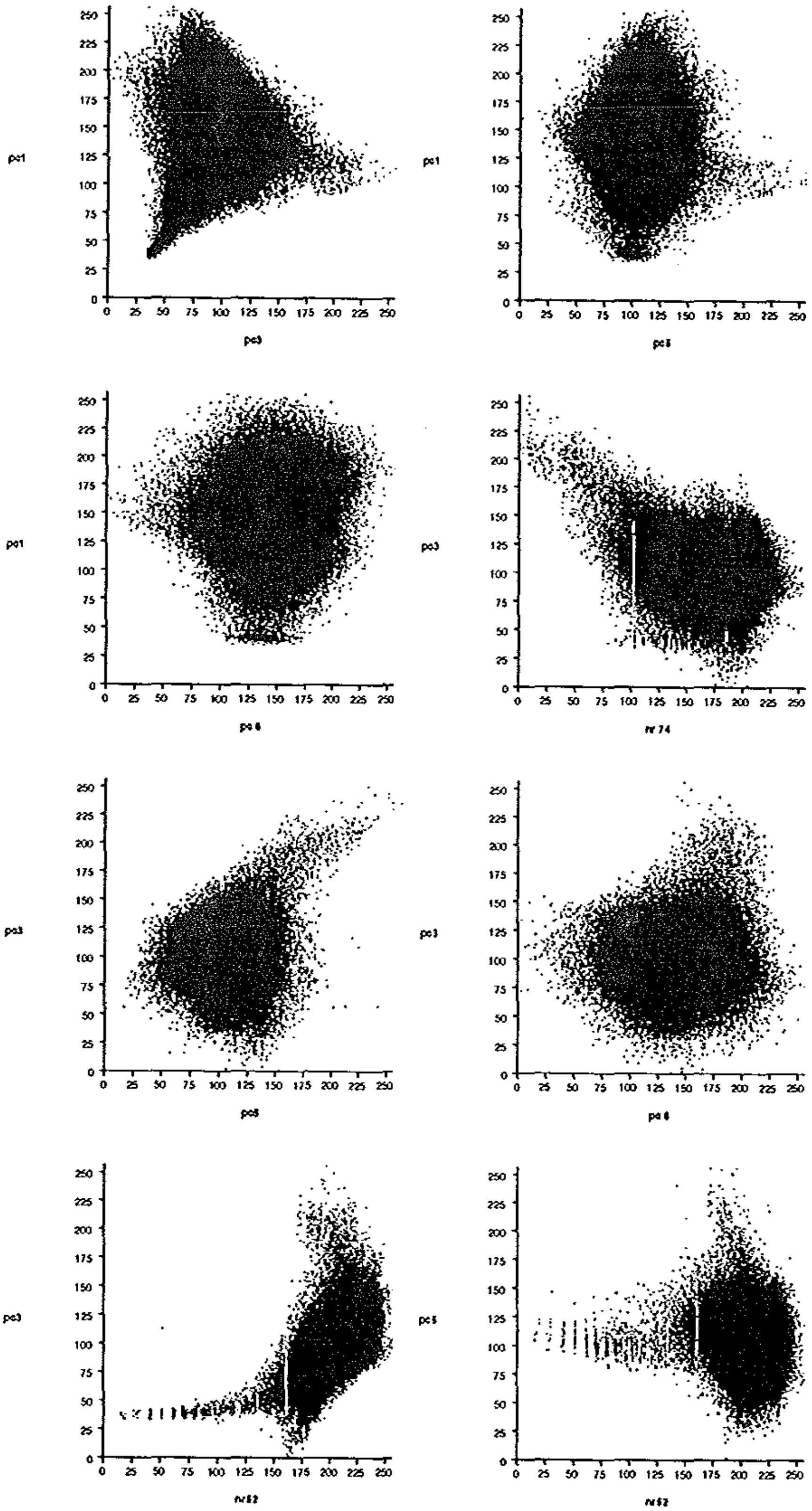

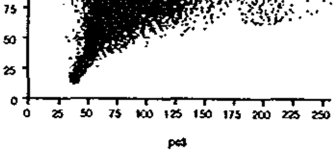

75
50
25
0
0 25 50 75 100 125 150 175 200 225 250
ped

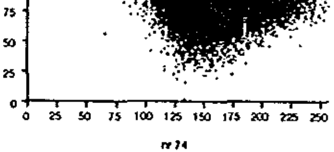

75
50
25
0
0 25 50 75 100 125 150 175 200 225 250

Correlation Matrix among the twelve original and transformed TM bands.

	TM 1	TM 2	TM 4	TM 5	TM 7	PC 1	PC 3	PC 5	PC 6	NR 52	NR 74	TM 3
TM 1	1.0000											
TM 2	0.9694	1.0000										
TM 4	0.8050	0.8383	1.0000									
TM 5	0.8202	0.8857	0.8143	1.0000								
TM 7	0.8098	0.8565	0.7034	0.9677	1.0000							
PC 1	0.9472	0.9768	0.8788	0.9570	0.9232	1.0000						
PC 3	-0.2510	0.1676	0.3110	0.1685	0.0703	0.0002	1.0000					
PC 5	-0.0067	0.0170	0.0266	-0.0877	0.0786	0.0003	-0.0001	1.0000				
PC 6	-0.0367	0.0858	-0.0070	0.0184	-0.0113	0.0001	-0.0000	0.0020	1.0000			
NR 52	0.0648	0.0599	0.2234	0.4615	0.4284	0.2395	0.5969	-0.2156	-0.1649	1.0000		
NR 74	0.3401	0.3703	0.0139	0.5655	0.7070	0.4308	-0.1720	0.0430	-0.0120	0.4275	1.0000	
TM 3	0.9340	0.9770	0.8321	0.9130	0.8897	0.9799	-0.0001	-0.0213	-0.0509	0.1316	0.4242	1.0000

DECLARATION

I, the undersigned, declare that this thesis is my work and that all sources of material used for the thesis have been duly acknoledged.

Name: Berhanu Temesgen
Signature: ____________
Place and date of submission:
June 1995, Addis Ababa.